PHYSICS OF SINGLE-TOP QUARK PRODUCTION AT HADRON COLLIDERS

By

Douglas Olaf Carlson

A DISSERTATION

Submitted to

Michigan State University

in partial fulfillment of the requirements

for the Degree of

DOCTOR OF PHILOSOPHY

Department of Physics and Astronomy

1995

ABSTRACT

PHYSICS OF SINGLE-TOP QUARK PRODUCTION AT HADRON COLLIDERS

By

Douglas Olaf Carlson

We discuss the physics of single-top quark production and decay at hadron colliders, such as the Tevatron, the Di-TeV and the LHC. Our study includes how to measure the mass and the width of the top quark produced from a single-t or a single-$\bar{t}$ process. We also show how to probe new physics by studying the couplings of t-b-W and show what can be improved from measuring the production rate of single-top events. We also discuss how to probe CP properties of the top quark by measuring the single-top production rate. Finally, we present a Monte Carlo study on the detection of single-top events in hadron collisions.

For Dawn.

ACKNOWLEDGEMENTS

Contents

List of Tables

List of Figures

x

Chapter 1

Introduction to the Standard Model

The Standard Model (SM) of elementary particle physics [1, 2, 3, 4] is a Yang–Mills gauge field theory with symmetry

$$\mathrm{SU(3)}_C \times \mathrm{SU(2)}_L \times \mathrm{U(1)}_Y. \tag{1.1}$$

It has been very successful in explaining and predicting experimental data. The $\mathrm{SU(3)}_C$ sector governs the strong force of the SM and is known as quantum chromo-dynamics (QCD). The $\mathrm{SU(2)}_L \times \mathrm{U(1)}_Y$ sector unifies the electromagnetic and weak forces, collectively known as the electroweak force. The unification of the electromagnetic and weak forces is accomplished in the SM via the mixing of the neutral $\mathrm{SU(2)}_L$ gauge boson and the hypercharge gauge boson of $\mathrm{U(1)}_Y$. Masses are introduced in a gauge invariant way through spontaneous symmetry breaking which gives rise to the as yet undiscovered Higgs boson (H). This process of spontaneous symmetry breaking is known as the Higgs mechanism.

The standard model does not incorporate the gravitational force. So far, no definitive quantum field theory of gravity exists. Gravity affects all massive particles, however, gravitational interactions with elementary particles are too weak and can be ignored.

In the standard model there are three generations of leptons and quarks as listed in Table 1.1. Associated with each force is one or several gauge bosons as listed in Table 1.2. For reference we list the masses of each particle as found in Reference [5]. So far, the only particle for which a discovery is lacking is the scalar Higgs boson.

In what follows, we briefly describe the particle spectrum, particle interactions and the 18 independent parameters which constitute the standard model.

1.1   The Matter Spectrum of Spin-$\frac{1}{2}$ Fermions

The matter spectrum consists of twelve fermions which are organized in Table 1.1 according to the symmetry structure of Equation (1.1). Each successive generation

Table 1.1: Lepton and Quark Masses

Particle	Symbol	Mass (GeV)	
Electron neutrino	ν_e	0	
Electron	e	0.00051	First
Up quark	u	0.002 to 0.008	Generation
Down quark	d	0.005 to 0.015	
Muon neutrino	ν_μ	0	
Muon	μ	0.106	Second
Charm quark	c	1.3 to 1.7	Generation
Strange quark	s	0.1 to 0.3	
Tau neutrino	ν_τ	0	
Tau	τ	1.78	Third
Top quark	t	174	Generation
Bottom quark	b	4.7 to 5.3	

Table 1.2: Boson Masses

Particle	Symbol	Mass (GeV)	
Photon	γ	0	Electromagnetic Force
W Boson	$W^\pm$	80.22	Charged Weak Force
Z Boson	Z^0	91.187	Neutral Weak Force
Gluon	G	0	Strong Force
Higgs	H	$60 < m_H < 800$	Spontaneous Symmetry Breaking

Table 1.3: Quantum numbers of the fermion spectrum

Chirality	Q	T_{W}^3	Y	C
ν_{eL}	0	1/2	-1	0
e_L	-1	-1/2	-1	0
u_L	2/3	1/2	1/3	r, g, b
d_L	-1/3	-1/2	1/3	r, g, b
e_R	-1	0	-2	0
u_R	2/3	0	4/3	r, g, b
d_R	-1/3	0	-2/3	r, g, b

is a more massive copy of the previous generation, so only the quantum numbers of the first generation are shown in Table 1.3. Under the $\mathrm{SU}(2)_L$ sector of the SM, left-handed fermions transform as weak isospin (T_{W}) doublets,

$$\ell_L = \begin{pmatrix} \nu_e \\ e \end{pmatrix}_L, \quad q_L = \begin{pmatrix} u \\ d \end{pmatrix}_L, \tag{1.2}$$

whereas right-handed fermions transform as singlets,

$$(e)_R, \quad (u)_R, \quad (d)_R. \tag{1.3}$$

Since neutrinos are massless Dirac fermions in the SM, there are no right-handed neutrinos. Once the third component of Weak isospin T_{W}^3 is assigned, the values of hypercharge Y can be determined to cancel the chiral anomalies [6]. With these quantum numbers in place, the charge quantization is determined by

$$Q = T_{\mathrm{W}}^3 + \frac{Y}{2}. \tag{1.4}$$

Only quarks transform under the $\mathrm{SU}(3)_C$ sector of the SM. Each quark flavor, (*i.e.*, $q = u, d, s, c, b, t$), carries *red*(r), *green*(g) or *blue*(b) color charge and therefore transforms as a triplet:

$$\Psi_q = \begin{pmatrix} q_r \\ q_g \\ q_b \end{pmatrix}. \tag{1.5}$$

1.2 Force Mediators as Spin-1 Gauge Bosons

Associated with the group structure of the SM are twelve generators and each generator is associated with a gauge boson. Therefore, $U(1)_Y$ has one generator, the neutral hypercharge gauge boson B_μ. $SU(2)_L$ has three $(2 \times 2 - 1 = 3)$ generators, two of which are charged $SU(2)_L$ gauge bosons $W_\mu^\pm$ and one neutral $SU(2)_L$ gauge boson W_μ^3. Finally, $SU(3)_C$ has eight $(3 \times 3 - 1 = 8)$ generators and therefore, eight gluons, $G_\mu^a, a = 1, 2, \ldots, 8$.

As stated earlier, electroweak unification is accomplished by mixing the B_μ and W_μ^3 gauge bosons. Formally this is accomplished via the following rotation,

$$\begin{pmatrix} Z_\mu^0 \\ A_\mu \end{pmatrix} = \begin{pmatrix} \cos\theta_W & -\sin\theta_W \\ \sin\theta_W & \cos\theta_W \end{pmatrix} \begin{pmatrix} W_\mu^3 \\ B_\mu \end{pmatrix}, \tag{1.6}$$

where θ_W, called the weak mixing angle, is chosen such that A_μ only couples with charged particles. A_μ is then identified as the photon field in quantum electrodynamics (QED) and additionally, a neutral weak force, Z_μ^0, is obtained.

At this point in the theory, all fermions and gauge bosons are massless to preserve gauge invariance. In the next two sections we describe how the force mediators interact with fermions and amongst themselves. The Higgs mechanism is also introduced to incorporate mass in a gauge invariant way.

1.3 Gauge Invariant Interactions of Fermion and Gauge Boson Fields

We begin with the lagrangian for a massless free fermion field Ψ,

$$\mathcal{L}_{FK} = \overline{\Psi}\, i\slashed{\partial}\, \Psi. \tag{1.7}$$

Equation (1.7) is the kinetic term for fermion fields.[1] To make the lagrangian gauge invariant, we introduce the gauge covariant derivative

$$\partial_\mu \to D_\mu = \partial_\mu - ig_1\frac{Y}{2}B_\mu - ig_2\frac{\tau^j}{2}W_\mu^j - ig_3\frac{\lambda^a}{2}G_\mu^a, \tag{1.8}$$

where $j = 1, 2, 3$ and $a = 1, 2, \ldots, 8$. The τ^j's are the Pauli matrices defined in Appendix A and $T_W^j = \frac{\tau^j}{2}$ is the Weak isospin. The (3×3) matrices (generators) $\lambda^a, a = 1, 2, \ldots, 8$, are the $SU(3)_C$ matrices. As a result, we obtain gauge interaction terms in the lagrangian.

The B_μ term acts on all fields with different Y's, including leptons and quarks in Table 1.3 (same for the other two generations) and the Higgs doublet field Φ discussed

---

[1] $\slashed{\partial} = \partial_\mu\gamma^\mu$ where ∂_μ is the Lorentz invariant space-time derivative and γ^μ are the Dirac matrices.

in Section 1.5 below. The W^j_μ term acts only on the $\text{SU}(2)_L$ doublets with non-zero T^3_W and the field Φ. In the process of obtaining electroweak unification the coupling constants, g_1 and g_2 become related through the weak mixing angle θ_W via

$$\frac{g_2}{g_1} = \tan\theta_W, \tag{1.9}$$

where $g_1 \sin\theta_W = e$. The value of e is related to the fine structure constant α by $\alpha = e^2/4\pi$.

For electroweak interactions, the colors of the quarks have to be the same since $\text{SU}(2)_L \times \text{U}(1)_Y$ does not act on color space. Also, the A_μ and Z^0_μ fields do not induce quark or lepton flavor changing at the Born level, (*i.e.* no $u \leftrightarrow c \leftrightarrow t$, $d \leftrightarrow s \leftrightarrow b$, $\nu_e \leftrightarrow \nu_\mu \leftrightarrow \nu_\tau$ or $e \leftrightarrow \mu \leftrightarrow \tau$ transitions occur). However, charged current transitions via $W^\pm_\mu$ do occur and for quarks, are not restricted by generation (*i.e.* $u, c, t \leftrightarrow d, s, b$ transitions are allowed). Lepton flavor changes are restricted to generation due to massless neutrinos. Finally, the SM does not allow for direct lepton-quark transitions.

The G^a_μ term in Equation (1.8) only acts on colored fermions, *i.e.* quarks. The coupling strength $g_3 = g_S$ is universal for all colored quarks. Analogous to the fine structure constant α in electromagnetic theory is the strong coupling constant $\alpha_S = g_S^2/4\pi$ in QCD. Here again, no flavor changes occur.

1.4 Gauge Field Self Interactions

To complete the lagrangian for massless fermions and gauge bosons and their interactions, we must introduce the kinetic term for gauge bosons,

$$\mathcal{L}_{GK} = -\frac{1}{4}\mathcal{B}_{\mu\nu}\mathcal{B}^{\mu\nu} - \frac{1}{4}\mathcal{W}^i_{\mu\nu}\mathcal{W}^{i\mu\nu} - \frac{1}{4}\mathcal{G}^a_{\mu\nu}\mathcal{G}^{a\mu\nu}, \tag{1.10}$$

where

$$\mathcal{B}_{\mu\nu} = \partial_\mu B_\nu - \partial_\nu B_\mu, \tag{1.11}$$

$$\mathcal{W}^i_{\mu\nu} = \partial_\mu W^i_\nu - \partial_\nu W^i_\mu + g_2\epsilon^{ijk}W^j_\mu W^k_\nu, \tag{1.12}$$

$$\mathcal{G}^a_{\mu\nu} = \partial_\mu G^a_\nu - \partial_\nu G^a_\mu + g_S f^{abc}G^b_\mu G^c_\nu. \tag{1.13}$$

The Lie group structure constants ϵ^{ijk} and f^{abc} are defined through the following anti-commutation relations,

$$\left[\frac{\tau^i}{2}, \frac{\tau^j}{2}\right] = i\,\epsilon^{ijk}\frac{\tau^k}{2}, \quad i,j,k = 1,2,3 \tag{1.14}$$

and

$$\left[\frac{\lambda^a}{2}, \frac{\lambda^b}{2}\right] = i\,f_{abc}\,\frac{\lambda^c}{2}, \quad a, b, c = 1, 2, \dots, 8 \tag{1.15}$$

for SU(2) and SU(3), respectively.

We note that the pure Yang-Mills terms, $-\frac{1}{4}\mathcal{W}^i_{\mu\nu}\mathcal{W}^{i\mu\nu}$ and $-\frac{1}{4}\mathcal{G}^a_{\mu\nu}\mathcal{G}^{a\mu\nu}$ contain factors that are trilinear and quadrilinear in W^i_μ and G^a_μ. These Yang-Mills terms expand out partially as

$$\cdots - g_2\,\epsilon^{ijk}\,(\partial_\mu W^i_\nu)W^{j\mu}W^{k\nu} - \frac{g_2^2}{4}\,\epsilon^{ijk}\,\epsilon^{ilm}\,W^j_\mu W^k_\nu W^{l\mu}W^{m\nu} \tag{1.16}$$

and

$$\cdots - g_S\,f^{abc}\,(\partial_\mu G^a_\nu)G^{b\mu}G^{c\nu} - \frac{g_S^2}{4}\,f^{abc}\,f^{ade}\,G^b_\mu G^c_\nu G^{d\mu}G^{e\nu} \tag{1.17}$$

respectively, and correspond to self-couplings of non-abelian gauge fields. This is fundamentally different than in the abelian case where, in QED, photons do not directly couple with photons. It also accounts for the short distance interaction of the strong force, despite the fact that the gluon is massless. As can be seen in Chapter 2, the triple gluon interaction contributes to $t\bar{t}$ production via $gg \to t\bar{t}$ at hadron colliders.

1.5   The Higgs Mechanism

The goal of the Higgs mechanism is to introduce mass to the particles in the SM in a gauge invariant way. We begin by defining a complex doublet scalar field Φ composed of four real scalar fields H, ϕ^0, ϕ^1 and ϕ^2 where

$$\Phi = \frac{1}{\sqrt{2}}\begin{pmatrix} v + H + i\phi^0 \\ i\phi^1 - \phi^2 \end{pmatrix} = \begin{pmatrix} \frac{v+H+i\phi^0}{\sqrt{2}} \\ i\phi^- \end{pmatrix}. \tag{1.18}$$

The quantum numbers of the Higgs field are as shown in Table 1.4.

The fields ϕ^0 and $\phi^\pm = (\phi^1 \mp i\phi^2)/\sqrt{2}$ are the unphysical would-be Goldstone bosons associated with spontaneous symmetry breaking. They give rise to the masses of the gauge bosons $W^\pm$ and Z^0. One physical field thus remains, which is the Higgs field H. The constant $v \simeq 246$ GeV is the scale characterizing the symmetry breaking scale and is called the vacuum expectation value of Φ, where

$$\langle\Phi\rangle_0 \equiv \langle 0|\Phi|0\rangle = \begin{pmatrix} \frac{v}{\sqrt{2}} \\ 0 \end{pmatrix}. \tag{1.19}$$

Table 1.4: Quantum numbers of the Higgs doublet

	Q	T_W^3	Y	C
$\frac{v+H+i\phi^0}{\sqrt{2}}$	0	1/2	-1	0
$i\phi^-$	-1	-1/2	-1	0

The lagrangian for the Higgs sector is

$$\mathcal{L}_\Phi = (D_\mu\Phi)^\dagger(D^\mu\Phi) - \frac{\lambda}{2}(\Phi^\dagger\Phi)^2 - \mu^2(\Phi^\dagger\Phi), \tag{1.20}$$

with

$$D_\mu\Phi = \left[\partial_\mu - ig_1\frac{Y}{2}B_\mu - ig_2\frac{\tau^j}{2}W_\mu^j\right]\Phi \tag{1.21}$$

as in Equation (1.8) without the gluon interaction.

If $\mu < 0$ and $\lambda > 0$ then the minimum of the potential energy occurs at

$$v = \sqrt{\frac{-2\mu}{\lambda}}. \tag{1.22}$$

The Goldstone bosons $\phi^\pm$ and ϕ^0 are "eaten" by the vector bosons $W^\pm$ and Z^0, respectively, where

$$M_W = \frac{1}{2}g_2v \text{ and } M_Z = \frac{M_W}{\cos\theta_W}. \tag{1.23}$$

Therefore, $W^\pm$ and Z^0 have three polarization states; two transverse and one longitudinal. The massless photon and gluon have only the two transverse polarization states. The Higgs mass is given by

$$m_H = v\sqrt{\lambda}. \tag{1.24}$$

To introduce fermion mass in a gauge invariant way one introduces the Higgs mechanism through Yukawa coupling interactions. For the first generation

$$\mathcal{L}_{Yukawa} = \frac{\sqrt{2}m_u}{v}\left(\bar{u}_L\ \bar{d}_L\right)\Phi\,u_R + \frac{\sqrt{2}m_d}{v}\left(\bar{u}_L\ \bar{d}_L\right)\left(-i\tau_2\Phi^*\right)d_R$$

$$+\frac{\sqrt{2}m_e}{v}\left(\bar{\nu}_L\ \bar{e}_L\right)\left(-i\tau_2\Phi^*\right)e_R + \text{hermitian conjugate} \tag{1.25}$$

where m_u, m_d and m_e are up quark, down quark and electron masses, respectively (neutrinos are massless) and

$$-i\tau_2\Phi^* = \begin{pmatrix} 0 & -1 \\ 1 & 0 \end{pmatrix} \Phi^* = \begin{pmatrix} i\phi^+ \\ \frac{v+H+i\phi^0}{\sqrt{2}} \end{pmatrix}. \tag{1.26}$$

As mentioned in Section 1.3, neutral currents coupled to γ, Z^0 and G do not change flavor, although G changes color, but charged currents coupled to $W^\pm$ do change flavor. For leptons, the flavor change does not exceed generational bounds, due to the massless neutrino. However, there is a chance that an up quark, for instance, can change to a down quark, a strange quark or even a bottom quark. This is called quark mixing, which is due to the weak eigenstates (indicated by the subscript "Weak") of quarks being different than the mass eigenstates (indicated by the subscript "Mass").

By convention, the three charge 2/3 quarks u, c and t are unmixed:

$$\begin{pmatrix} u \\ c \\ t \end{pmatrix}_{\text{Weak}} = \begin{pmatrix} u \\ c \\ t \end{pmatrix}_{\text{Mass}}. \tag{1.27}$$

All the mixing is therefore expressed in terms of a (3×3) unitary matrix V operating on the charge (-1/3) quarks d, s and b:

$$\begin{pmatrix} d \\ s \\ b \end{pmatrix}_{\text{Weak}} \equiv \begin{pmatrix} V_{ud} & V_{us} & V_{ub} \\ V_{cd} & V_{cs} & V_{cb} \\ V_{td} & V_{ts} & V_{tb} \end{pmatrix} \begin{pmatrix} d \\ s \\ b \end{pmatrix}_{\text{Mass}}$$

$$\approx \begin{pmatrix} 1 - \lambda^2/2 & \lambda & A\lambda^3(\rho - i\eta) \\ -\lambda & 1 - \lambda^2/2 & A\lambda^2 \\ A\lambda^3(1 - \rho - i\eta) & -A\lambda^2 & 1 \end{pmatrix} \begin{pmatrix} d \\ s \\ b \end{pmatrix}_{\text{Mass}}. \tag{1.28}$$

The matrix V is known as the Cabibbo–Kobayashi–Maskawa matrix (CKM), which consists of three mixing angles and one phase. The second parameterization is due to Wolfenstein [7], where $\lambda \simeq 0.22$, $A \simeq 1$, $\eta \simeq 0.5$ and $-0.4 \leq \rho \leq 0.2$. CP violation, which is the violation of combined charge conjugation C and the parity transformation P, is characterized by the CP violating phase in $\rho - i\eta$.

1.6   Review

In this introduction to the SM, we have outlined how the SM is constructed based on gauge invariance and the Higgs mechanism. Although the SM has been successful in describing experimental data, there are 18 independent parameters which must be determined experimentally. These parameters are:

- nine fermion masses: $m_e, m_\mu, m_\tau, m_u, m_d, m_c, m_s, m_t, m_b$ (neutrinos are massless),

- four CKM parameters: λ, A, η, ρ,

- four electroweak parameters: e, θ_W, M_W, m_H,

- the strong coupling constant: α_S.

Chapter 2

Introduction to the Top Quark

If the SU(2) structure of the Standard Model (SM) holds, the top quark (t) has to exist as the weak isospin partner of the bottom quark (b) [8]. If the coupling of t-t-Z is as predicted in the SM, then from LEP and SLAC experiments the mass of the top quark (m_t) has to be larger than half of the Z-boson mass ($\sim 45\,\mathrm{GeV}$) independent of how the top quark decays. If the coupling of t-b-W is as predicted in the SM, then from the measurement of the total width of the W–boson, by measuring the ratio of the event rates of $\bar{\mathrm{p}}\mathrm{p} \to W(\to \ell\nu)$ to $\bar{\mathrm{p}}\mathrm{p} \to Z(\to \ell^+\ell^-)$ [1], the mass of the top quark (m_t) has to be larger than 62 GeV independent of how the top quark decays [9]. From examining the radiative corrections to low energy observables, such as the ρ parameter[2] which is proportional to m_t^2 at the one loop level [10], m_t has to be less than about $200\,\mathrm{GeV}$. Based upon analysis of a broad range of Electroweak data, the mass of the SM top quark is expected to be in the vicinity of 150 to 200 GeV [11, 12, 13, 14]. Independently, from the direct search at the Tevatron, the top quark has been discovered and found to have mass of $m_t = 176 \pm 8\,(\mathrm{stat.}) \pm 10(\mathrm{sys.})\,\mathrm{GeV}$ from CDF data [15], and $m_t = 199^{+29}_{-21}\,(\mathrm{stat.}) \pm 22(\mathrm{sys.})\,\mathrm{GeV}$ from DØ data [16].

For a heavy top quark, m_t is of the order of the electroweak symmetry breaking scale $v = (\sqrt{2}G_F)^{-1/2} = 246\,\mathrm{GeV}$. In fact, recall the Yukawa coupling interaction, this time for third generation quarks,

$$\mathcal{L}_{Yukawa} = \frac{\sqrt{2}m_t}{v}\,(\bar{t}_L\,\bar{b}_L)\,\Phi\,t_R + \frac{\sqrt{2}m_b}{v}\,(\bar{t}_L\,\bar{b}_L)\,(-i\tau_2\Phi^*)\,b_R. \tag{2.1}$$

We see that

$$\frac{\sqrt{2}m_t}{v} \sim 1, \tag{2.2}$$

---

[1] A proton is denoted by p and an anti-proton by $\bar{\mathrm{p}}$

[2] $\rho = \frac{M_W^2}{M_Z^2 \cos^2\theta_W}$, where M_W (or M_Z) is the mass of $W^\pm$ (or Z) boson. θ_W is the weak mixing angle. ρ has been measured to the accuracy of about 0.1%.
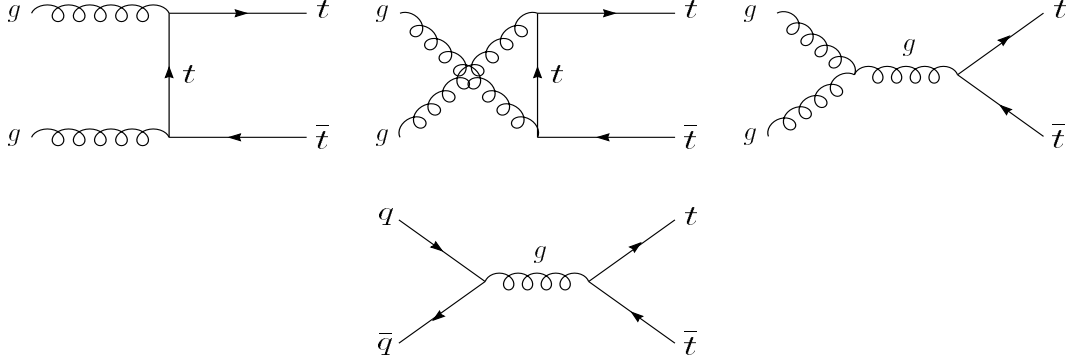
Figure 2.1: Diagrams contributing to the QCD production of $q\bar{q}$, $gg \rightarrow t\bar{t}$

for $m_t = 175$ GeV. Because the generation of fermion mass can be closely related to the electroweak symmetry breaking [17, 18], effects from new physics should be more apparent in the top quark sector than any other light sector of the electroweak theory. Thus, the top quark system may be used to probe the symmetry breaking sector. A few examples were discussed in Ref. [19] to illustrate that different models of electroweak symmetry breaking mechanism will induce different interactions among the top quark and the $W-$ and $Z-$bosons. Therefore, hopefully through studying the top quark system one may eventually learn about the symmetry breaking sector of the electroweak theory.

The most important consequence of a heavy top quark is that to a good approximation it decays as a free quark because its lifetime is short and it does not have time to bind with light quarks before it decays [20]. Furthermore, because the heavy top quark has the weak two-body decay $t \rightarrow bW^+$, it will analyze its own polarization. Thus we can use the polarization properties of the top quark as additional observables to test the SM and to probe new physics. In the SM, the heavy top quark produced from the usual QCD process, at the Born level, is unpolarized. However, top quarks will have longitudinal polarization if weak effects are present in their production [21]. For instance, the top quark produced from the $W-$gluon fusion process is left-hand polarized. With a large number of top quark events, it will be possible to test the polarization effects of top quarks.

How to detect a SM top quark pair produced via the QCD processes $q\bar{q}$, $gg \rightarrow t\bar{t}$, as shown in Figure 2.1, has been extensively studied in the literature [22]. In this paper we will concentrate on how to detect and study the top quark produced from the single-top quark processes $q'g(W^+g) \rightarrow qt\bar{b}$, $q'b \rightarrow qt$, $gb \rightarrow W^-t$, and $q'\bar{q} \rightarrow W^* \rightarrow t\bar{b}$. For the single-top production we will only consider the decay mode of $t \rightarrow bW^+ \rightarrow b\ell^+\nu$, with $\ell^+ = e^+$ or ν^+. (The branching ratio for this decay mode is Br = $\frac{2}{9}$.)

The rest of this paper is organized as follows. In Chapter 3 we discuss the production rates of top quarks at hadron colliders. Following that, we will discuss in Chapters 4 and 5, respectively, how to measure the mass and the width of the top quark. In Chapter 6 we discuss what we have learned about the couplings of the top quark to the weak gauge bosons and show what can be improved from measuring the production rate of single-top quark events. We will also discuss in Chapter 7 the potential of the Tevatron as a $\bar{p}p$ collider to probe CP properties of the top quark

by simply measuring the single-top quark production rate. Finally, in Chapter 8 we present a Monte Carlo study on the detection of a single-top quark event in hadron collisions. Various unique features of the kinematics of the single-top quark signal will be discussed. Chapter 9 contains our conclusions. Based upon the results of the FNAL CDF and DØ , the mass of the SM top quark m_t is not likely to be lighter than, say, $140\,\text{GeV}$. Throughout this paper we will use $m_t = 180\,\text{GeV}$ (or $140\,\text{GeV}$) as an example of a heavy (or a light) top quark for our studies.

Chapter 3

The Single-Top Production Mechanism

In this chapter we consider the production rate of a single-top quark at the Tevatron, the Di-TeV (the upgraded Tevatron) and the LHC (Large Hadron Collider) colliders. In referring to single-top production, unless stated otherwise, we will concentrate only on the positive charge mode (*i.e.*, only including single-t, but not single-$\bar{t}$). The colliders we consider are the Tevatron (a $\bar{p}p$ collider) with the Main Injector at $\sqrt{S} = 2\,\text{TeV}$, the Di-TeV (a $\bar{p}p$ collider) at $4\,\text{TeV}$ and the LHC (a pp collider) at $\sqrt{S} = 14\,\text{TeV}$ with an integrated luminosity of $1\,\text{fb}^{-1}$, $10\,\text{fb}^{-1}$, and $100\,\text{fb}^{-1}$, respectively.[1]

A single-top quark signal can be produced from either the W–gluon fusion process $q'g(W^+g) \to qt\bar{b}$ (or $q'b \to qt$) [23, 24], the Drell-Yan type process $q'\bar{q} \to W^* \to t\bar{b}$ (also known as "W^*" production) [25], or Wt production via $gb \to W^-t$ [26]. The corresponding Feynman diagrams for these processes are shown in Figure 3.1.

In Figures 3.2 and 3.3 we show the total cross sections of these processes for the Tevatron, the Di-TeV and the LHC energies referred to above. For reference we include plots of the cross sections of top quarks as a function of m_t in both the $\bar{p}p$ collisions, shown in Figure 3.2, and pp collisions, shown in Figure 3.3. The parton distribution function (PDF) used in our calculation is the leading order set CTEQ2L [27]. We note that taking the Λ_{QCD} value given in CTEQ2L PDF we obtain $\alpha_s(M_Z) = 0.127$ which is about 15% larger than the value of 0.110 in CTEQ2M PDF [27]. We found that if we rescale the $t\bar{t}$ production rates obtained from CTEQ2L PDF with born level amplitudes by the ratio of $\alpha_s^2(Q, \Lambda_{QCD})$ from CTEQ2M and that from CTEQ2L, which yields 0.7 for $Q = M_Z$, then our total rates are in good agreement with those obtained using NLO PDF and NLO amplitudes [28], see, for example, Reference [29]. Hereafter we shall use the scaled results for our rates. The constituent cross sections are all calculated at tree level for simplicity to study the kinematics of the top quark and its decay products.

To include the production rates for both single-t and single-$\bar{t}$ events at $\bar{p}p$ colliders,

---
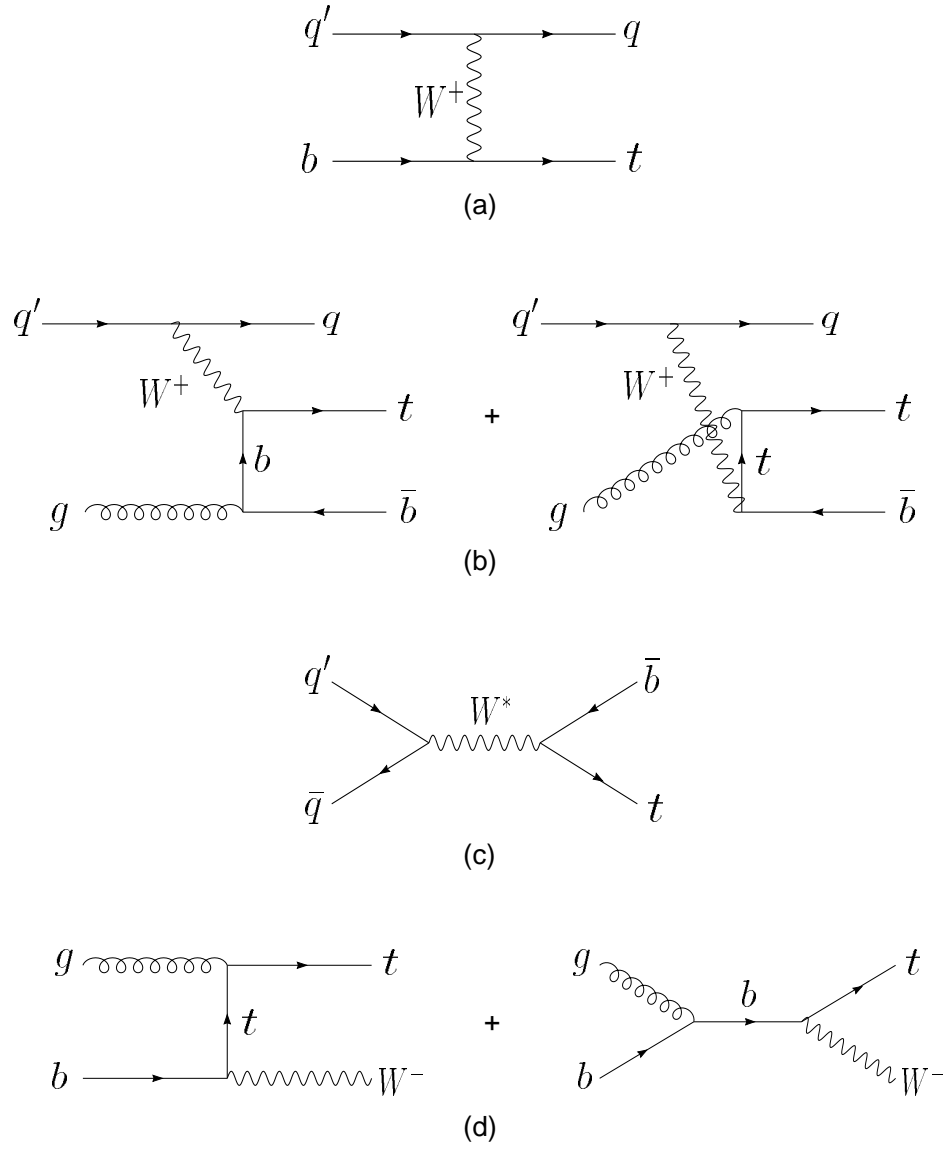
Figure 3.1: Diagrams for various single-top quark processes.
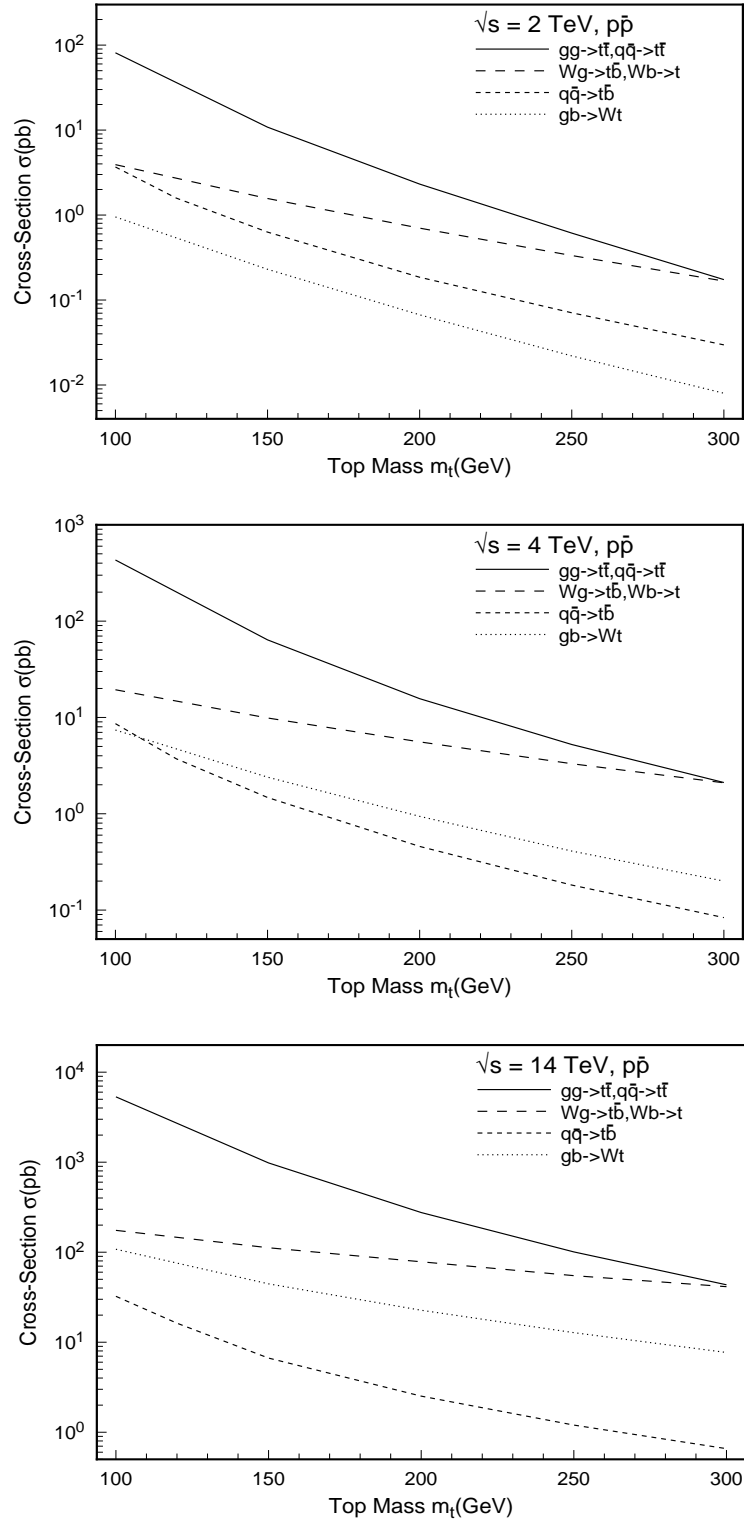
Figure 3.2:   Rate in [pb] for $q\bar{q}$, $gg \rightarrow t\bar{t}$, $q'g(W^+g) \rightarrow qt\bar{b}$, $q'\bar{q} \rightarrow W^* \rightarrow t\bar{b}$ and $gb \rightarrow W^-t$ at various energies of $\bar{p}p$ colliders.
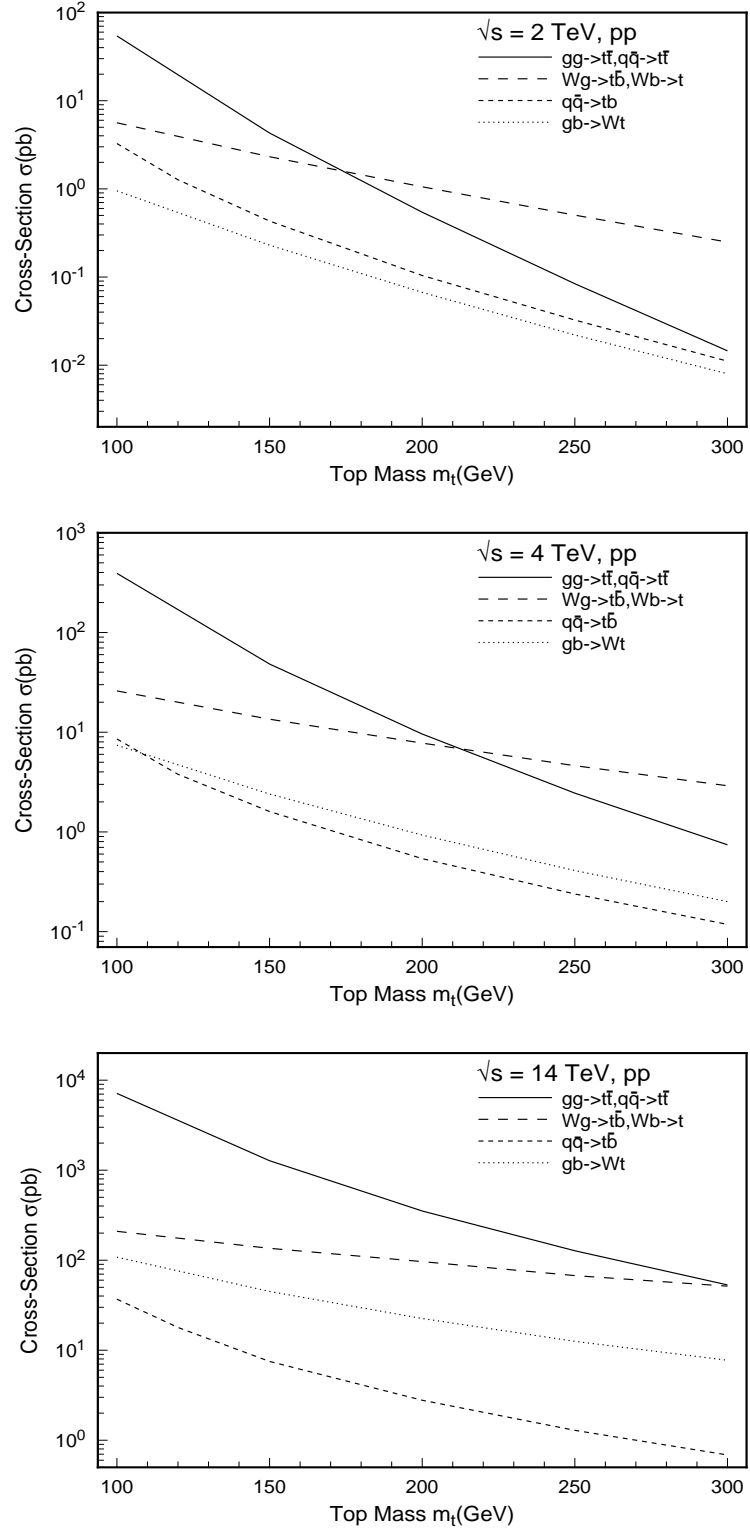
Figure 3.3: Rate in [pb] for $q\bar{q}$, $gg \to t\bar{t}$, $q'g(W^+g) \to qt\bar{b}$, $q'\bar{q} \to W^* \to t\bar{b}$ and $gb \to W^-t$ at various energies of pp colliders.

Table 3.1: Rates of the above processes for $m_t = 180(140)\,$GeV. (Branching ratios are not included here.) For $\sqrt{S} = 2\,$TeV and $4\,$TeV we include rates for a $\bar{p}p$ machine. At $\sqrt{S} = 14$ TeV the rates are for a pp machine. For the single-top rates we only include single-t production.

	Cross Section (pb)			
$\sqrt{S}$(TeV)	$q\bar{q}, gg \to t\bar{t}$	$q'g \to qt\bar{b}$ (or $q'b \to qt$)	$q'\bar{q} \to W^* \to t\bar{b}$	$gb \to W^-t$
2	4.5(16)	1(2)	0.3(0.8)	0.1(0.3)
4	26(88)	7(11)	0.8(2.1)	1.3(2.9)
14	430(1300)	100(140)	4.6(11)	3.6(8.8)

a factor of 2 should be multiplied to the single-t rates shown in Figures 3.2 and 3.3 because the parton luminosity for single-$\bar{t}$ production is the same as that for single-t. Similarly, at pp colliders the rates should be multiplied by about 1.5 for the center-of-mass energy $(\sqrt{S})$ of the collider up to approximately 4 TeV, but almost a factor of two at higher energies (say, $\sqrt{S} \geq 8$ TeV up to about 14 TeV) because the relevant parton luminosities for producing a single-t and a single-$\bar{t}$ event in pp collisions are different. As shown in Figures 3.2 and 3.3 the total rate for single-top production is about the same at $\bar{p}p$ and pp colliders for $\sqrt{S} \geq 8\,$TeV because the relevant valence and sea quark parton distributions are about equal for $100\,$GeV $< m_t < 300\,$GeV. For smaller $\sqrt{S}$, up to about 4 TeV, a $\bar{p}p$ collider is preferred over a pp collider for heavy top quark production because of its larger parton luminosities. Similarly, for $t\bar{t}$ pair productions at small $\sqrt{S}$, the quark initiated process $q\bar{q} \to t\bar{t}$ is more important than the gluon fusion process $gg \to t\bar{t}$. At $\sqrt{S}$ from 8 to 14 TeV the $t\bar{t}$ rate is about the same in $\bar{p}p$ and pp collisions because the $gg \to t\bar{t}$ subprocess becomes dominant.

For later reference in this paper, we show the rates of the above processes in Table 3.1 for $m_t = 180(140)\,$GeV. (Branching ratios are not included here.) For $\sqrt{S} = 2$ and 4 TeV we include only the rates for a $\bar{p}p$ machine, whereas at $\sqrt{S} = 14$ TeV the rates are for a pp machine. Again, for the single-top rates we only include t production.

Both in Figures 3.2 and 3.3 and Table 3.1, we have given the cross section of single-top quarks produced from either the $q'g(W^+g) \to qt\bar{b}$ or $q'b \to qt$ processes. From now on, we will refer to this production rate as the rate of the W–gluon fusion process. The single-top quark produced from the W–gluon fusion process involves a very important and not yet well-developed technique of handling the kinematics of a *heavy b* parton inside a hadron. Thus the kinematics of the top quark produced from this process can not be accurately calculated yet. However, the total event rate for single-top quark production via this process can be estimated using the method proposed in Reference [30]. The total rate for the W–gluon fusion process involves the
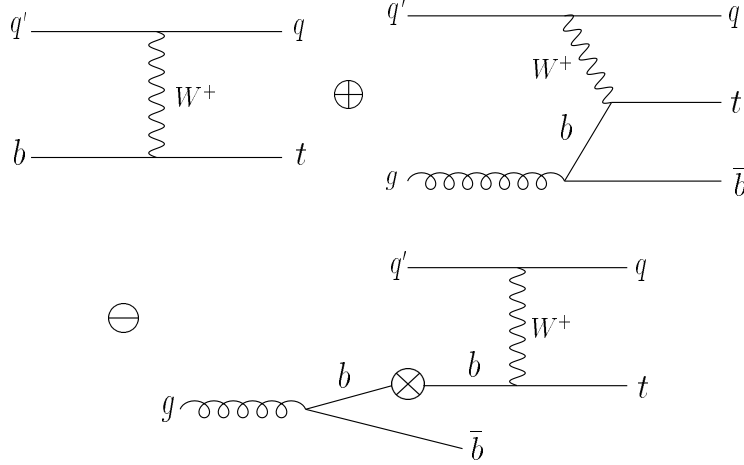
Figure 3.4: Feynman diagrams illustrating the subtraction procedure for calculating the total rate for W–gluon fusion: $q'b \to qt \oplus q'g(W^+g) \to qt\bar{b} \ominus (g \to b\bar{b} \otimes q'b \to qt)$.

$\mathcal{O}(\alpha^2)$ $(2 \to 2)$ process $q'b \to qt$ plus the $\mathcal{O}(\alpha^2\alpha_s)$ $(2 \to 3)$ process $q'g(W^+g) \to qt\bar{b}$ (where the gluon splits to $b\bar{b}$) minus the *splitting* piece $g \to b\bar{b} \otimes q'b \to qt$ in which $b\bar{b}$ are nearly collinear. These processes are shown diagrammatically in Figure 3.4. The helicity amplitudes and the cross sections for these processes are given in Appendices A and B respectively.

The splitting piece is subtracted to avoid double counting the regime in which the b propagator in the $(2 \to 3)$ process is close to on-shell.[2] The procedure is to resum the large logarithm $\alpha_s \ln(m_t^2/m_b^2)$ in the W–gluon fusion process to all orders in α_s and include part of the higher order $\mathcal{O}(\alpha^2\alpha_s)$ corrections to its production rate. (m_b is the mass of the bottom quark.) We note that to obtain the complete $\mathcal{O}(\alpha^2\alpha_s)$ corrections beyond just the leading log contributions one should also include virtual corrections to the $(2 \to 2)$ process, but we shall ignore these non-leading contributions in this work. Using the prescription described as above we found that the total rate of the W–gluon fusion process is about 25% less as compared to the $(2 \to 2)$ event rate for $m_t = 180\,(140)$ GeV regardless of the energy or the type (*i.e.*, pp or $\bar{\text{p}}$p) of the machine. In Figures 3.5 and 3.6 we show the total rate of W–gluon fusion versus m_t with scale $Q = m_t$ as well as a breakdown of the contributing processes at the Tevatron, the Di-TeV and the LHC.

To estimate the uncertainty in the production rate due to the choice of the scale Q in evaluating the strong coupling constant α_s and the parton distributions, we show in Figure 3.7 the scale dependence of the W–gluon fusion rate. As shown in the figure, although the individual rate from either $(2 \to 2)$, $(2 \to 3)$ or the splitting piece is relatively sensitive to the choice of the scale, the total rate as defined by $(2 \to 2) + (2 \to 3) - (\text{splitting piece})$ only varies by about 30% for $M_W/2 < Q < 2m_t$ at the Tevatron. At the Di-TeV and the LHC, it varies by about 30% and 10%, respectively. Based upon the results shown in Figure 3.7, we argue that $Q < M_W/2$ probably is not a good choice as the relevant scale for the production of the top quark from the W–gluon fusion process because the total rate rapidly increases by about a factor of 2 in the low Q regime. In view of the prescription adopted in

---

[2] The total rate of the $(2 \to 3)$ process is extensively discussed in the Appendix C.
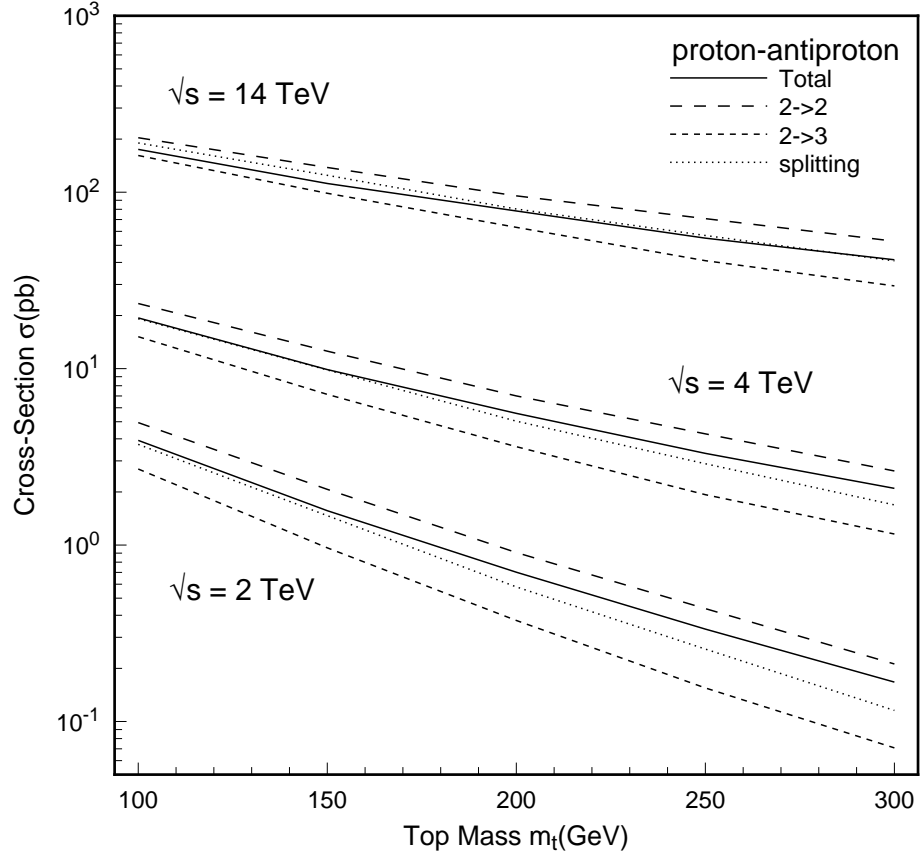
Figure 3.5: Rate in [pb] for single-t production: $q'b \to qt$ $(2 \to 2)$, $q'g \to qt\bar{b}$ $(2 \to 3)$ and the *splitting* piece $g \to b\bar{b} \otimes q'b \to qt$ in which $b\bar{b}$ are collinear. The rates are for $\bar{\text{p}}$p colliders.
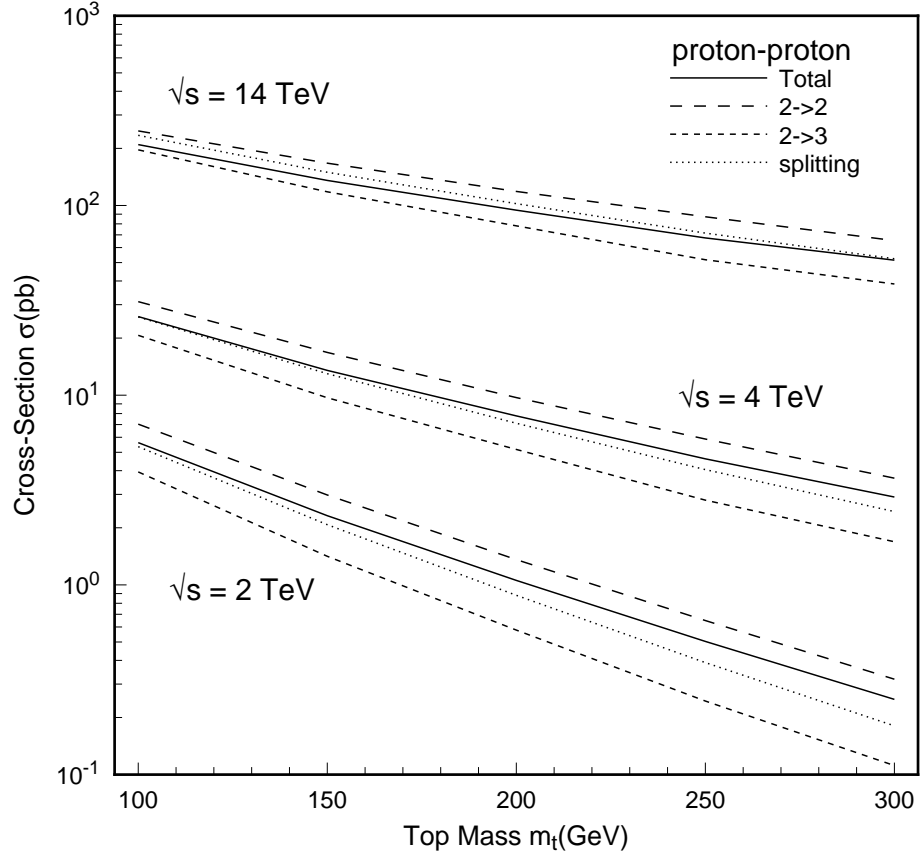
Figure 3.6: Rate in [pb] for single-t production: $q'b \to qt$ $(2 \to 2)$, $q'g \to qt\bar{b}$ $(2 \to 3)$ and the *splitting* piece $g \to b\bar{b} \otimes q'b \to qt$ in which $b\bar{b}$ are collinear. The rates are for pp colliders.
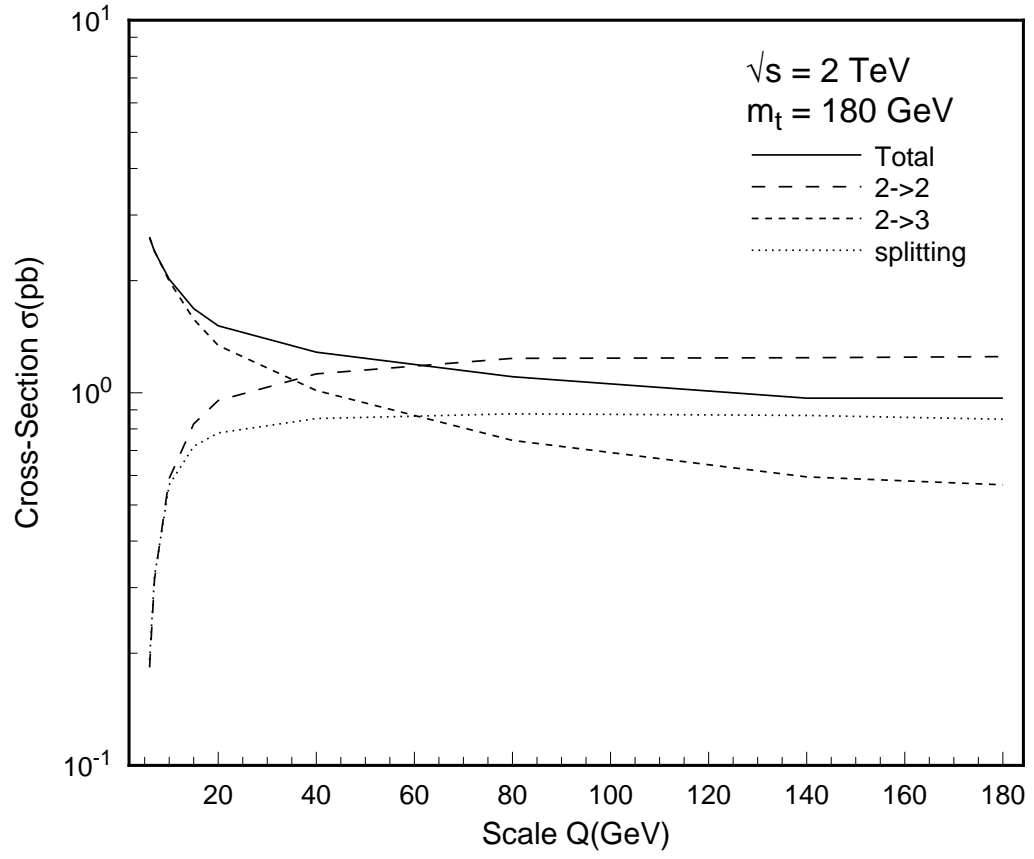
Figure 3.7:   Rate of W–gluon fusion process versus scale Q for $m_t = 180\,\text{GeV}$ and $\sqrt{S} = 2\,\text{TeV}$.

calculating the total rate, the only relevant scales are the top quark mass m_t and the virtuality of the W-line in the scattering amplitudes. Since the typical transverse momentum of the quark (q), which comes from the initial quark (q') after emitting the W-line, is about half of the W–boson mass, the typical virtuality of the W-line is about $M_W/2 \simeq 40\,\text{GeV}$. $m_b \simeq 5\,\text{GeV}$ is thus not an appropriate scale to be used in calculating the W–gluon fusion rate using our prescription. We note that in the $(2 \to 2)$ process the b quark distribution effectively contains sums to order $[\alpha_s \ln(Q/m_b)]^n$ from n-fold collinear gluon emission, whereas the subtraction term (namely, the splitting piece) contains only first order in $\alpha_s \ln(Q/m_b)$. Therefore, as $Q \to m_b$ the $(2 \to 2)$ process picks up only the leading order in $\alpha_s \ln(Q/m_b)$ and so gets largely cancelled in calculating the total rate. Consequently, as shown in Figure 3.7, the total rate is about the same as the $(2 \to 3)$ rate for $Q \to m_b$. We also note that at $Q \simeq M_W/2$, the $(2 \to 2)$ and $(2 \to 3)$ processes have about the same rate. As Q increases the $(2 \to 2)$ rate gradually increases while the $(2 \to 3)$ rate decreases such that the total rate is not sensitive to the scale Q. It is easy to see also that the total rates calculated via this prescription will not be sensitive to the choice of PDF although each individual piece can have different results from different PDF's, based upon the factorization of the QCD theory [30].

Another single-top quark production mechanism is the Drell-Yan type process $q'\bar{q} \to W^* \to t\bar{b}$. As shown in Figures 3.2 and 3.3, for top quarks with mass on the order of $180\,\text{GeV}$ the rate for W^* production is about one fifth that of W–gluon fusion at $\sqrt{S} = 2\,\text{TeV}$. The W^* process becomes much less important for a heavier top quark. This is because at higher invariant masses $\hat{s}$ (for producing a heavier top quark) of the $t\bar{b}$ system, W^* production suffers the usual $1/\hat{s}$ suppression in the constituent cross section. However, in the W–gluon fusion process the constituent cross section does not fall off as $1/\hat{s}$ but flattens out asymptotically to $1/M_W^2$. (The analytical results of these amplitudes are given in Appendix A for reference.) For colliders with higher energies, therefore with large range of $\hat{s}$, the W^* production mechanism for heavy top quarks becomes much less important. However, the kinematics of the top quarks produced from this process are different from those in the W–gluon fusion events. Moreover, possible new physics may introduce a high mass state (say, particle V) to couple strongly with the $t\bar{b}$ system such that the production rate from $q'\bar{q} \to W^* \to V \to t\bar{b}$ can largely deviate from the SM W^* rate.[3] We will however not discuss it in detail here because its rate is highly model dependent.

The W–gluon fusion process becomes more important for a heavier top quark. Why? Effectively, the W–gluon fusion process can be viewed as the scattering of a longitudinal W–boson (W_L) with gluon to produce a top quark and a bottom anti-quark ($W_L^+ g \to t\bar{b}$) after applying the effective-W approximation [32]. For large $\hat{s}$ this scattering process is equivalent to ($\phi^+ g \to t\bar{b}$) where ϕ^+ is the corresponding Goldstone boson of the gauge boson W^+ due to the Goldstone Equivalence Theorem [33, 34]. Since the coupling of t-b-ϕ is proportional to the mass of the top quark, the constituent cross section of the W–gluon fusion process grows like m_t^2/M_W^2 when m_t increases. This explains why the W–gluon fusion rate only decreases slightly as the mass of the top quark increases even though both the parton luminosity and the available phase space decrease for a heavier top quark. In contrast, the $t\bar{t}$ pair production rate from the QCD processes decreases more rapidly as m_t increases because the

---

[3] This is similar to the speculations made in Reference [31] for having some high mass resonance in $t\bar{t}$ production.

constituent cross section of $q\bar{q}$, $gg \to t\bar{t}$ goes as $1/\hat{s}$ and the phase space for producing a $t\bar{t}$ pair is smaller than that for producing a single-t. Therefore, the W–gluon fusion process becomes more important for the production of a heavy top quark.

Before closing this chapter, we note that the Effective-W approximation has been the essential tool used in studying the strongly interacting longitudinal W system to probe the symmetry breaking sector at the supercolliders such as the LHC [35]. By studying single-top production from the W–gluon fusion process at the Tevatron, one can learn about the validity of the Effective-W approximation prior to the supercolliders.

Chapter 4

Measuring the Top Quark Mass

By the year 2000, we expect results from the Tevatron (with $1\,\text{fb}^{-1}$) and results from LEP-200, giving an error of about $50\,\text{MeV}$ on M_W. Due to Veltman's screening theorem, the low energy data are not sensitive to the mass of the Higgs boson [36]. For a heavy Higgs boson, the low energy data can at most depend on m_H logarithmically up to the one loop level. Therefore, within the SM one needs to also know the mass of the top quark to within about $5\,\text{GeV}$ to start getting useful information on m_H with an uncertainty less than a few hundred GeV. This can be done by studying radiative corrections to the low energy data which include LEP, SLC, and neutrino experiments [11, 12, 13, 14]. (Of course, m_H will be measured to better precision if it is detected from direct production at colliders.)

How accurate can the mass of the top quark be measured at hadron colliders? At hadron colliders, m_t can be measured in the $t\bar{t}$ events by several methods [22, 37]. The first method is to use the lepton+jet decay mode of the $t\bar{t}$ pair, as shown in Figure 4.1. This is done by reconstructing the invariant mass of the three jets in the opposite hemisphere from the isolated lepton ℓ ($= e\,\text{or}\,\mu$) in $t \to bW(\to \ell\nu)$, and requiring that two of the three jets reconstruct to a W and the third be tagged as a b-jet. The second method is to use the di-lepton decay mode of the $t\bar{t}$ pair, as shown in Figure 4.2. Here it is required that both W's decay leptonically. In addition, one of the b's must decay semileptonically to measure the mass distribution of the non-isolated lepton ℓ_b (from b decay) and one of the two isolated leptons (ℓ_1 and ℓ_2 from $W^{\pm}$ decay) which is closer to ℓ_b. The third method is to measure the cross section of the di-lepton decay mode of the $t\bar{t}$ pair. At the LHC, there will be about 10^8 $t\bar{t}$ pairs produced in one year of running for $m_t < 200\,\text{GeV}$. With such a large number of events, the ATLAS and CMS collaborations concluded that m_t can be measured with a precision of $\leq 5\,\text{GeV}$ using the first method described above and with about a factor of 2 improvement using the second method [38, 39]. A similar conclusion was also drawn by the CDF and the DØ collaborations for the Tevatron with Main Injector after the upgrade of their detectors [40]. This is remarkable given that the $t\bar{t}$ cross section at the Tevatron is smaller by about two orders of magnitude as compared with that at the LHC, as shown in Figures 3.2 and 3.3.

Next, we would like to discuss how to measure the mass of the top quark in the W–gluon fusion process. Since m_t has been measured by the FNAL CDF and DØ groups in the $t\bar{t}$ events [15, 16], why do we care? To check whether it is a SM top
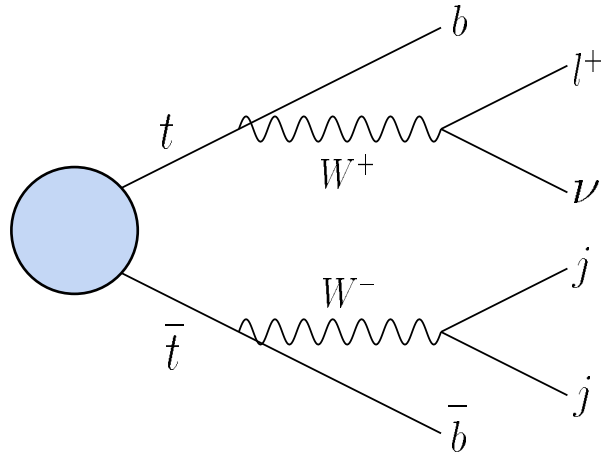
Figure 4.1:   The lepton+jet decay mode of $t\bar{t}$ production.
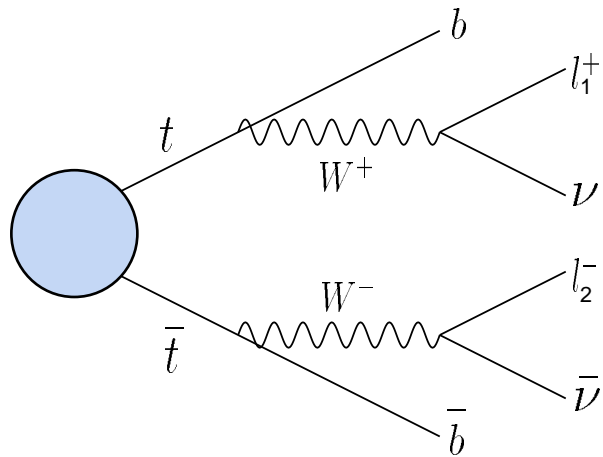
Figure 4.2:   The di-lepton decay mode of $t\bar{t}$ production.

quark, we should verify its production rate predicted by the SM for other production processes such as the single-top quark process.

Suppose the coupling of t-b-W is not of the SM nature, then we would find that the single-top quark production rate of the W–gluon fusion process is different from the SM prediction because its production rate is directly proportional to the square of this coupling. (We will discuss more on this point in Chapter 6.) Hence, without knowing the nature of the t-b-W interactions one can not use the production rates of the single-top quark events to measure m_t. Alternatively, we propose two methods to measure m_t in the single-top quark events. We will refer to them as the fourth and the fifth method. The fourth method is a slight variation of the second method. Instead of measuring the invariant mass of the leptons, we propose to directly measure the invariant mass $(m_{b\ell})$ of the ℓ and b in $t \rightarrow bW(\rightarrow \ell\nu)$. We expect that the efficiency of b tagging using the displaced vertex is higher for detecting a heavier top quark, and the b jet energy measurement is better for b having larger transverse momentum from a heavy top quark decay. Thus $m_{b\ell}$ can be used to measure the mass of a SM top quark. The details of our Monte Carlo study are given in Chapter 8 for a single-top quark event. In the $t\bar{t}$ event there are two b's, therefore this method may not work as well as in the single-top event which only contains one b. However it is not entirely impossible to use this method because, as shown in Figure 4.3, the sum of the invariant mass distributions of $b\ell$ and $\bar{b}\ell$ for a 180 GeV top quark still show a bump near the region that the distribution of $m_{b\ell}$ peaks. (With a larger sample of $t\bar{t}$ events one might be able to afford using the electric charge of the soft-lepton from b-decay to separate b from $\bar{b}$ on an event-by-event basis at the cost of the small branching ratio of $b \rightarrow \mu + X$, of about 10%.) We will explain in more detail how to use f_{Long} (the fraction of longitudinal W–bosons from top quark decay), derived from the distribution of $m_{b\ell}$, to measure m_t in Chapter 6.

The fifth method is to reconstruct the invariant mass of the top quark in the $t \rightarrow bW(\rightarrow \ell\nu)$ decay mode by measuring the missing transverse momentum and choosing a two-fold solution of the longitudinal momentum of the neutrino from the mass constraint of the W boson. In Chapter 8 we conclude that it is possible to measure m_t using either of these last two methods to a precision of $5\,\text{GeV}$ at the Tevatron ($\sqrt{S} = 2\,\text{TeV}$) with $1\,\text{fb}^{-1}$ integrated luminosity. We also find that after applying all the kinematical cuts to suppress the dominant background $W + b\bar{b}$, at most 10% of W^* events contribute to single-top production for a 180 (140) GeV top quark. The SM W^* production rate is already much smaller than the W–gluon fusion rate for a heavier top quark, therefore the contribution from the W^* is not important in our study although we do include its small effects in our analysis as described in Chapter 8.
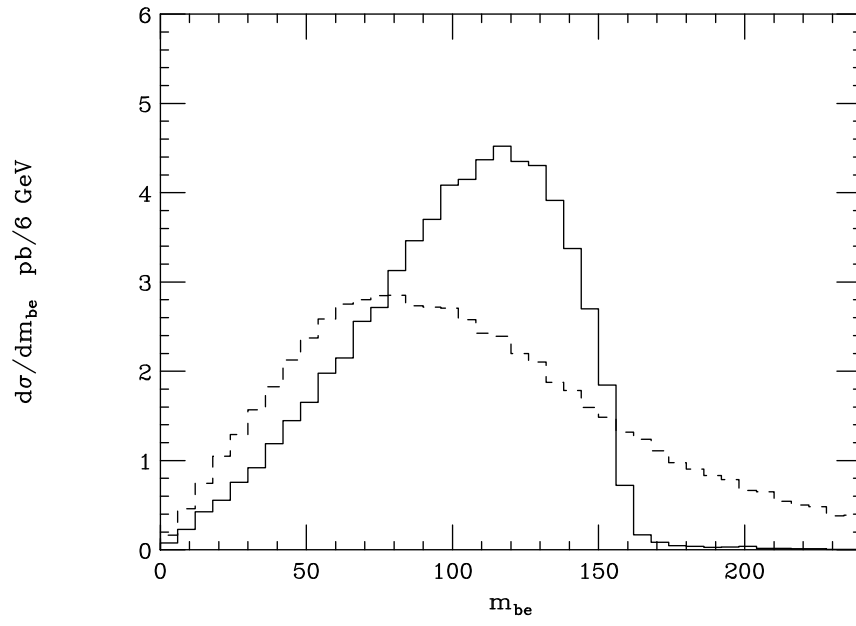
Figure 4.3: Distributions of $m_{b\ell}$ (solid) and $m_{\bar{b}\ell}$ (dash) in $t\bar{t}$ events for a 180 GeV top quark.

Chapter 5

Measuring the Top Quark Width

As shown in Reference [41] the intrinsic width of the top quark can not be measured at a high energy hadron collider such as the LHC through the usual QCD processes.[1] For instance, the intrinsic width of a 150 GeV Standard Model top quark is about 1 GeV, and the full width at half maximum of the reconstructed top quark invariant mass (from $t \to bW(\to jets)$ decay mode) is about 10 GeV after including the detector resolution effects by smearing the final state parton momenta. Here, the ratio of the measured width and the intrinsic width for a 150 GeV top quark is about a factor of 10. For a heavier top quark, this ratio may be slightly improved because the jet energy can be better measured. (The detector resolution $\Delta E/E$ for a QCD jet with energy E is proportional to $1/\sqrt{E}$.) A similar conclusion was also given from a hadron level analysis presented in the SDC Technical Design Report which concluded that reconstructing the top quark invariant mass gave a width of 9 GeV for a 150 GeV top quark [42]. Is there a way to measure the top quark width $\Gamma(t \to bW^+)$, say, within a factor of 2 or better, at hadron colliders? Yes, it can in principle be measured in single-top events.

The width $\Gamma(t \to bW^+)$ can be measured by counting the production rate of top quarks from the W–b fusion process which is *equivalent* to the W–gluon fusion process by a proper treatment of the bottom quark and the W boson as partons inside the hadron. The W–boson which interacts with the b-quark to produce the top quark can be treated as an on-shell boson in the leading log approximation [32, 43]. The result is that even under the approximations considered, a factor of 2 uncertainty in the production rate for this process gives a factor of 2 uncertainty in the measurement of $\Gamma(t \to bW^+)$. This is already much better than what can be measured from the invariant mass distribution of the jets from the decay of top quarks in the $t\bar{t}$ events produced via the usual QCD processes. More precisely, as argued in Chapter 3, the production rate of single-top events at the Tevatron can probably be known within about 30%, thus it implies $\Gamma(t \to bW^+)$ can be measured to about the same accuracy.[2]

---

[1] In Reference [41], the effects of QCD radiation in top quark decay (at one loop level) to the measurement of m_t in $t\bar{t}$ events produced in hadron collisions was studied. It was concluded that the peak position of the m_t distribution remains about the same as the tree level result, but the shape is different. It was also found that the $m_{b\ell}$ distribution is not sensitive to QCD radiation in top decay.

[2] Strictly speaking, from the production rate of single-top events, one measures the sum of all the

Therefore, this is an extremely important measurement because it directly tests the couplings of t-b-W.

W–gluon fusion can also tell us about the CKM matrix element $|V_{tb}|$. Assuming only three generations of quarks, the constraints from low energy data together with unitarity of the CKM matrix require $|V_{tb}|$ to be in 0.9988 to 0.9995 at the 90% confidence level [5]. As noted in Reference [5] the low energy data do not preclude there being more than three generations of quarks (assuming the same interactions as described by the SM). Moreover, the entries deduced from unitarity might be altered when the CKM matrix is expanded to accommodate more generations. When there are more than three generations the allowed ranges (at 90% CL) of the matrix element $|V_{tb}|$ can be anywhere between 0 and 0.9995 [5]. Since $|V_{tb}|$ is directly involved in single-top production via W–gluon fusion, any deviation from SM value in $|V_{tb}|$ will either enhance or suppress the production rate of single-top events. It can therefore be measured by simply counting the single-top event rates. For instance, if the single-top production rate is measured to within 30%, then $|V_{tb}|$ is determined to within 15%.

In conclusion, after the top quark is found, the branching ratio of $t \to bW^+(\to \ell^+\nu)$ can be measured from the ratio of $(2\ell + jets)$ and $(1\ell + jets)$ rates in $t\bar{t}$ events. The measured single-top quark event rate is equal to the single-top production rate multiplied by the branching ratio of $t \to bW^+(\to \ell^+\nu)$ for the $(1\ell + jets)$ mode and the same t-b-W couplings appearing in the decay of t in this process appear also in the production of t. Thus, a model independent measurement of the decay width $\Gamma(t \to bW^+)$ can be made by simply counting the production rate of t in the W–gluon fusion process. Should the top quark width be found to be different from the SM expectations, we would then have to look for non-standard decay modes of the top quark. We note that it is important to measure at least one partial width (say, $\Gamma(t \to bW^+)$) precisely in order to discriminate between different models of new physics, if any. In the SM, the partial width $\Gamma(t \to bW^+)$ is about the same as the total width of the top quark at the tree level because of the small CKM matrix element $|V_{ts}|$, thus measuring the single-top quark production rate measures the lifetime of the top quark.

---

possible partial decay widths, such as $\Gamma(t \to bW^+) + \Gamma(t \to sW^+) + \Gamma(t \to dW^+) + \cdots$, therefore, this measurement is really measuring the width of $\Gamma(t \to XW^+)$ where X can be more than one particle state as long as it originates from the partons inside the proton (or anti-proton). In the SM, $\Gamma(t \to bW^+)$ is about equal to the total width of the top quark.

Chapter 6

Top Quark Couplings to the W Gauge Boson

It is equally important to ask what kind of interactions the t-b-W vertex might involve [44]. For instance, one should examine the form factors of t-b-W which result from higher order corrections due to SM strong and/or electroweak interactions. It is even more interesting to examine these form factors to test the plausibility of having *nonuniversal* gauge couplings of t-b-W due to some dynamical symmetry breaking scenario [45, 19].

The QCD [46] and the electroweak [47] corrections to the decay process $t \to bW^+$ in the SM have been done in the literature. The most general operators for this coupling are described by the interaction lagrangian

$$
\begin{aligned}
L = \quad & \frac{g}{\sqrt{2}} \left[W_\mu^- \bar{b} \gamma^\mu (f_1^L P_- + f_1^R P_+) t - \frac{1}{M_W} \partial_\nu W_\mu^- \bar{b} \sigma^{\mu\nu} (f_2^L P_- + f_2^R P_+) t \right] \\
& + \frac{g}{\sqrt{2}} \left[W_\mu^+ \bar{t} \gamma^\mu (f_1^{L*} P_- + f_1^{R*} P_+) b - \frac{1}{M_W} \partial_\nu W_\mu^+ \bar{t} \sigma^{\mu\nu} (f_2^{R*} P_- + f_2^{L*} P_+) b \right] ,
\end{aligned}
$$

$$(6.1)$$

where $P_\pm = \frac{1}{2}(1 \pm \gamma_5)$, $i\sigma^{\mu\nu} = -\frac{1}{2}[\gamma^\mu, \gamma^\nu]$ and the superscript $*$ denotes the complex conjugate. In general, the form factors $f_1^{L,R}$ and $f_2^{L,R}$ can be complex. Note that in Equation (6.1), if there is a relative phase between f_1^L and f_2^R or between f_1^R and f_2^L, then CP is violated. For instance, in the limit of $m_b = 0$, a CP-violating observable will have a coefficient proportional to $\text{Im}(f_1^L f_2^{R*})$ for a left-handed bottom quark, and $\text{Im}(f_1^R f_2^{L*})$ for a right-handed bottom quark [44]. (We will discuss more on CP violation in Chapter 7.) If the W–boson can be off–shell then there are additional form factors such as

$$\partial^\mu W_\mu^- \bar{b}(f_3^L P_- + f_3^R P_+) t + \partial^\mu W_\mu^+ \bar{t}(f_3^{R*} P_- + f_3^{L*} P_+) b , \qquad (6.2)$$

which vanish for an on–shell W–boson or when the off–shell W–boson couples to massless on–shell fermions. Here, we only consider on–shell W–bosons for $m_t >$

$M_W + m_b$. At tree level in the SM the form factors are $f_1^L = 1$ and $f_1^R = f_2^L = f_2^R = 0$. These form factors will in general affect the experimental observables related to the top quark, such as the fraction of longitudinal W's produced in top quark decays.

The fraction (f_{Long}) of longitudinally polarized W–bosons, produced in the rest frame of the decaying top quark, strongly depends on the form factors $f_1^{L,R}$ and $f_2^{L,R}$, as shown in Appendix C. Hence, f_{Long} is a useful observable for measuring these form factors. The definition of f_{Long} is simply the ratio of the number of longitudinally polarized W–bosons produced with respect to the total number of W–bosons produced in top quark decays:

$$f_{\text{Long}} = \frac{\Gamma(\lambda_W = 0)}{\Gamma(\lambda_W = 0) + \Gamma(\lambda_W = -) + \Gamma(\lambda_W = +)}. \tag{6.3}$$

We use $\Gamma(\lambda_W)$ to refer to the decay rate for a top quark to decay into a W–boson with polarization λ_W. ($\lambda_W = -, +, 0$ denotes a left-handed, right-handed, and longitudinal W–boson.) Clearly, the polarization of the W–boson depends on the form factors f_1 and f_2.[1] Therefore, one can measure the polarization of the W–boson to measure these form factors. As shown in Appendix C, the polarization of the W–boson can be determined by the angular distribution of the lepton, say, e^+ in the rest frame of W^+ in the decay mode $t \to bW^+(\to e^+\nu)$. However, the reconstruction of the W–boson rest frame (to measure its polarization) could be a non-trivial matter due to the missing longitudinal momentum (P_z) (with a two-fold ambiguity) of the neutrino (ν) from W decay. Fortunately, as shown in Equation (6.4), one can determine the polarization of the W–boson without reconstructing its rest frame by using the Lorentz-invariant observable m_{be}, the invariant mass of b and e from t decay.

The polar angle $\theta_{e^+}^*$ distribution of the e^+ in the rest frame of the W^+ boson, whose z-axis is defined to be the moving direction of the W^+ boson in the rest frame of the top quark, can be written in terms of m_{be} through the following derivation:

$$\cos\theta_{e^+}^* = \frac{E_e E_b - p_e \cdot p_b}{|\vec{\mathbf{p}}_e||\vec{\mathbf{p}}_b|}$$

$$\simeq 1 - \frac{p_e \cdot p_b}{E_e E_b} = 1 - \frac{2m_{be}^2}{m_t^2 - M_W^2}. \tag{6.4}$$

The energies E_e and E_b are evaluated in the rest frame of the W^+ boson from the top quark decay and are given by

$$E_e = \frac{M_W^2 + m_e^2 - m_\nu^2}{2M_W}, \qquad |\vec{\mathbf{p}}_e| = \sqrt{E_e^2 - m_e^2},$$

$$E_b = \frac{m_t^2 - M_W^2 - m_b^2}{2M_W}, \qquad |\vec{\mathbf{p}}_b| = \sqrt{E_b^2 - m_b^2}. \tag{6.5}$$

---

[1] The fraction of longitudinal W's in top quark decays contributed from the form factor f_1^R is the same as that from f_1^L [44].

m_e (m_ν) denotes the mass of e^+ (ν_e) for the sake of bookkeeping. The first line in Equation (6.4) is exact when using Equation (6.5), while the second line of Equation (6.4) holds in the limit of $m_b = 0$. It is now trivial to find f_{Long} by first calculating the $\cos\theta^*_{e+}$ distribution then fitting it according to the decay amplitudes of the W–boson from top quark decay, as given in the Appendix C. In what follows we will show how to use the distribution of m_{be} to measure the mass of the top quark and its couplings to the W–boson.

In Reference [19], we considered the effective couplings

$$W - t_L - b_L : \quad \frac{g}{2\sqrt{2}}\frac{1 + \kappa^{CC}_L}{2}\gamma_\mu(1 - \gamma_5) \tag{6.6}$$

and

$$W - t_R - b_R : \quad \frac{g}{2\sqrt{2}}\frac{\kappa^{CC}_R}{2}\gamma_\mu(1 + \gamma_5) \tag{6.7}$$

derived from an electroweak chiral lagrangian with the symmetry $\text{SU}(2)_L \times \text{U}(1)_Y$ broken down to $\text{U}(1)_{\text{EM}}$. (Here, $\kappa^{CC}_L = f^L_1 - 1$, and $\kappa^{CC}_R = f^R_1$.) At the Tevatron and the LHC, heavy top quarks are predominantly produced from the QCD process $gg, q\bar{q} \to t\bar{t}$ and the W–gluon fusion process $qg(Wg) \to t\bar{b}, \bar{t}b$. In the former process, one can probe $\kappa_L{}^{CC}$ and $\kappa_R{}^{CC}$ from the decay of the top quark to a bottom quark and a W–boson. In the latter process, these non-standard couplings can also be measured by simply counting the production rates of signal events with a single t or $\bar{t}$. Let us discuss $\kappa_L{}^{CC}$ and $\kappa_R{}^{CC}$ in more detail as follows.

6.1 From the Decay of Top Quarks

To probe $\kappa_L{}^{CC}$ and $\kappa_R{}^{CC}$ from the decay of the top quark to a bottom quark and a W–boson, one needs to measure the polarization of the W–boson, which can be measured from the distribution of the invariant mass $m_{b\ell}$. For a massless b, the W–boson from top quark decay can only be either longitudinally or left-hand polarized for a left-hand charged current ($\kappa_R{}^{CC} = 0$). For a right-hand charged current ($\kappa_L{}^{CC} = -1$) the W–boson can only be either longitudinally or right-hand polarized. (Note that the handedness of the W–boson is reversed for a massless $\bar{b}$ from $\bar{t}$ decays.) This is a consequence of helicity conservation, as diagrammatically shown in Figures 6.1 and 6.2 for a polarized top quark. In these figures we show the preferred moving direction of the lepton from a polarized W–boson in the rest frame of a polarized top quark for either a left-handed or a right-handed t-b-W vertex. As indicated in these figures, the invariant mass $m_{b\ell}$ depends on the polarization of the W–boson from the decay of a polarized top quark. Also, $m_{b\ell}$ is preferentially larger for a pure right-handed t-b-W vertex than a pure left-handed one. This is clearly shown in Figure 6.3, in which the peak of the $m_{b\ell}$ distribution is shifted to the right and the distribution falls off sharply at the upper mass limit for a pure right-handed t-b-W vertex. In terms of $\cos\theta^*_\ell$, their difference is shown in Figure 6.4. However, in both cases the fraction (f_{Long}) of longitudinal W's from top quark decay is enhanced by

(a) left-handed top
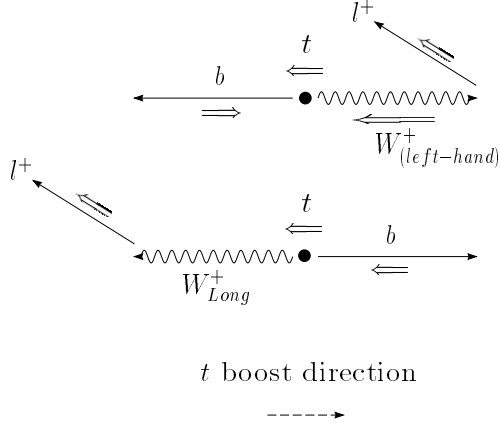
(b) right-handed top
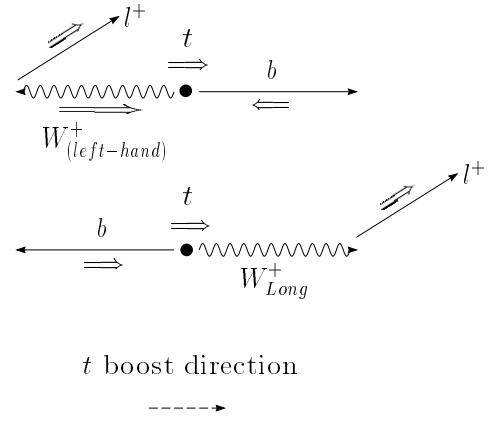
Figure 6.1:   For a left-handed t-b-W vertex.

(a) left-handed top
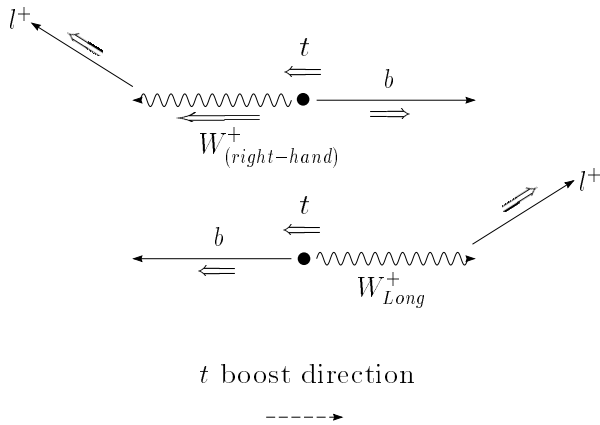
(b) right-handed top
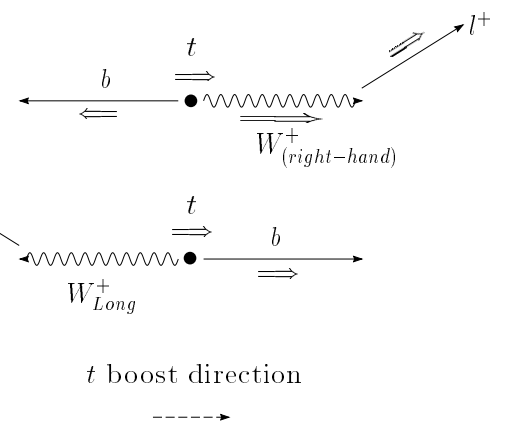
Figure 6.2:   For a right-handed t-b-W vertex.
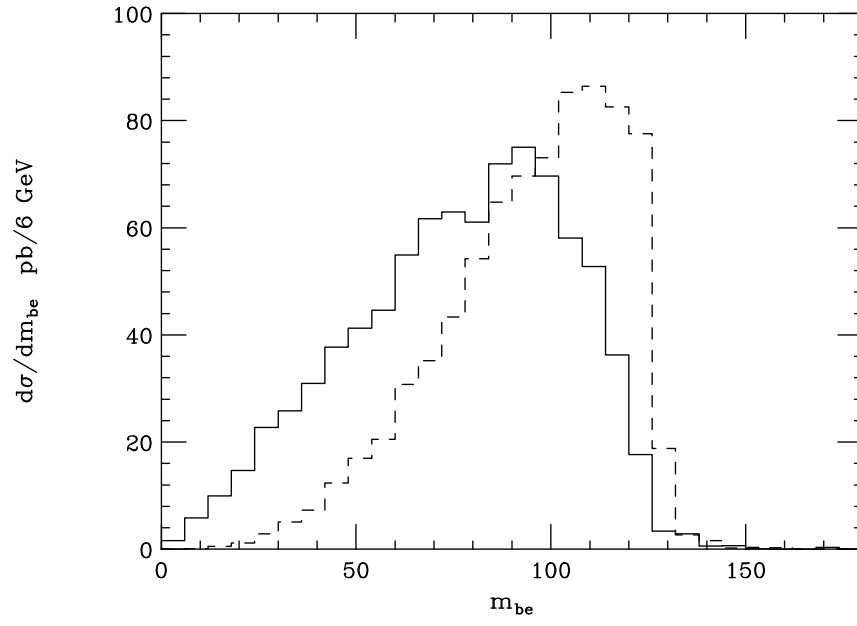
Figure 6.3: $m_{b\ell}$ distribution for SM top quark (solid) and for pure right-handed t-b-W coupling of tbW (dash).
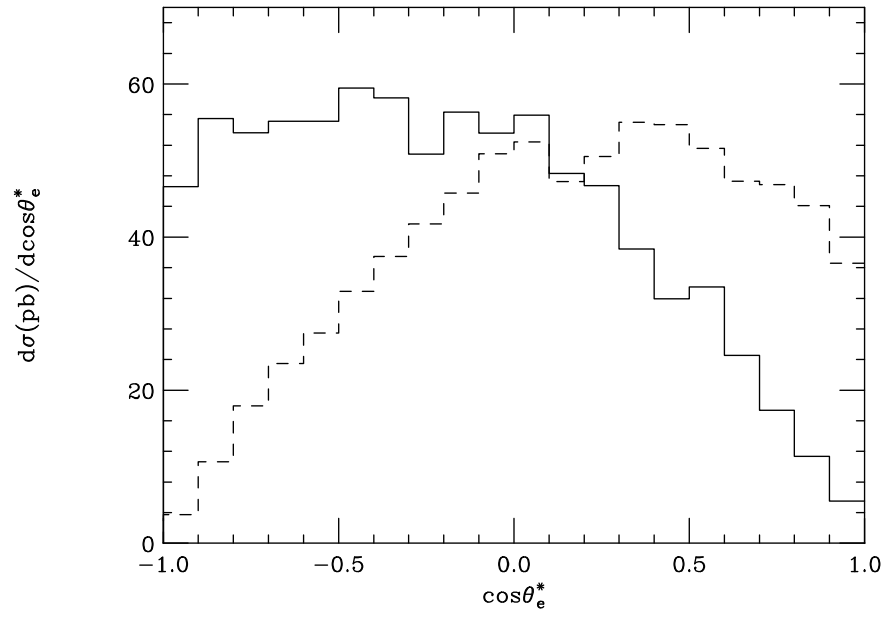
Figure 6.4: $\cos\theta^*_\ell$ distribution for SM top quark (solid) and for pure right-hand t-b-W coupling of tbW (dash).

$m_t{}^2/2M_W{}^2$ as compared to the fraction of transversely polarized W's [44], namely,

$$f_{\text{Long}} = \frac{\frac{m_t^2}{2M_W^2}}{1 + \frac{m_t^2}{2M_W^2}} \; . \tag{6.8}$$

Therefore, for a heavier top quark, it is more difficult to untangle the $\kappa_L{}^{CC}$ and $\kappa_R{}^{CC}$ contributions. On the other hand, because of the very same reason, the mass of a heavy top quark can be accurately measured from f_{Long} (discussed below) irrespective of the nature of the t-b-W couplings (either left-handed or right-handed).

The QCD production rate of $t\bar{t}$ is obviously independent of $\kappa_L{}^{CC}$ and $\kappa_R{}^{CC}$. (Here we assume the electroweak production rate of $q\bar{q} \to A, Z \to t\bar{t}$ remains small as in the SM.) Let us estimate how well the couplings $\kappa_L{}^{CC}$ and $\kappa_R{}^{CC}$ can be measured at the Tevatron, the Di-TeV, and the LHC. First, we need to know the production rates of the top quark pairs from the QCD processes. As shown in Table 3.1, the QCD production rate of $gg, q\bar{q} \to t\bar{t}$ for a $180\,\text{GeV}$ top quark is about $4.5\,\text{pb}$, $26\,\text{pb}$ and $430\,\text{pb}$ at the Tevatron, the Di-TeV, and the LHC, respectively. For simplicity, let's consider the $\ell^\pm + \geq 3$ jet decay mode whose branching ratio is $\text{Br} = 2\frac{2}{9}\frac{6}{9} = \frac{8}{27}$, where the charged lepton $\ell^\pm$ can be either $e^\pm$ or $\mu^\pm$. We assume the experimental detection efficiency (ϵ), which includes both the kinematic acceptance and the efficiency of b-tagging, to be 15% for the signal event [48]. Let's further assume that there is no ambiguity in picking up the right b ($\bar{b}$) to combine with the charged lepton ℓ^+ (ℓ^-) to reconstruct t (or $\bar{t}$), then in total there are $4.5\,\text{pb} \times 10^3\,\text{pb}^{-1} \times \frac{8}{27} \times 0.15 = 200$ reconstructed $t\bar{t}$ events to be used in measuring $\kappa_L{}^{CC}$ and $\kappa_R{}^{CC}$ at $\sqrt{S} = 2\,\text{TeV}$. The same calculation at the Di-TeV and the LHC yields 1100 and 19000 reconstructed $t\bar{t}$ events, respectively. Given the number of reconstructed top quark events, one can fit the $m_{b\ell}$ distribution to measure $\kappa_L{}^{CC}$ and $\kappa_R{}^{CC}$. For example we have done a study for the Tevatron. Let us assume the effects of new physics only modify the SM results ($f_1^L = 1$ and $f_1^R = 0$ at Born level) slightly and the form factors $f_2^{L,R}$ are as small as expected from the usual dimensional analysis [49, 50].[2] We summarize our results on the accuracy of measuring $f_1^{L,R}$ for various luminosities in Table 6.1 [51]. (Only statistical errors are included at the 95% confidence level.)

In the same table (*i.e.*, Table 6.1) we also show our estimate on how well the mass of the top quark m_t can be measured from f_{Long}. By definition of f_{Long}, for a SM top quark (*i.e.*, $f_1^L = 1$ and $f_1^R = 0$), the distribution of $\cos\theta_\ell^*$ has the functional form

$$F(\cos\theta_\ell^*) \sim (1 - f_{\text{Long}}) \left(\frac{1 - \cos\theta_\ell^*}{2} \right)^2 + f_{\text{Long}} \left(\frac{\sin\theta_\ell^*}{\sqrt{2}} \right)^2 \; . \tag{6.9}$$

---

[2] The coefficients of the form factors $f_2^{L,R}$, assumed to be induced through loop effects, will be a factor of $\frac{1}{16\pi^2}$ smaller than that of the form factors $f_1^{L,R}$.

Table 6.1: Results on the accuracy of measuring $f_1^{L,R}$ for various luminosities. (Only statistical errors are included at the 95% confidence level.)

Integrated Luminosity fb^{-1}	Number of reconstructed $t\bar{t}$ events.	$\frac{\Delta f_1^L}{f_1^L}$	Δf_1^R	$\frac{\Delta m_t}{m_t}$
1	200	8%	±0.5	4%
3	600	4%	±0.3	2%
10	2000	2%	±0.2	1%

Therefore, f_{Long} can be calculated by fitting with the distribution of $\cos\theta_\ell^*$, or equivalently with the distribution of $m_{b\ell}$. We prefer to measure κ_L^{CC} and κ_R^{CC} using the distributions of $m_{b\ell}$ than of $\cos\theta_\ell^*$ because the former can be directly calculated from the measured momenta of b and ℓ. However, to convert from the distributions of $m_{b\ell}$ to $\cos\theta_\ell^*$, as given in Equation (6.4), the effects from the width of the W–boson and the top quark might slightly distort the distribution of $\cos\theta_\ell^*$. (Notice that in the full calculation of the scattering amplitudes the widths of the W–boson and the top quark have to be included in the Breit-Wigner form to generate a finite event rate.)

However, in reality, the momenta of the bottom quark and the charged lepton will be smeared by detector effects and another problem in this analysis is the identification of the right b to reconstruct t. There are three possible strategies to improve the efficiency of identifying the right b. One is to demand a large invariant mass of the $t\bar{t}$ system so that t is boosted and its decay products are collimated. Namely, the right b will be moving closer to the lepton from t decay. This can be easily enforced by demanding leptons with a larger transverse momentum. Another is to identify the soft (non-isolated) lepton from $\bar{b}$ decay (with a branching ratio $\text{Br}(\bar{b} \to \mu^+ X) \sim 10\%$). The other is to statistically determine the electric charge of the b-jet (or $\bar{b}$-jet) to be $1/3$ (or $-1/3$) [52]. All of these methods may further reduce the reconstructed signal rate by an order of magnitude. How will these affect our conclusion on the determination of the non-universal couplings κ_L^{CC} and κ_R^{CC}? It can only be answered by detailed Monte Carlo studies which are yet to be done.

6.2 From the Production of Top Quarks

Here we propose another method to measure the couplings κ_L^{CC} and κ_R^{CC} from the production rate of the single-top quark process.

For $m_t = 180$ GeV, the sum of the production rates of single-t and single-$\bar{t}$ events is about $2\,\text{pb}$ and $14\,\text{pb}$ for $\sqrt{S} = 2\,\text{TeV}$ and $\sqrt{S} = 4\,\text{TeV}$ respectively. The branching ratio of interest is $\text{Br} = \frac{2}{9}$. The kinematic acceptance of this event at $\sqrt{S} = 2\,\text{TeV}$ is about 0.55, as shown in Chapter 8. Assuming the efficiency of b-tagging is about

30%, then there will be $2\,\mathrm{pb} \times 10^3\,\mathrm{pb}^{-1} \times \frac{2}{9} \times 0.55 \times 0.3 = 75$ events reconstructed for a $1\,\mathrm{fb}^{-1}$ integrated luminosity. At $\sqrt{S} = 4\,\mathrm{TeV}$, as shown in Chapter 8, the kinematic acceptance of this event is about 0.40 which, from the above calculation, yields about 3700 reconstructed events for $10\,\mathrm{fb}^{-1}$ integrated luminosity. Based on statistical error alone, this corresponds to a 12% and 2% measurement on the single-top cross section. A factor of 10 increase in the luminosity of the collider can improve the measurement by a factor of 3 statistically. Taking into account the theoretical uncertainties, as discussed in Chapter 3, we examine two scenarios: 20% and 50% error on the measurement of the cross section for single-top production. The results, which are not sensitive to the energies of the colliders considered here (either 2 TeV or 4 TeV), are shown in Figure 6.5 for a 180 GeV top quark at the Tevatron. We found that $\kappa_L{}^{CC}$ and $\kappa_R{}^{CC}$ are well constrained inside the region bounded by two (approximate) ellipses (cf. Appendix A). To further determine the sizes of $\kappa_L{}^{CC}$ and $\kappa_R{}^{CC}$ one needs to study the kinematics of the decay products, such as the charged lepton ℓ, of the top quark. Since the top quark produced from the W–gluon fusion process is almost one hundred percent left-hand (right-hand) polarized for a left-hand (right-hand) t-b-W vertex, the charged lepton ℓ^+ from t decay has a harder momentum for a right-handed t-b-W coupling than for a left-handed coupling. (Note that the couplings of light-fermions to W–boson have been well tested from the low energy data to be left-handed as described in the SM.) As shown in Figures 6.1 and 6.2, this difference becomes smaller when the top quark is much heavier because the W–boson from the top quark decay tends to be more longitudinally polarized.

A right-hand charged current is absent in a linearly $SU(2)_L$ invariant gauge theory with massless bottom quark. In this case, $\kappa_R{}^{CC} = 0$, then $\kappa_L{}^{CC}$ can be constrained to within about $-0.08 < \kappa_L{}^{CC} < 0.03$ ($-0.20 < \kappa_L{}^{CC} < 0.08$) with a 20% (50%) measurement on the production rate of single-top quark at the Tevatron [19]. (Here we assume the experimental data agrees with the SM prediction within 20% (50%).) This means that if we interpret $(1 + \kappa_L{}^{CC})$ as the CKM matrix element $|V_{tb}|$, then $|V_{tb}|$ can be bounded as $|V_{tb}| > 0.9$ (or 0.75) for a 20% (or 50%) measurement on the single-top production rate.

Before closing this chapter, we remark that in the Refs. [19] and [53] some bounds on the couplings of $\kappa_L{}^{CC}$ and $\kappa_R{}^{CC}$ were obtained by studying the low energy data with the assumption that the effects of new physics at low energy can only modify the couplings of $\kappa_L{}^{CC}$ and $\kappa_R{}^{CC}$ but not introduce any other light fields in the effective theory. However, nature might not behave exactly in this way. It is possible that some light fields may exist just below the TeV scale, then the bounds obtained from Refs. [19] and [53] may no longer hold. Thus, it is important to have direct measurements on all the form factors listed in Equation (6.1) from the production of top quarks, in spite of the present bounds on κ's derived from radiative corrections to low energy data.
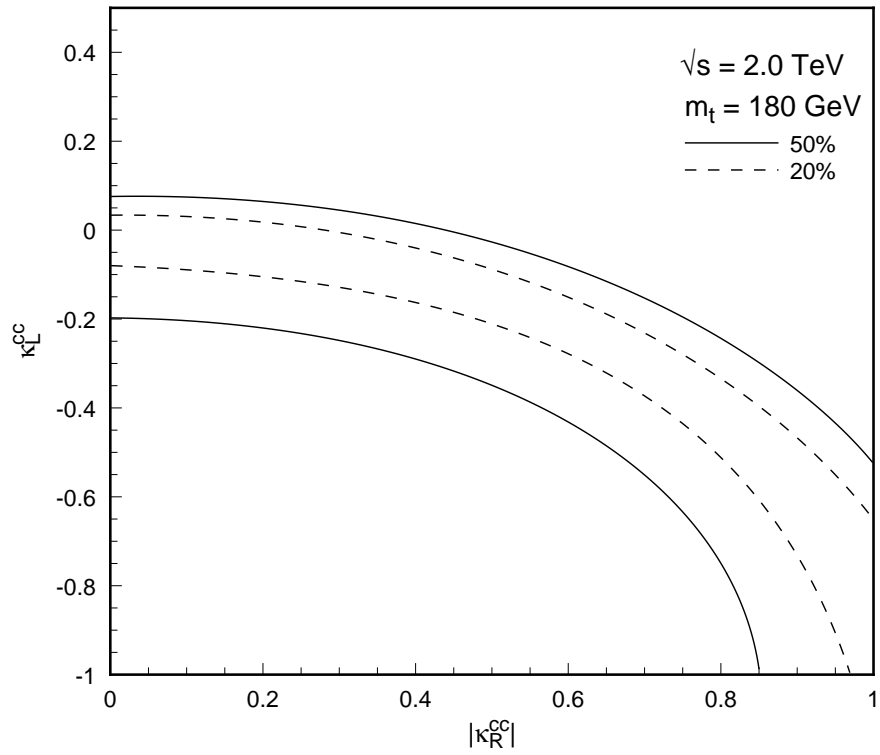
Figure 6.5: Constraint on $|\kappa_L{}^{CC}|$ and $\kappa_R{}^{CC}$ given 20% and 50% error in measurement of Standard Model rate for W–gluon fusion. Curves are identical for $m_t = 140$ GeV and $m_t = 180$ GeV.

Chapter 7

Probing CP Properties in Top Quarks

It is known that explicit CP violation requires the presence of both the CP non-conserving vertex and the complex structure of the physical amplitude. Due to the origin of this complex structure, the possible CP-violating observables can be separated into two categories. In the first category, this complex structure comes from the absorptive part of the amplitude due to the final state interactions. In the second category, this complex structure does not arise from the absorptive phase but from the correlations in the kinematics of the initial and final state particles involved in the physical process. Hence, it must involve a triple product correlation (*i.e.*, a Levi-Civita tensor).

To distinguish the symmetry properties between these two cases, we introduce the transformation $\hat{\mathrm{T}}$, as defined in Reference [54], which is simply the application of time reversal to all momenta and spins without interchanging initial and final states. The CP-violating observables in the first category are CP-odd and CP$\hat{\mathrm{T}}$-odd, while those in the second category are CP-odd and CP$\hat{\mathrm{T}}$-even. Of course, both of them are CPT-even.

To illustrate the above two categories, we consider CP-violating observables for the decay of the top quark. Consider the partial rate asymmetry

$$\mathcal{A}_{bW} \;\; \equiv \;\; \frac{\Gamma(t \to bW^+) - \Gamma(\bar{t} \to \bar{b}W^-)}{\Gamma(t \to bW^+) + \Gamma(\bar{t} \to \bar{b}W^-)}. \tag{7.1}$$

A non-vanishing $\mathcal{A}_{bW}$ clearly violates CP and CP$\hat{\mathrm{T}}$, therefore this observable belongs to the first category. We note that because of CPT invariance, the total decay width of the top quark $\Gamma(t)$ has to equal the total decay width of the top anti-quark $\Gamma(\bar{t})$. Thus, any non-zero $\mathcal{A}_{bW}$ implies that there exists a state (or perhaps more than one state) X such that t can decay into X and $\bar{t}$ into $\bar{X}$. The absorptive phase of $t \to bW^+$ is therefore generated by re-scattering through state X, *i.e.*, $t \to X \to bW^+$, where $X \neq bW^+$ because the final state interaction should be off-diagonal [55].

Next, let's consider the observable of the second category. In the decay of $t \to bW^+(\to \ell^+\nu_\ell)$, for a polarized t quark, time reversal invariance (T) is violated if the expectation value of

$$\vec{\sigma}_t \times \vec{p}_b \cdot \vec{p}_{\ell+} \tag{7.2}$$

is not zero [44]. Assuming CPT invariance, this implies CP is violated. Therefore, this observable is CP-odd but $\text{CP}\hat{\text{T}}$-even. A non-vanishing triple product observable, such as that in Equation (7.2), from the decay of the top quark violates T. However, it may be entirely due to final state interaction effects without involving any CP-violating vertex. To construct a truly CP-violating observable, one must combine information from both the t and $\bar{t}$ quarks. For instance, the difference in the expectation values of $\vec{\sigma}_t \times \vec{p}_b \cdot \vec{p}_{\ell+}$ and $\vec{\sigma}_{\bar{t}} \times \vec{p}_{\bar{b}} \cdot \vec{p}_{\ell-}$ would be a true measure of an intrinsic CP violation.

There have been many studies on how to measure the CP-violating effects in the $t\bar{t}$ system produced in either electron or hadron collisions. (For a review, see a recent paper in Reference [56].) At hadron colliders, the number of $t\bar{t}$ events needed to measure a CP-violating effect of the order of $10^{-3} - 10^{-2}$ is about $10^7 - 10^8$. To examine the potential of various current and future hadron colliders in measuring the CP-violating asymmetries, we estimate the total event rates of $t\bar{t}$ pairs for a 180 GeV SM top quark produced at these colliders. At the Tevatron, the Di-TeV and the LHC, an integrated luminosity of 10, 100 and 100 fb^{-1} will produce about 4.5×10^4, 2.6×10^6 and 4.3×10^7 $t\bar{t}$ pairs, respectively, as given in Table 3.1. Therefore, the LHC would be able to probe the CP asymmetry of the top quark at the level of a few percent. A similar number of the $t\bar{t}$ pairs is required in electron collisions to probe the CP asymmetry at the same level. Thus, for a $\sqrt{S} = 500\,\text{GeV}$ e^-e^+ collider, an integrated luminosity of about $10^4 - 10^5$ fb^{-1} has to be delivered. This luminosity is at least a factor of 100 higher than the planned next linear colliders. We note that although the initial state in a pp collision (such as at the LHC) is not an eigenstate of a CP transformation, these CP-odd observables can still be defined as long as the production mechanism is dominated by gg fusion. This is indeed the case for $t\bar{t}$ pair production at the LHC.

In the SM, the top quark produced via the W–gluon fusion process is about one hundred percent left-hand (longitudinally) polarized, see Appendix A. Given a polarized top quark, one can use the triple product correlation, as defined in Equation (7.2), to detect CP violation of the top quark. For a polarized top quark, one can either use $\vec{\sigma}_t \times \vec{p}_b$ or $\vec{p}_t^{\text{Lab}} \times \vec{p}_b$ to define the decay plane of $t \to bW(\to \ell^+\nu)$. Obviously, the latter one is easier to implement experimentally. Define the asymmetry to be

$$\mathcal{A}_{io} \equiv \frac{N(\ell^+ \text{ out of the decay plane}) - N(\ell^+ \text{ into the decay plane})}{N(\ell^+ \text{ out of the decay plane}) + N(\ell^+ \text{ into the decay plane})} . \tag{7.3}$$

If $\mathcal{A}_{io}$ is not zero, then the time-reversal T is not conserved, therefore CP is violated for a CPT invariant theory. Due to the missing momentum of the neutrino from the decay of the W–boson, it is difficult to reconstruct the azimuthal angle (ϕ_W) of the W–boson from the decay of the top quark. Once the angle ϕ_W is integrated over, the transverse polarization of the top quark averages out and only the longitudinal polarization of the top quark contributes to the asymmetry $\mathcal{A}_{io}$. Thus, the asymmetry $\mathcal{A}_{io}$ can be used to study the effects of CP violation in the top quark, which in the

SM is about one hundred percent left-hand (longitudinally) polarized as produced from the W–gluon fusion process. To apply the CP-violating observable $\mathcal{A}_{io}$, one needs to reconstruct the directions of both the t and b quarks. It has been shown in Reference [57] that it takes about $10^7 - 10^8$ single-top events to detect CP violation at the order of $\sim 10^{-3} - 10^{-2}$.

For $m_t = 180\,\text{GeV}$ at the Tevatron, the Di-TeV and the LHC, an integrated luminosity of 10, 100 and 100 fb^{-1} will produce about 2×10^4, 1.4×10^6 and 2×10^7 single-t or single-$\bar{t}$ events, respectively, from Table 3.1. At the NLC, the single top quark production rate is much smaller. For a 2 TeV electron collider, the cross sections for $e^- e^+ \rightarrow e^- \bar{\nu}_e t \bar{b}$ and $e^+ \gamma \rightarrow \bar{\nu}_e t \bar{b}$ are 8 fb and 60 fb, respectively [58]. Hence, it will be extremely difficult to detect CP violation effects at the order of $\leq 10^{-2}$ in the single-top events produced in electron collisions.

A few comments are in order. First, to extract the *genuine* CP-violating effects, we need to study the difference in the asymmetry $\mathcal{A}_{io}$ measured in the single-t and single-$\bar{t}$ events because the time-reversal violation in $\mathcal{A}_{io}$ of the t (or $\bar{t}$) alone could be generated by final state interactions without CP-violating interactions. Second, the detection efficiency for this method is not close to one, so a good understanding of the kinematics of the decay products and how the detector works are needed to make this method useful.

The asymmetry $\mathcal{A}_{io}$ belongs to the second category of CP-violating observables and is CP-odd and CP$\hat{\text{T}}$-even. Consider another asymmetry $\mathcal{A}_t$ which belongs to the first category of CP-violating observables and is CP-odd and CP$\hat{\text{T}}$-odd. Using $\mathcal{A}_t$ for detecting CP-violating effects is to make use of the fact that $\bar{\text{p}}\text{p}$ is a CP eigenstate; therefore, the difference in the production rates for $\bar{\text{p}}\text{p} \rightarrow tX$ and $\bar{\text{p}}\text{p} \rightarrow \bar{t}X$ is a signal of CP violation. This asymmetry is defined to be

$$
\mathcal{A}_t \equiv \frac{\sigma(\bar{\text{p}}\text{p} \rightarrow tX) - \sigma(\bar{\text{p}}\text{p} \rightarrow \bar{t}X)}{\sigma(\bar{\text{p}}\text{p} \rightarrow tX) + \sigma(\bar{\text{p}}\text{p} \rightarrow \bar{t}X)} \quad . \tag{7.4}
$$

As discussed in Chapter 6, the production rate of $\bar{\text{p}}\text{p} \rightarrow tX$ is proportional to the decay rate of $t \rightarrow bW^+$ and the rate of $\bar{\text{p}}\text{p} \rightarrow \bar{t}X$ is proportional to the rate of $\bar{t} \rightarrow \bar{b}W^-$. This implies that $\mathcal{A}_t = \mathcal{A}_{bW}$, cf. Equation (7.1). There have been quite a few models studied in the literature about the asymmetry in $\mathcal{A}_{bW}$. For instance, in the Supersymmetric Standard Model where a CP-violating phase may occur in the left-handed and right-handed top-squark, $\mathcal{A}_{bW}$ can be as large as a few percent depending on the details of the parameters in the model [59].

Next, let's examine how many top quark events are needed to detect a few percent effect in the CP-violating asymmetry $\mathcal{A}_t$. Consider $t \rightarrow bW^+ \rightarrow b\ell^+\nu$, where $\ell = e$ or μ. Define the branching ratio B_W as the product of $\text{Br}(t \rightarrow bW^+)$ and $\text{Br}(W^+ \rightarrow \ell^+\nu)$, where $\text{Br}(W^+ \rightarrow \ell^+\nu)$ is 2/9. ($\text{Br}(t \rightarrow bW^+)$ depends on the details of a model and is almost 1 in the SM.) Let us assume that the efficiency of b-tagging (ϵ_{btag}) is about 30% and the kinematic acceptance (ϵ_k) of reconstructing the single-top event, $\bar{\text{p}}\text{p} \rightarrow tX \rightarrow bW^+X \rightarrow b\ell^+\nu X$, is about 50%. (See, a Monte Carlo study in Chapter 8.) The number of single-t and single-$\bar{t}$ events needed to measure $\mathcal{A}_t$ is

$$
\mathcal{N}_t = \frac{1}{B_W \epsilon_{\text{btag}} \epsilon_k} \left(\frac{1}{\mathcal{A}_t} \right)^2 \quad . \tag{7.5}
$$

Thus, to measure $\mathcal{A}_t$ of a few percent, $\mathcal{N}_t$ has to be as large as $\sim 10^6$, which corresponds to an integrated luminosity of $100\,\mathrm{fb}^{-1}$ at the Di-TeV.

Chapter 8

A Monte Carlo Study

It was shown in Reference [24] that due to the characteristic features of the transverse momentum and rapidity distributions of the spectator quark which emitted the virtual W an almost perfect efficiency for "kinematic b tagging" can be achieved. In addition, the ability of performing b-tagging using a vertex detector increases the detection efficiency of a heavy top quark produced via the W–gluon fusion process. In this chapter we show that this process is useful at the Tevatron with the Main Injector. We also estimate results for $\sqrt{S} = 4$ TeV at the Di-TeV and for $\sqrt{S} = 14$ TeV at the LHC in separate subsections.

To show that a heavy top quark produced from the W–gluon fusion process can be detected at the Tevatron, we performed a Monte Carlo study on the $W + 2\,jets$ mode of the $(2 \to 2)$ process

$$q'b \to qt(\to bW^+(\to \ell^+\nu)) \tag{8.1}$$

with $\ell^+ = e^+$ or μ^+. More specifically, we assume that the b-quark jet from the top quark decay can be tagged so that the decay mode of interest is identified to be $W + b + jet$. Throughout this study, we assume that the efficiency of the b-quark tagging is 30% for $P_t^b > 30\,\mathrm{GeV}$ with no misidentifications of a b-jet from other QCD jets. For clarity we only give rates for top quark (not including top-antiquark) production in this chapter, unless specified otherwise. To include the top-antiquark production one can refer to Chapter 3 for its production rate as compared with that of a top quark.

For simplicity we only consider the intrinsic backgrounds (*i.e.*, those present at the parton level) for the $W + b + jet$ final state, and will not invoke any detailed study on effects due to hadronization of the partons or the imperfectness of the detectors used in experiments. The intrinsic backgrounds in the SM for the mode $W + b + jet$ are the electroweak-QCD process $q'\bar{q} \to W + b + \bar{b}$ and QCD process $q\bar{q},\ gg \to t\bar{t} \to W + b + jet$. We will show that the dominant backgrounds for the single-top signal come from the electroweak-QCD processes (as shown in Figure 8.1)

$$u\bar{d},\ c\bar{s} \to b\bar{b}W^+(\to \ell^+\nu). \tag{8.2}$$

The other backgrounds such as $cg \to bW^+$ are suppressed due to the small CKM matrix element $|V_{cb}| \simeq 0.03\,\mathrm{to}\,0.048$ [5]. As done in the previous sections, we will give our numerical results in this section for either a $140\,\mathrm{GeV}$ or a $180\,\mathrm{GeV}$ top quark.

44

8.1 Tevatron with $\sqrt{S} = 2\,\text{TeV}$

At the Tevatron ($\bar{\text{p}}\text{p}$, $\sqrt{S} = 2\,\text{TeV}$) the single-top production rate from the W–gluon fusion process is 1(2) pb, as shown in Table 3.1. For the final state of Equation (8.1), the branching ratio of $t \to bW^+(\to \ell^+\nu)$ for $\ell^+ = e^+$ or μ^+ is about 2/9 in the SM. As discussed in Chapter 3, we found that after properly treating the b quark as a parton inside the proton (or antiproton) the total rate for the W–gluon fusion process is about 30% smaller than that of the $(2 \to 2)$ process. Hereafter, we shall rescale all the numerical results of our analysis for the $(2 \to 2)$ process to the total event rate of the W–gluon fusion process by multiplying them by a factor of 0.7.

To show that a 180 (140) GeV top quark produced from this process can be detected at the Tevatron, we first impose the following kinematic cuts:

$$P_T^q > 15\,\text{GeV}, \quad |\eta^q| < 3.5,$$

$$P_T^\ell > 15\,\text{GeV}, \quad |\eta^\ell| < 2,$$

$$P_T^b > 35\,\text{GeV}, \quad |\eta^b| < 2,$$

$$\not{E}_T > 15\,\text{GeV}, \quad \Delta R_{qb} > 0.7 \ . \tag{8.3}$$

The efficiency of these cuts for a 180 (140) GeV top quark is 32%(53%). Including the reduction factor from the assumed b-tagging efficiency, 30%, the signal rate is found to be about 0.045 (0.063) pb. In Equation (8.3), P_T stands for transverse momentum, η for pseudo-rapidity, $\not{E}_T$ for missing transverse momentum, and $\Delta R = \sqrt{(\delta\eta)^2 + (\delta\phi)^2}$ with ϕ being the azimuthal angle. It is important to note in Figure 8.2 that the typical rapidity of the spectator jet in the signal event is about 1.6 although almost all the signal events have $|\eta^q| < 3.5$ [24]. The distribution of η^q is asymmetric because the Tevatron is a $\bar{\text{p}}\text{p}$ collider. To produce a heavy top quark, which decays to a positively charged lepton, the valence quark from the proton is most important, implying a large probability for η^q to be positive. (We define the positive z-direction to be the proton moving direction in the laboratory frame.) Similarly, a top-antiquark produced from the W–gluon fusion process would prefer a negative η^q due to the large up-antiquark PDF inside the antiproton.

In the $W + b\bar{b}$ background process, the $b\bar{b}$ pair comes from a virtual gluon conversion, therefore its rate is highly suppressed if the invariant mass of the $b\bar{b}$ pair is
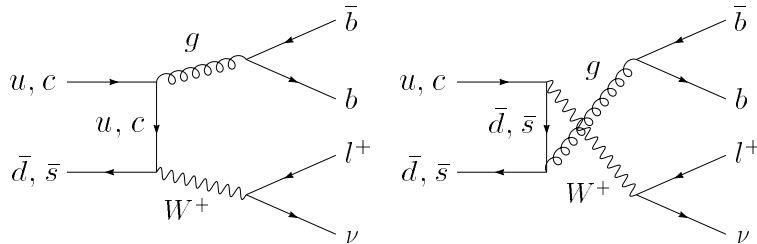
Figure 8.1: Diagrams for $u\bar{d}$, $c\bar{s} \to b\bar{b}W^+(\to \ell^+\nu)$.
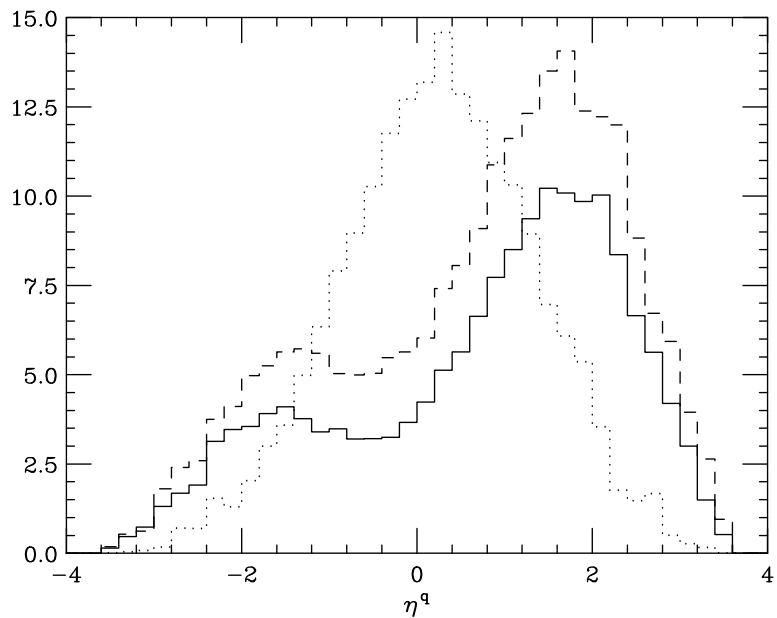
Figure 8.2:   The rapidity distribution of the spectator quark q, after cuts in Equation (8.3), for the signal $q'b \rightarrow qt(\rightarrow bW^+(\rightarrow \ell^+\nu))$, and of the spectator quark $\bar{b}$ for the major background $q'\bar{q} \rightarrow \bar{b}bW^+(\rightarrow \ell^+\nu)$ (dots), for $m_t = 180\,\text{GeV}$ (solid) and $140\,\text{GeV}$ (dash), at the Tevatron. (The vertical scale is arbitrary, but the relative size among these curves are absolute.)

large. Since both b and $\bar{b}$ have about the same transverse momentum (P_T) in the background event, the requirement of $P_T^b > 35\,\mathrm{GeV}$ effectively forces a similar P_T cut on $\bar{b}$. This generates a large invariant mass of b and $\bar{b}$ (*i.e.*, the virtuality of the gluon), strongly suppressing the background rate. In contrast, in the signal event the final parton q (from q', after emitting a virtual W) typically has a smaller P_T than the b-quark (from the decay of a heavy top quark). Typically, in the signal event, $P_T^b \simeq m_t/3$. In Figure 8.3 we show the P_T distribution of the tagged b from t in both the signal and the background events. Hence, demanding an asymmetric cut on P_T (*i.e.*, $P_T^q > 15\,\mathrm{GeV}$ and $P_T^b > 35\,\mathrm{GeV}$) will suppress background effectively and keep most of the signal events. This is why an asymmetric cut on P_T was used in our analysis to suppress the major background process $W + b\bar{b}$. To compare the efficiency of this asymmetric cut in P_T, we note that using $P_T^b > 15$ GeV along with all the other cuts in (8.3) yields a signal-to-background ratio (S/B) of about $1/3(2/3)$. Requiring $P_T^b > 35$ GeV excludes about 60% of the background events sacrificing about 10%(30%) of the signal.

After imposing the kinematic cuts in Equation (8.3), we found that S/B $\simeq 0.9(1.3)$. However, the signal-to-background ratio can be further improved by imposing

$$\cos\theta_{\ell q} > -0.4. \tag{8.4}$$

Because the top quark produced from the W–gluon fusion process is left-hand polarized, ℓ^+ tends to move against the moving direction of the top quark in the center-of-mass frame of q and t, cf. Figure 6.1. However, in the background event, the distribution of $\cos\theta_{\ell q}$, as shown in Figure 8.4, is almost flat after imposing the cuts of (8.3). ($\theta_{\ell q} = \pi - \theta_\ell$, where θ_l is the the polar angle of ℓ^+ in the rest frame of t defined in the center-of-mass frame of q and t.)

To calculate $\cos\theta_{\ell q}$, the P_z^ν information must be constructed. Since both ℓ^+ and ν come from a real W^+ boson, we can use the W–boson mass constraint

$$M_W^2 = (p_\ell + p_\nu)^2 \tag{8.5}$$

and the $\displaystyle{\not}E_T$ information to specify the longitudinal momentum P_z^ν of the neutrino. There are two solutions for P_z^ν and typically, both of them are physical solutions for a signal event. Therefore, one has to fix a prescription to choose the one which will most likely give the correct distribution of the invariant mass of ℓ^+, ν and b. We choose the solution which has the smaller $|P_z^\nu|$. Here we exploit the fact that the W has finite width. If a physical solution for P_z^ν is not found with $M_W = 80$ GeV, we generate a resonant mass of the W–boson using a Breit-Wigner distribution. We use a full half-maximum width of the W–boson, where $\Gamma_W = 2.1\,\mathrm{GeV}$, and solve for P_z^ν, repeating the algorithm for up to three trials if necessary. We found that the survival probability for finding a solution using this algorithm is about 90%, and the difference between this solution and the value actually generated by the Monte Carlo generator is a Gaussian distribution peaking at 0 with a width about the order of Γ_W. After the additional cut imposed on $\cos\theta_{\ell q}$, we obtained S/B $\simeq 1.2(1.8)$. About 55%(40%) of the total signal event rate remains after applying the cuts (8.3) and (8.4) to the

process (8.1). We conclude that for an integrated luminosity of $1\,\mathrm{fb}^{-1}$ at a $2\,\mathrm{TeV}$ $\bar{p}p$

collider, there will be about 75(105) signal events detected with a significance S/$\sqrt{B}$ of about 10(14), including both the single-t and single-$\bar{t}$ events as defined in (8.1).
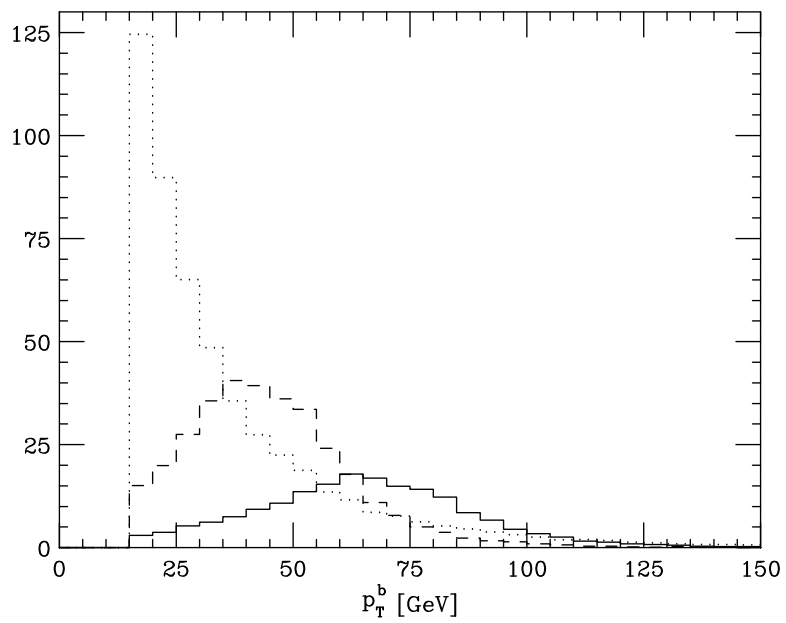
Figure 8.3: P_T distribution of the b quark, after requiring $P_T^b > 15\,\text{GeV}$ along with all the other cuts in (8.3), for the signal $q'b \to qt(\to bW^+(\to \ell^+\nu))$, and the major background $q'\bar{q} \to \bar{b}bW^+(\to \ell^+\nu)$, at the Tevatron.
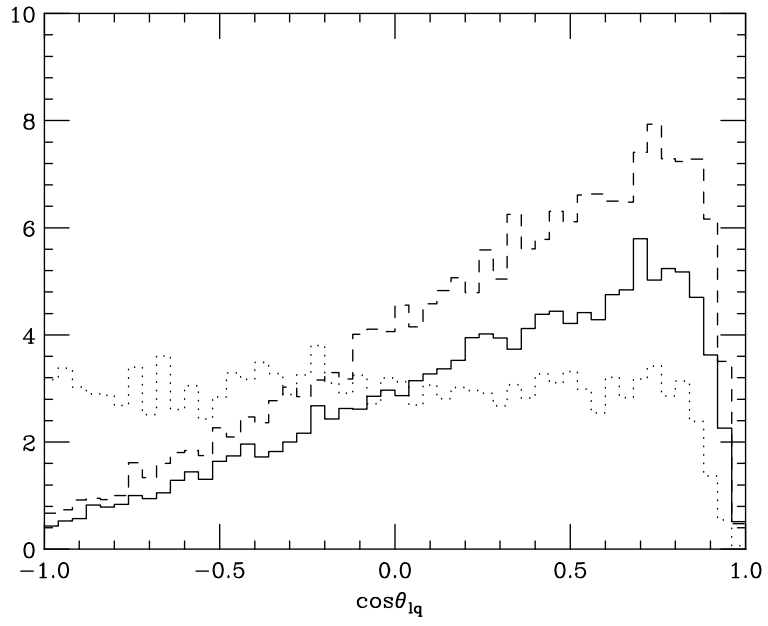
Figure 8.4: The $\cos\theta_{\ell q}$ distribution prior to cut Equation (8.4) for the signal $q'b \to qt(\to bW^+(\to \ell^+\nu))$ and the major background $q'\bar{q} \to \bar{b}bW^+(\to \ell^+\nu)$, at the Tevatron.
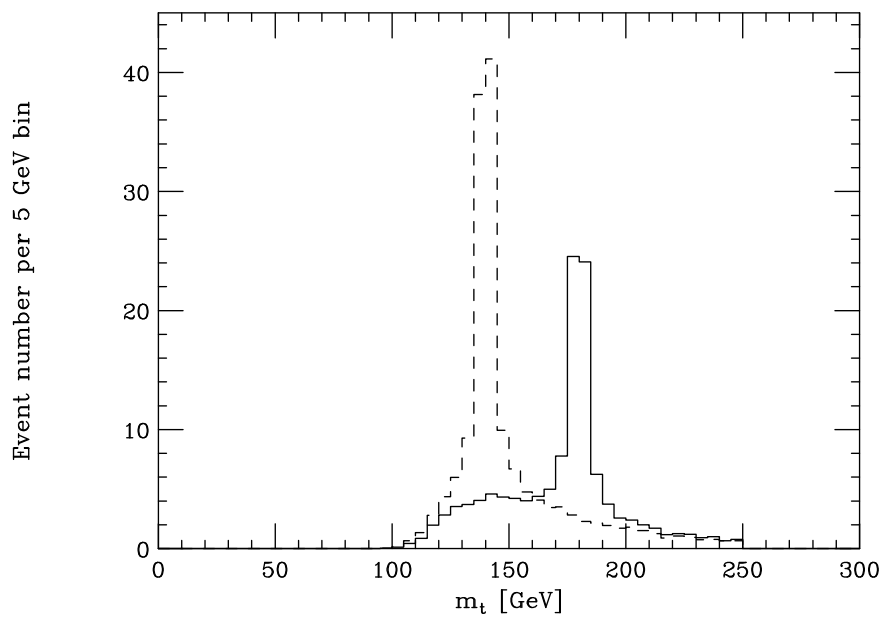
Figure 8.5: The m_t distribution after the cuts Equation (8.3) and Equation (8.4) for $m_t = 180$ GeV (solid) and 140 GeV (dash) at the Tevatron including both the signal and background events with $W^\pm \rightarrow e^\pm$ or $\mu^\pm$.

To measure the mass of the top quark, we calculate the reconstructed invariant mass (m_t) of the top quark using

$$m_t^2 = (p_b + p_\ell + p_\nu)^2. \tag{8.6}$$

The distribution of m_t, including both the signal and the backgrounds, is shown in Figure 8.5, in which a clear mass peak appears unmistakably. Therefore, we conclude that the top quark can be detected and studied via this process at the Tevatron. In Figure 8.5, other less important backgrounds, such as $t\bar{t}$ events, were also included.

The $t\bar{t}$ background is not important after vetoing the events with more than 2 jets [24]. To support this we did a study for the two decay modes of $t\bar{t}$:

$$t\bar{t} \rightarrow bW^+(\rightarrow \ell^+\nu)\,\bar{b}W^-(\rightarrow q'\bar{q}) \tag{8.7}$$

and

$$t\bar{t} \rightarrow bW^+(\rightarrow \ell^+\nu)\,\bar{b}W^-(\rightarrow \ell_2^-\bar{\nu}), \qquad \ell_2 = e \text{ or } \mu. \tag{8.8}$$

For both modes we require one of the jets to be a b or $\bar{b}$.

Consider first the $\bar{t} \rightarrow \bar{b}q'\bar{q}$ decay mode. We require at least one of the q'- and $\bar{q}$-jets and $\bar{b}$ (if b is tagged) or b (if $\bar{b}$ is tagged) to be within rapidity 3.5, otherwise we reject the event. If any one (and only one) of the untagged jets is within rapidity 3.5 we call it the spectator jet and then apply our cuts. If two of the untagged jets are within rapidity 3.5, then we require their ΔR separation to be less than 0.7 to classify them as one spectator jet. When all three untagged jets are within rapidity 3.5 we choose the jet with the largest P_T and check its ΔR separation with the other two. If the lower P_T jets are within $\Delta R = 0.7$ of the high P_T jet, we call this the spectator jet and apply our cuts, otherwise, reject the event. Recall from Table 3.1 for a 180 GeV top quark, the $t\bar{t}$ rate is about 4.5 pb. After applying the cuts (8.3) and (8.4) and including the branching ratio for this mode, $\frac{2}{9}\frac{6}{9} = \frac{4}{27}$, the event rate, of approximately 3×10^{-4} pb, is very small as compared with the signal rate of 0.075 pb (including t and $\bar{t}$). This is because for most of the $\bar{t} \rightarrow \bar{b}q'\bar{q}$ decay modes all three jets are within rapidity 3.5 and ΔR_{bj} and $\Delta R_{\bar{b}j}$ are in general large .

For the $\bar{t} \rightarrow \bar{b}\ell_2^-\bar{\nu}$ decay mode we require that ℓ_2 be undetected. Specifically, if ℓ_2 is within rapidity 2 with $P_T^{\ell_2} > 15\,\text{GeV}$ we reject the event. If $2 < |\eta^{\ell_2}| < 3.5$ we require $P_T^{\ell_2}$ to be less than the minimum P_T for detecting leptons, *i.e.*, $< 15\,\text{GeV}$ in accordance with Equation (8.3). After the cuts in (8.3), this mode (with branching ratio $\frac{2}{9}\frac{2}{9} = \frac{4}{81}$) already suffers, being about 5% of the signal rate. This mode suffers another factor of about two loss to the failure of reconstructing P_z^ν due to the presence of two neutrinos in the final state. After imposing the $\cos\theta_{\ell q}$ cut the rate for $t\bar{t} \rightarrow bW^+(\rightarrow \ell^+\nu)\,\bar{b}W^-(\rightarrow \ell_2^-\bar{\nu})$ is about 3×10^{-3} pb which is about a factor of 25 smaller than the signal rate. Hence the dominant background (of the same order as the signal rate) comes from the electroweak-QCD processes as given in Equation (8.2).

As summarized in Figure 8.5, even with the very minimum kinematic cuts of (8.3) and (8.4) the single-top signal can already be detected, assuming a perfect detector with b-tagging efficiency of 30%. To incorporate the effects of detector efficiencies,

we smear the final state parton momenta using a Gaussian distribution with

$$(\Delta E/E)_\ell = 15\%/\sqrt{E}, \quad \text{and} \quad (\Delta E/E)_{q,b} = 50\%/\sqrt{E}. \tag{8.9}$$

The m_t distribution becomes slightly broader as shown in Figure 8.6; however, both the signal and the background rates are almost the same as those obtained with a perfect detector. As discussed in the previous chapters, the distribution of the invariant mass $m_{b\ell}$ is extremely useful in either determining the mass of the top quark or measuring the form factors of t-b-W. For completeness we show in Figure 8.7 the distribution of $m_{b\ell}$ with or without smearing, after all the above analysis. Because the b-jet is required to have large P_T, cf. Equation (8.3), so $\Delta E/E$ for the b-jet is small, therefore the two $m_{b\ell}$ distributions do not differ much and the difference becomes smaller for larger $m_{b\ell}$. Thus, the position of the bump at large $m_{b\ell}$ in the signal events remain a good signature for detecting the single-top signals and determining the mass of the top quark (discussed in Chapter 4) or the couplings of t-b-W (discussed in Chapter 6).

We note that the data sample obtained after all the above analysis can be further purified at the cost of somewhat reducing the signal rates. This can be easily done, for instance, by noting the distinct differences between the signal events and the background events from the distributions of rapidity of the spectator jet (Figure 8.2), transverse momentum of the bottom quark (Figure 8.3), and the angular correlation $\cos\theta_{\ell q}$ (Figure 8.4) due to the polarization of the top quark in signal events. However, for a more realistic simulation, one should also consider the possibility of having a charm-jet (or even an ordinary QCD-jet) faking a bottom jet in b-tagging so that the actual background rate measured by the detector would be larger than that given here. This is outside the scope of our parton level study.

As discussed in Chapter 3, another process which produces a single-top is the W^* production

$$q'\bar{q} \to W^* \to t\bar{b}. \tag{8.10}$$

At 2 TeV for a 180 (140) GeV top quark, the W^* production rate is about $1/5(1/3)$ of the W–gluon fusion rate. Applying the kinematic cuts defined in Equation (8.3) we find that the W^* process passes with about the same efficiency as the W–gluon fusion process. However, there are a few obvious differences in the kinematics of their final state partons. First, in the W^* event, there are two b-jets (one for b from t decay and another for $\bar{b}$ from production), therefore there is a 50% chance of tagging the wrong b and giving the wrong reconstructed top quark invariant mass, as defined in Equation (8.6). To improve the invariant mass distribution of the top quark, one has to be able to distinguish a b-jet from a $\bar{b}$-jet by making further selections at the cost of reducing the single-top rate from this process. (Some of the techniques have been discussed in Chapter 4.) Second, the rapidity distribution of the spectator jet (*i.e.*, $\bar{b}$-jet if b-jet identified) in the W^* event peaks around zero (*i.e.*, central, as shown in Figure 8.8) because $t\bar{b}$ is produced through the s–channel process.[1] This is in contrast to that in the W–gluon fusion event where the rapidity distribution (η^q)

---

[1] We note that the rapidity distribution of the $\bar{b}$-quark in the $W^* \to t\bar{b}$ event is slightly asymmetric around zero. It favors a slightly negative rapidity. (Recall that in the W–gluon events for producing single-t, the rapidity of the spectator quark q favors positive values.) This is similar to the lepton rapidity asymmetry observed in the $\bar{p}p \to W^+ \to \ell^+\nu$ events due to the ratio of the down-quark and the up-quark parton distributions inside the proton and the anti-proton.
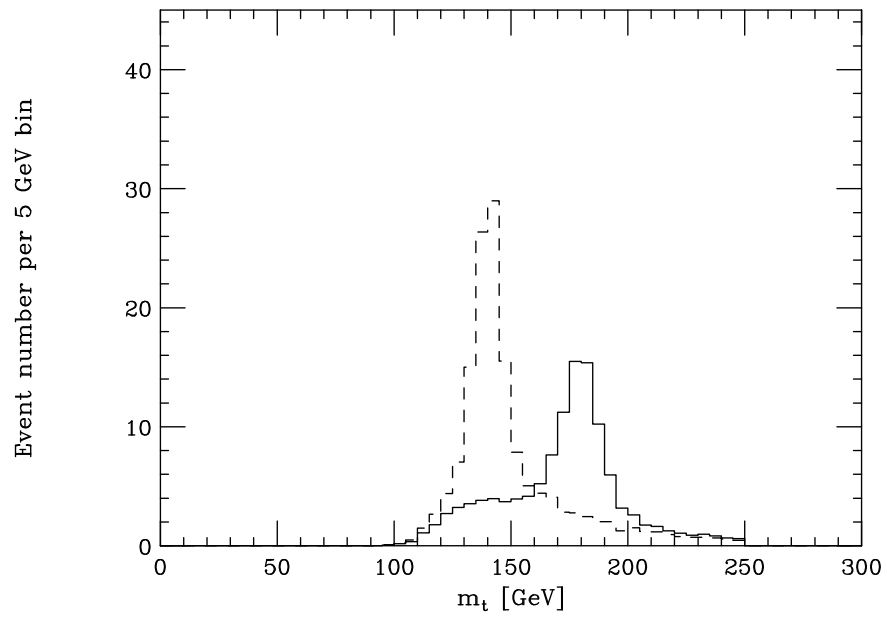
Figure 8.6: Same as Figure 8.5, but with detector resolution effects as described in Equation 8.9.
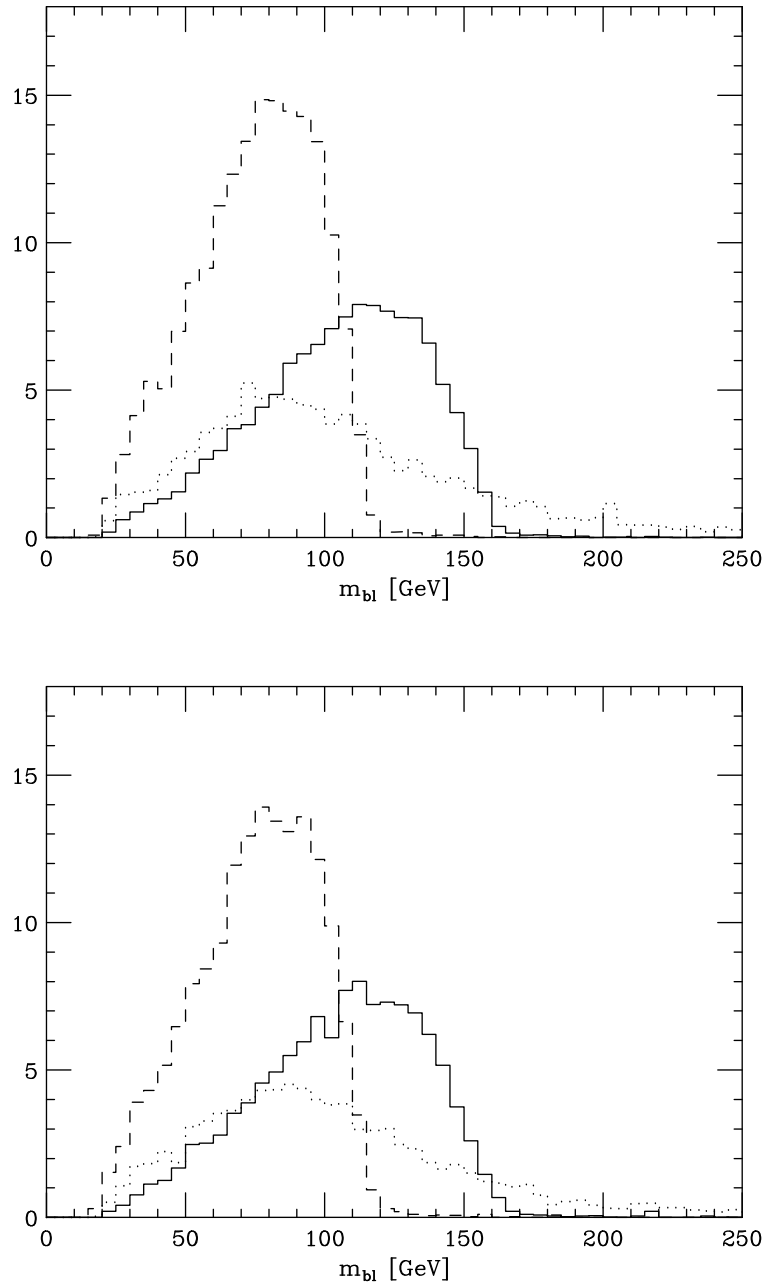
Figure 8.7: $m_{b\ell}$ distributions without (top) or with (bottom) smearing, after all the above analysis for the Tevatron.
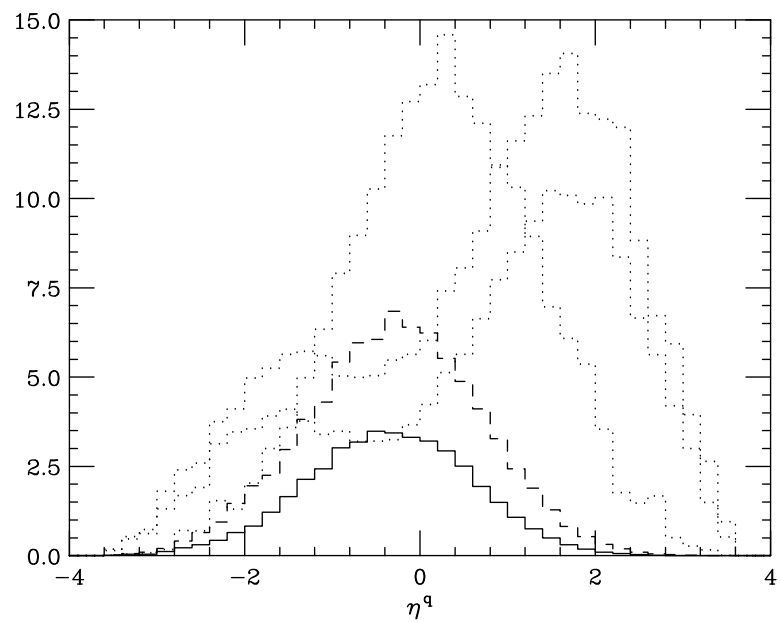
Figure 8.8: The rapidity distribution, after Equation (8.3), of the spectator jet (*i.e.*, $\bar{b}$-jet if b-jet identified) in the W^* event for m_t=180 GeV (solid) and 140 GeV (dash) against Figure 8.2 (dots), at the Tevatron.

of the spectator jet (labeled as q-jet) is asymmetric and less likely to be around zero. Third, the polarization of the top quark produced from the W^* process is not purely left-hand polarized as in the case of the $q'b \to qt$ process. For a 180 (140) GeV top quark, the ratio of the event rates for producing a left-handed top versus a right-handed top in the W^* event is about 3.5(3.4). In Figure 8.9, we show the production rate for a left-handed or a right-handed top quark from the W^* process and compare them with that from the W–gluon fusion process as a function of m_t. Because the top quark is not 100% polarized in the W^* process, the angular correlation of ℓ and the spectator jet will not be as strong as that in the W–gluon fusion process. In Figure 8.10 we show the distribution of $\cos\theta_{\ell q}$ in W^* events for a 140 and 180 GeV top quark. (Here, q-jet denotes the spectator jet.) Following through the previous analysis done for the W–gluon fusion events we found that W^* production compliments the W–gluon fusion process by increasing the single-top production rate by about 10%.[2] Therefore, its contribution to our final results of various distributions is small.

In conclusion we found that at the Tevatron ($\bar{p}p$, $\sqrt{S} = 2$ TeV) the single-top production rate from the W–gluon fusion process after including the branching ratio for $t \to bW^+(\to \ell^+\nu)$ is about 0.22(0.44) pb for a 180 (140) GeV top quark, where $\ell^+ = e^+$ or μ^+. The kinematic acceptance after the kinematic cuts (8.3) and (8.4) is about 55%(40%). Assuming a 30% b-tagging efficiency we concluded that the single-top event rate from the W–gluon fusion process is about 0.036(0.052) pb. For an integrated luminosity of 1 fb^{-1}, this yields 36(52) reconstructed single-top events. (To include top-antiquark production, a factor 2 should be included.) The dominant background process is the electroweak-QCD process $W + b\bar{b}$ whose rate is about 80%(60%) of the signal rate in the end of the analysis. The $t\bar{t}$ events are not as important to our study. The $t\bar{t}$ rate for a 180 GeV top quark is only 0.4% and 4% of the signal rate for its lepton+jet and di-lepton mode, respectively. In both Figs. 8.5 and 8.6 for the distribution of m_t, we have also included another single-top production process (a single-top produced from W^*) which increases the single-top rate by about 10%.

Let us make a side remark about the dominant background $q'\bar{q} \to W + b\bar{b}$ before we close this section. In the above analysis we did not include the possibility of having an additional QCD jet from either the radiation or the conversion of the incoming quark jet (q' or $\bar{q}$). The concern is that this jet may be identified as a forward jet which would fake the single-top signal event. In this case, b and $\bar{b}$ in the $W + b\bar{b} + jet$ background event have to both fall into a cone of $\Delta R = 0.7$ in order to fake the tagged b-jet (only one b) in the single-t event (cf. Equation (8.1)). To examine the possibility for this to happen, we have applied the eikonal approximation [60] to calculate the rate of $W + b\bar{b} + jet$ from the square of the $W + b\bar{b}$ amplitude. (The results are shown in Appendix E.)

After the basic kinematic cuts:

$$P_T^{jet} > 15\text{GeV}, \quad |\eta^{jet}| < 3.5,$$

$$P_T^{\ell} > 15\text{GeV}, \quad |\eta^{\ell}| < 2,$$

$$P_T^{b,\bar{b}} > 15\text{GeV}, \quad |\eta^{b,\bar{b}}| < 3.5, \tag{8.11}$$

---

[2] The W^* production rate is about one fifth of the W–gluon fusion rate for a 180 GeV top quark, and the kinematic acceptance of the W^* event is about half of that of the W–gluon fusion event.

the rate for $W + b\bar{b} + jet$ is already about a factor of 5 smaller than that for $W + b\bar{b}$. Naively, one might expect a factor of $\alpha_s(M_W)$ (~ 0.1) suppression factor for emitting an additional QCD jet (quark or gluon) in the hard scattering process. However, as compared to the large invariant mass ($M_{Wb\bar{b}}$) of the $W + b\bar{b}$ system a jet P_T of 15 GeV may be small enough to generate large logs, such as $\ln(M_{Wb\bar{b}}/P_T)$, in the amplitudes. Hence, because $\alpha_s \ln(M_{Wb\bar{b}}/P_T)$ is not negligible, the rate for $W + b\bar{b} + jet$ is not suppressed by a factor of 10 relative to the rate of $W + b\bar{b}$, but only a factor of 5.

To see how often b and $\bar{b}$ will fall into a cone of $\Delta R = 0.7$ we show in Figs. 8.11 and 8.12 the $\Delta R_{b\bar{b}}$ and the $M_{b\bar{b}}$ distributions in $W + b\bar{b} + jet$ events after applying the kinematic cuts listed in (8.11). The same distribution in $W + b\bar{b}$ events is also shown for comparison. The $\Delta R_{b\bar{b}}$ distributions look alike, and the $M_{b\bar{b}}$ distribution falls slowly as $M_{b\bar{b}}$ increases. Also, the $W + b\bar{b} + jet$ event prefers a larger $M_{b\bar{b}}$ because the P_T of b and $\bar{b}$ are larger in this process than that in the $W + b\bar{b}$ process. We find that only about 20% of the $W + b\bar{b} + jet$ events can possibly fake the single-t event by having b and $\bar{b}$ inside the same jet-cone and thus fake a tagged b-jet. Hence, the additional background rate from $W + b\bar{b} + jet$ events is about a factor of $\frac{1}{5} \times 20\% = 4\%$ of the electroweak-QCD background rate. Although our estimate is not precise, we believe our conclusion for this additional background should hold within a factor of 2. Hence, this additional background is negligible at the Tevatron. However, it can be important at the LHC. Because the energy of the LHC collider is much higher, it is more likely to have additional radiation in the event and to boost the $b\bar{b}$ system to make them closer and thus fall into the same jet-cone.

8.2   Tevatron with $\sqrt{S} = 4\,\text{TeV}$

Here we present our results for a possible upgrade of the Tevatron with $\sqrt{S} = 4\,\text{TeV}$. After the following kinematic cuts:

$$P_T^q > 15\,\text{GeV}, \quad |\eta^q| < 3.5,$$

$$P_T^\ell > 15\,\text{GeV}, \quad |\eta^\ell| < 2,$$

$$P_T^b > 30\,\text{GeV}, \quad |\eta^b| < 2,$$

$$\not{E}_T > 15\,\text{GeV}, \quad \Delta R_{qb} > 0.7\,, \tag{8.12}$$

the signal rate is about 0.28(0.37) pb. (The efficiency of these cuts is 45%(56%).) In Figure 8.13 the typical rapidity of the spectator jet in the signal event is about 2, and almost all the signal events have $|\eta^q| < 3.5$. An asymmetric cut on P_T was used once again to suppress the major background process $W + b + jet$. Demanding $P_T^b > 15\,\text{GeV}$ along with the other cuts in Equation (8.12), the signal-to-background ratio (S/B) is about 1.1(1.7). We show in Figure 8.14 the P_T distribution of the tagged b from t. Requiring $P_T^b > 30\,\text{GeV}$ excludes about half of the background events sacrificing about 6%(20%) of the signal. After all the cuts listed in Equation (8.12), S/B $\simeq$ 2.3(3.0) with the signal rate at 0.28(0.37) pb.

We show in Figure 8.15 the distribution of $\cos\theta_{\ell q}$. After applying the cut (8.4), the ratio S/B $\simeq$ 2.9(3.8) with the signal rate of 0.22(0.29) pb. In the end of the analysis there are about 2200(2900) single-t events for an integrated luminosity of 10

fb^{-1} at $\sqrt{S} = 4$ TeV (a $\bar{\text{p}}$p collider) with a significance S/$\sqrt{\text{B}}$ of about 80(105). The kinematic acceptance of the signal event is about 43%(34%). Note that in all the above rates we have included the reduction factor from a 30% b-tagging efficiency. In Figure 8.16, we show the reconstructed invariant mass (m_t) of the top quark. Once again, to incorporate the effects of detector efficiencies, we smear the final state parton momenta as in (8.9). The m_t distribution becomes slightly broader as shown in Figure 8.17; however, both the signal and the background rates are almost the same as those obtained with a perfect detector.

8.3 LHC with $\sqrt{S} = 14\,\textbf{TeV}$

Here we present our results for the LHC with $\sqrt{S} = 14$ TeV. After the following kinematic cuts

$$P_T^q > 40\,\text{GeV}, \quad 1 < |\eta^q| < 4,$$

$$P_T^\ell > 40\,\text{GeV}, \qquad |\eta^\ell| < 2,$$

$$P_T^b > 40\,\text{GeV}, \qquad |\eta^b| < 2,$$

$$\not{E}_T > 40\,\text{GeV}, \quad \Delta R_{qb} > 0.7\ , \tag{8.13}$$

the signal rate is about 0.44(0.24) pb. (The efficiency of the cuts is 94%(98%). We still assume a 30% efficiency for the b-tagging at the LHC.) Here we did not impose a smaller P_T^q cut because a lower P_T jet will be more difficult to be identified at the LHC. (A typical QCD event at the supercollider will be engulfed by soft gluon radiation.) Since the signal event yield is large at the LHC, we decided to purify our data simply by requiring a large P_T^q cut. Notice that the rate for $m_t = 180$ GeV is larger at the LHC than that for $m_t = 140$ GeV after our cuts, opposite to the behavior of the rate at 2 TeV and 4 TeV. This is due in part to less sensitivity to m_t at higher energies, but mainly because the b from top decay is much harder for larger top mass and thus is less sensitive to the cut of $P_T^b > 40$ GeV. The typical P_T^b for m_t = 180 (140) GeV is 60(40) GeV. We show in Figure (8.18) the P_T distribution of the tagged b from t.

In Figure 8.19 the typical rapidity of the spectator jet in the signal event is about 3, but a cut on $|\eta^q| < 4$ keeps almost all the signal events. Excluding the $|\eta^q| > 1$ cut in (8.13) the signal-to-background ratio (S/B) is about 10(7). Requiring $|\eta^q| > 1$ excludes about 40% of the background events sacrificing about 15%(20%) of the signal. After the kinematic cuts in (8.13), the ratio S/B $\simeq 25(14)$.

We show in Figure 8.20 the distribution of $\cos\theta_{\ell q}$ at the LHC. After the $\cos\theta_{\ell q}$ cut, S/B $\simeq 40(20)$. In the end of the analysis, there are about $30,000(15,000)$ single-top events for an integrated luminosity of 100 fb^{-1} at $\sqrt{S} = 14$ TeV (a pp collider) with a significance S/$\sqrt{\text{B}}$ of about 32(16). Hence, about 4%(2%) of the total signal event rate remains. This is thus the kinematic acceptance for the signal process (8.1). In Figure 8.21, we show the reconstructed invariant mass (m_t) of the top quark for a perfect detector. Once again, to incorporate the effects of detector efficiencies, we smear the final state parton momenta as in (8.9) and reconstruct the m_t distribution

for the LHC is shown in Figure 8.22.

Notice that the above analysis for the LHC is less reliable because the energy of the collider is much higher and therefore it is more likely to have additional soft-jets accompanying the signal and the background events. As discussed at the end of section 7.1, it would be more reliable to use a full event generator such as ISAJET [61], PYTHIA [62] or HERWIG [63] for this study because these generators contain radiation from either the initial or final states. However, these generators currently do not have the correct angular correlations in ℓ and jets, as discussed in this analysis. It would therefore be important in the future to improve these generators to incorporate the polarization effects of the top quark and the W–boson for studying physics of the top quark in hadron collisions.
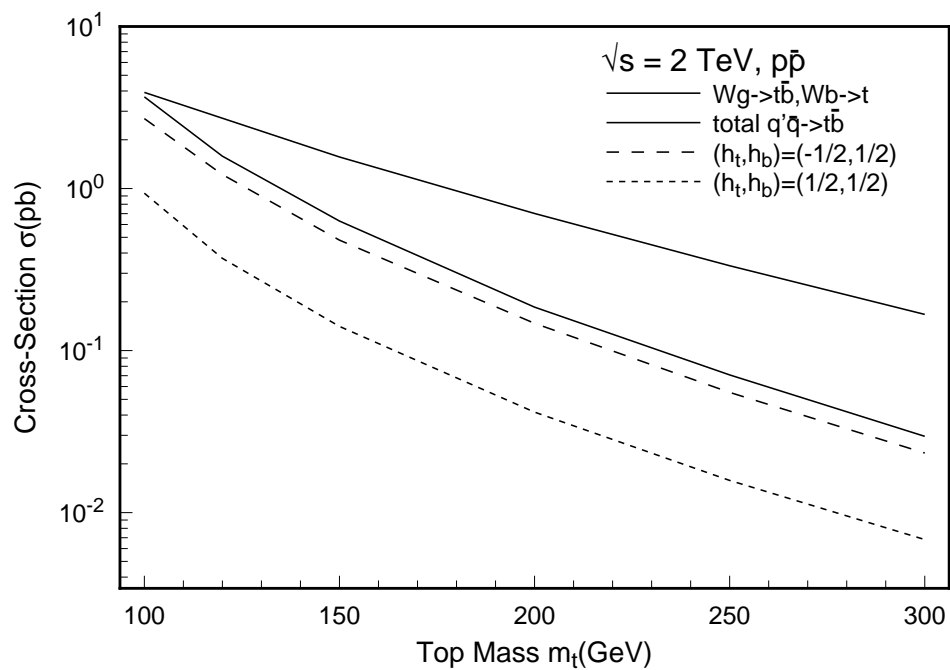
Figure 8.9: The production rate for a left-handed (long dash) or a right-handed (short dash) top quark from the W^* process. The upper solid line is the total rate for the W–gluon fusion process, the lower solid line for the W^* process.
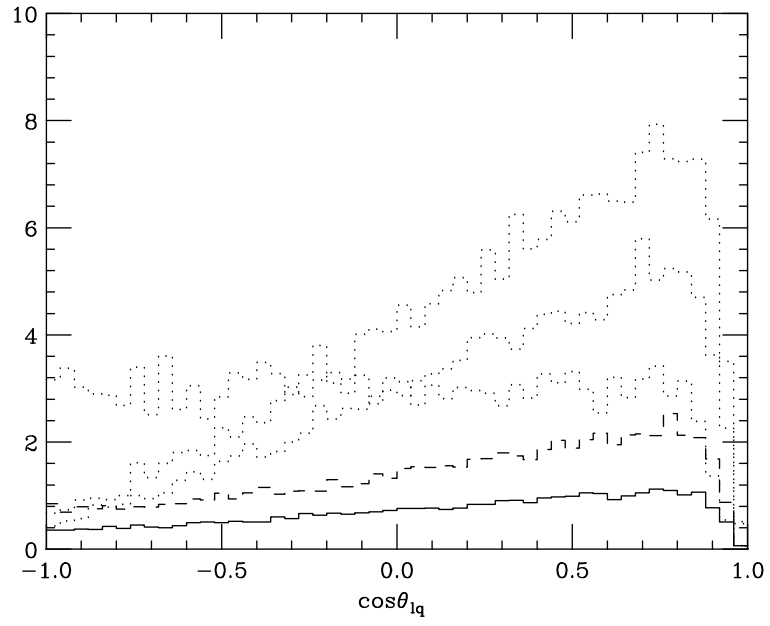
Figure 8.10: The distribution of $\cos\theta_{\ell q}$ in W^* event for m_t=180 GeV (solid) and 140 GeV (dash) against Figure 8.4 (dots), at the Tevatron.
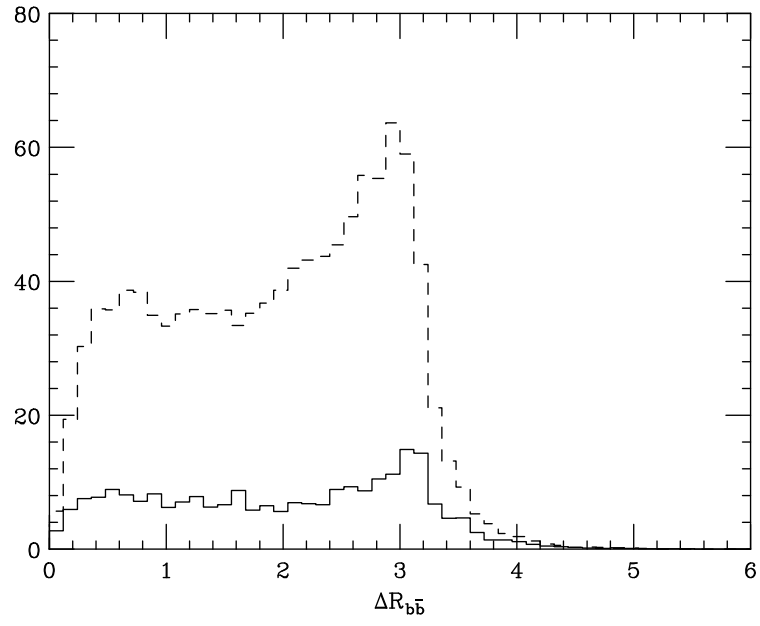
Figure 8.11: $\Delta R_{b\bar{b}}$ distributions in $W + b\bar{b} + jet$ (solid) and $W + b\bar{b}$ (dash) events after applying the cuts listed in (8.11).
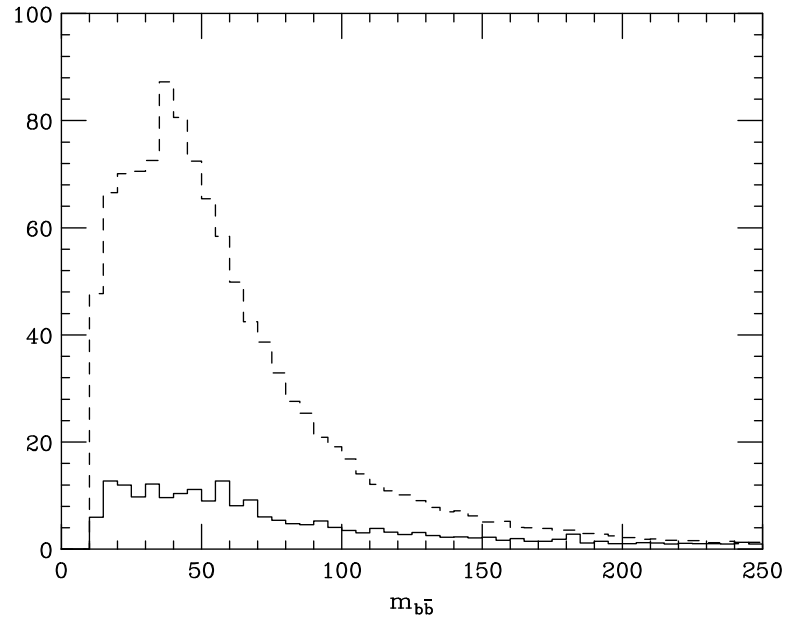
Figure 8.12: $M_{b\bar{b}}$ distributions in $W + b\bar{b} + jet$ (solid) and $W + b\bar{b}$ (dash) events after applying the cuts listed in (8.11).
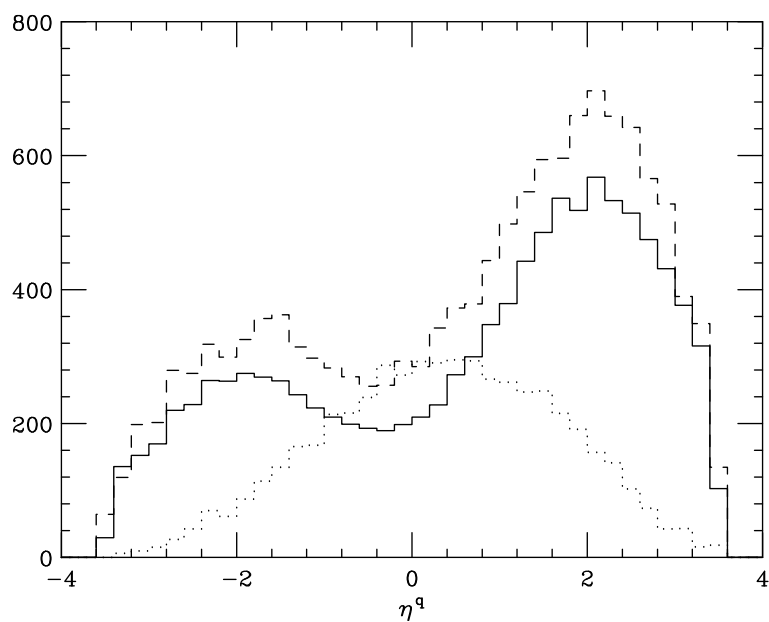
Figure 8.13: The rapidity distribution of the spectator quark q, after cuts in Equation (8.12), for the signal $q'b \to qt(\to bW^+(\to \ell^+\nu))$, and of the spectator quark $\bar{b}$ for the major background $q'\bar{q} \to \bar{b}bW^+(\to \ell^+\nu)$ (dots), for $m_t = 180\,\text{GeV}$ (solid) and $140\,\text{GeV}$ (dash), at the Di-TeV.
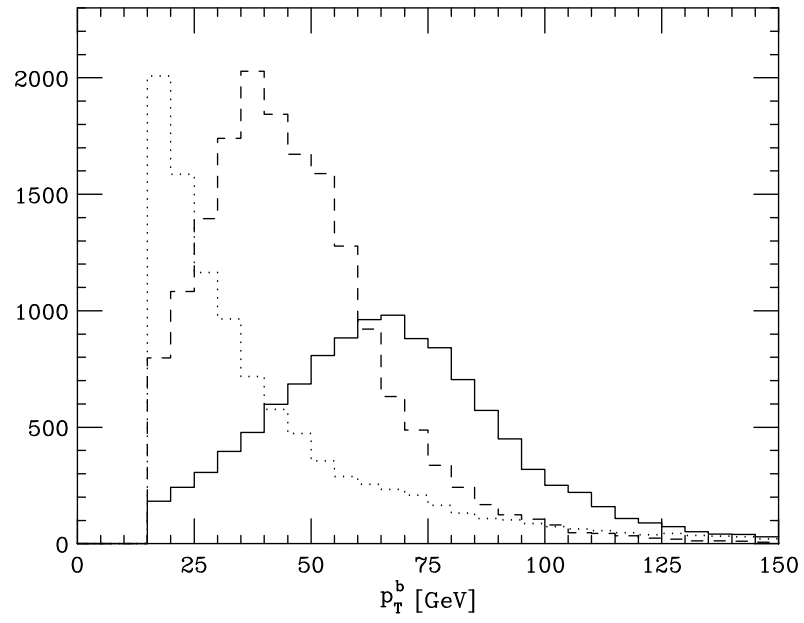
Figure 8.14: P_T distribution of the b quark, after requiring $P_T^b > 15\,\mathrm{GeV}$ along with all the other cuts in (8.12), for the signal $q'b \to qt(\to bW^+(\to \ell^+\nu))$, and the major background $q'\bar{q} \to \bar{b}bW^+(\to \ell^+\nu)$, at the Di-TeV.
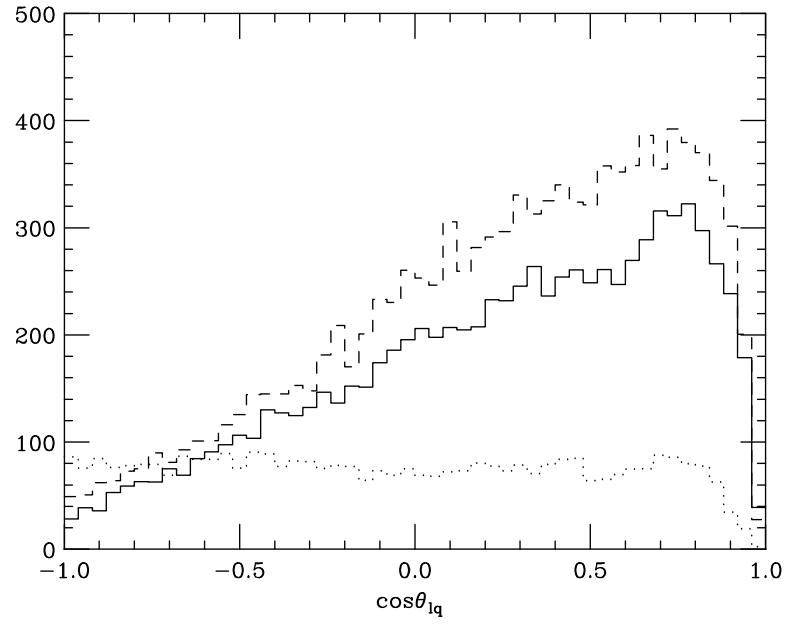
Figure 8.15: $\cos\theta_{\ell q}$ distribution for the signal $q'b \rightarrow qt(\rightarrow bW^+(\rightarrow \ell^+\nu))$ and background $q'\bar{q} \rightarrow \bar{b}bW^+(\rightarrow \ell^+\nu)$ at the Di-TeV.
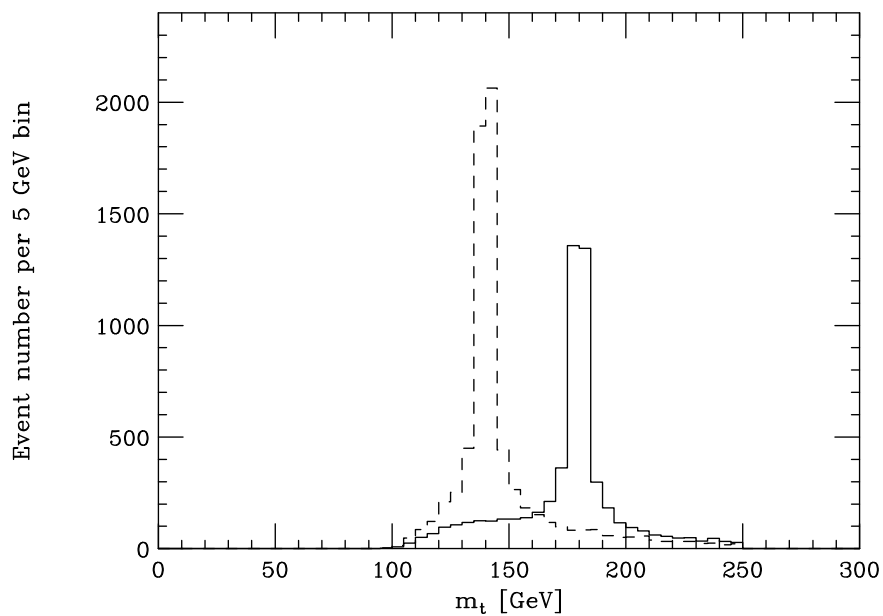
Figure 8.16: The m_t distribution after the cuts Equation (8.12) and Equation (8.4) for $m_t = 180$ GeV (solid) and 140 GeV (dash) at the Di-TeV, including both the signal and background events with $W^{\pm} \to e^{\pm}$ or $\mu^{\pm}$.
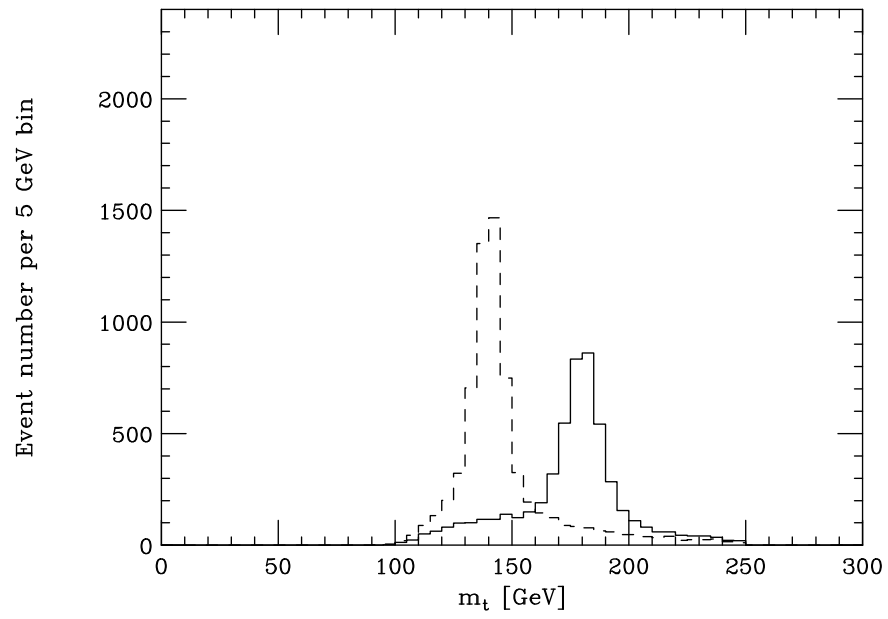
Figure 8.17:   Same as Figure 8.16 but with detector resolution effects as described in Equation (8.9).
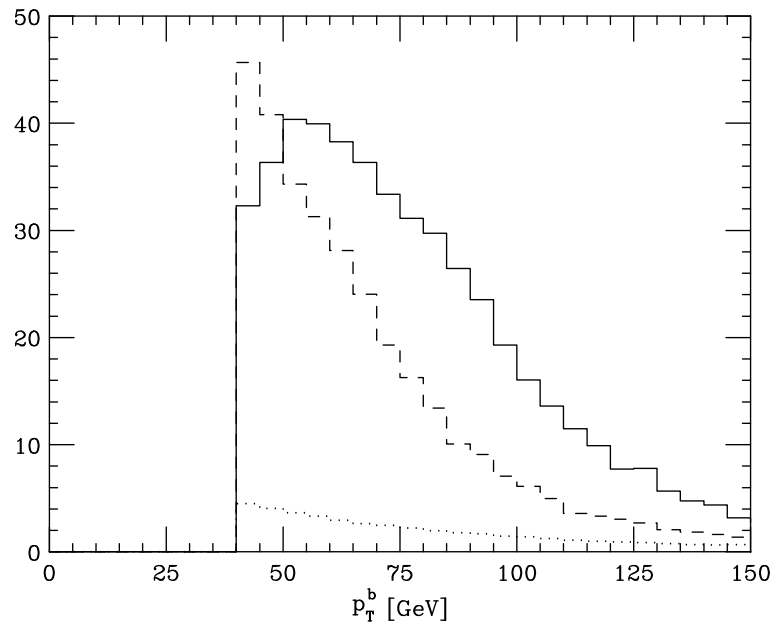
Figure 8.18: P_T distribution of the b quark, after cuts in (8.13), for the signal $q'b \to qt(\to bW^+(\to \ell^+\nu))$, and the major background $q'\bar{q} \to \bar{b}bW^+(\to \ell^+\nu)$, at the LHC.
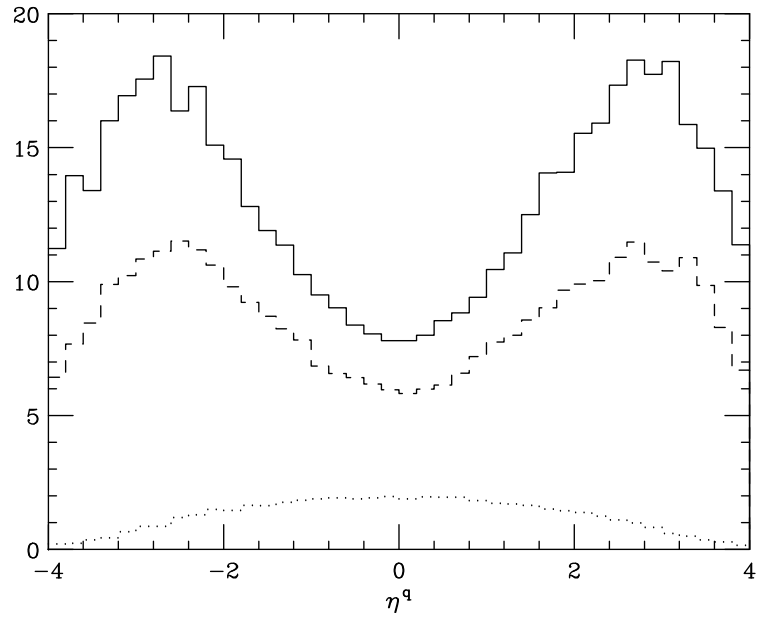
Figure 8.19:   The rapidity distribution of the spectator quark q, after cuts in Equation (8.13), for the signal $q'b \rightarrow qt(\rightarrow bW^+(\rightarrow \ell^+\nu))$, and of the spectator quark $\bar{b}$ for the major background $q'\bar{q} \rightarrow \bar{b}bW^+(\rightarrow \ell^+\nu)$ (dots), for $m_t = 180\,\text{GeV}$ (solid) and $140\,\text{GeV}$ (dash), at the LHC.
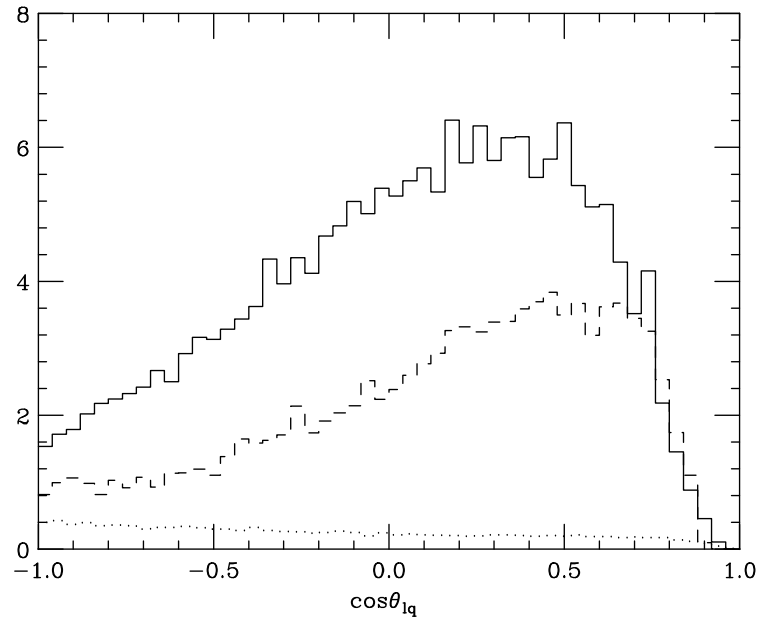
Figure 8.20: $\cos\theta_{\ell q}$ distribution for the signal $q'b \rightarrow qt(\rightarrow bW^+(\rightarrow \ell^+\nu))$ and background $q'q \rightarrow \bar{b}bW^+(\rightarrow \ell^+\nu)$ at the LHC.
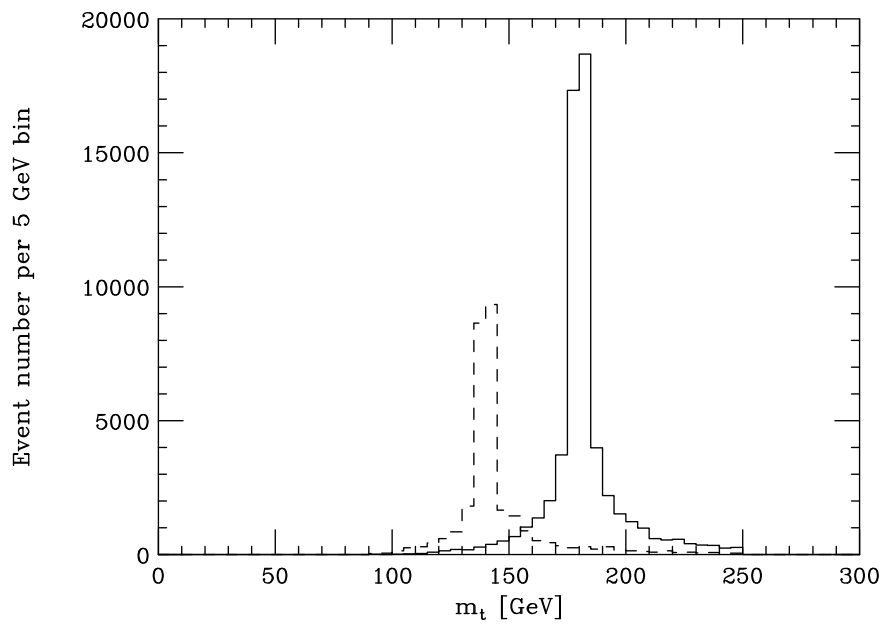
Figure 8.21: The m_t distribution after the cuts Equation (8.13) and Equation (8.4) for $m_t = 180\,\text{GeV}$ (solid) and $140\,\text{GeV}$ (dash) at the LHC including both the signal and background events with $W^\pm \to e^\pm$ or $\mu^\pm$.
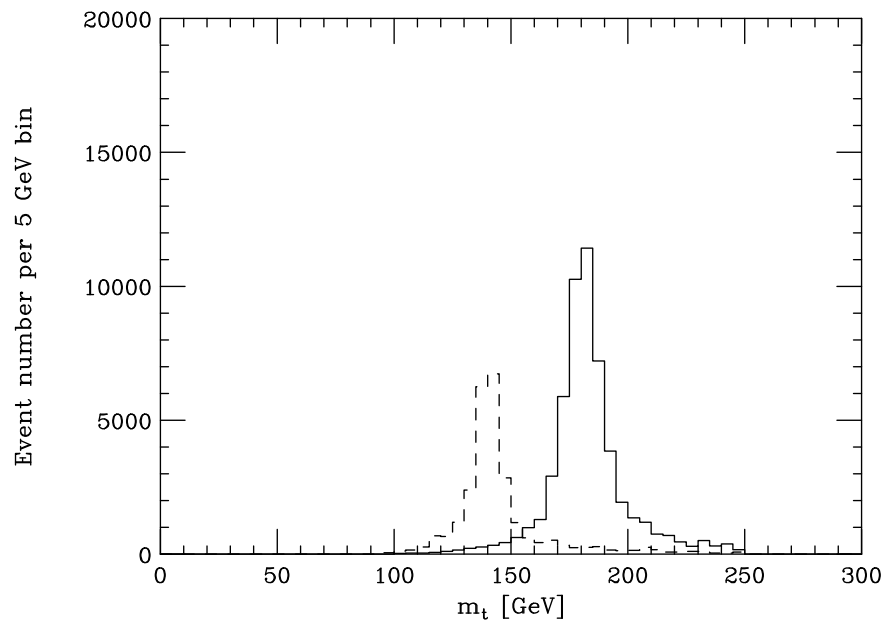
Figure 8.22: Same as Figure 8.21, but with detector resolution effects as described in Equation (8.9).

Chapter 9

Discussions and Conclusions

We discussed the physics of top quark production and decay at hadron colliders, such as the Tevatron, the Di-TeV and the LHC. We showed how to use the invariant mass distribution of $m_{b\ell}$ to measure the mass and the width of the top quark, produced from either a single-top or a $t\bar{t}$ pair process. It has been shown in Reference [41] that the distribution of $m_{b\ell}$ is not sensitive to radiative corrections from QCD interactions. Thus it can be reliably used to test the polarization of the W–boson from t decay (hence, test the polarization of the top quark from the production mechanism) and to measure the mass of the top quark using the observed value of f_{Long} (the fraction of longitudinal W's from top decays). We also discussed how well the couplings of t-b-W vertex can be measured to probe new physics, and how well the CP properties of the top quark can be tested in electron or hadron colliders.

In Reference [24] we showed that an almost perfect efficiency for "kinematic b tagging" can be achieved due to the characteristic features of W–gluon fusion events. In addition, the ability of performing b-tagging using a vertex detector increases the detection efficiency of a heavy top quark produced via the W–gluon fusion process.

A detailed Monte Carlo study on how to identify the characteristic features of the signal events (*i.e.*, the transverse momentum and the rapidity distributions of the spectator quark which emitted the virtual W) and therefore suppress the background events was performed in Chapter 8.[1] For an integrated luminosity of 1 fb^{-1}, there will be about 75 (105) single-t or single-$\bar{t}$ events reconstructed in the lepton+jet mode for $m_t = 180\,(140)\,\text{GeV}$ at $\sqrt{S} = 2\,\text{TeV}$. (The branching ratio of $W \to e$, or μ is included, and the b-quark tagging efficiency is assumed to be 30% for $P_t^b > 30\,\text{GeV}$ with no misidentifications of a b-jet from other QCD jets.) The dominant background process is the electroweak-QCD process $W + b\bar{b}$ whose rate is about 80%(60%) of the signal rate in the end of the analysis. The $t\bar{t}$ events are not as important to our study. The results for $\sqrt{S} = 4\,\text{TeV}$ at the Di-TeV and for $\sqrt{S} = 14\,\text{TeV}$ at the LHC were also discussed.

Although the $W^* \to t\bar{b}$ rate in the SM is not as large as the W–gluon fusion rate for producing a heavy top quark, it remains a complementary process for probing

---

[1] The fortran code, ONETOP, used for this study is available by request. In Appendix F we briefly describe the processes included in this program.

new physics in the single-top quark event. The W^* process is particularly useful for detecting new physics through some possible high mass resonance in the theory. In that case, its rate will be highly enhanced by the resonance effects. We however did not study such a possibility in this work because its rate depends on the details of the models considered.

Appendix A

Helicity Amplitude Method

In this appendix we would like to display the rules for doing calculations at the amplitude level using the Helicity Amplitude Method. The method breaks down the algebra of four-dimensional Dirac spinors and matrices into equivalent two-dimensional ones. This algebra is easy to program and more efficient than computing the Dirac algebra as it stands. All diagrams are summed and squared numerically.

In what follows we introduce the Weyl representation of Dirac spinors and matrices. We also include several example calculations to illustrate the finer points of the method. Throughout this paper we use the Bjorken-Drell metric

$$g^{\mu\nu} = diag\,(1, -1, -1, -1)\,. \tag{A.1}$$

The four-momenta have the form in spherical coordinates:

$$p^\mu = (E, |\vec{p}|\sin\theta\cos\phi, |\vec{p}|\sin\theta\sin\phi, |\vec{p}|\cos\theta) \tag{A.2}$$

with $E^2 - |\vec{p}|^2 = m^2$. We define the right-hand (R), left-hand (L) and longitudinal (0) polarization vectors for a spin-1 field as [1]

$$
\begin{aligned}
\varepsilon^\mu_{(R)} &= \frac{e^{i\phi}}{\sqrt{2}}(0, i\sin\phi - \cos\phi\cos\theta, -i\cos\phi - \sin\phi\cos\theta, \sin\theta) \\[2mm]
\varepsilon^\mu_{(L)} &= \frac{e^{-i\phi}}{\sqrt{2}}(0, i\sin\phi + \cos\phi\cos\theta, -i\cos\phi + \sin\phi\cos\theta, -\sin\theta) \qquad \text{(A.3)} \\[2mm]
\varepsilon^\mu_{(0)} &= \frac{1}{m}(|\vec{p}|, E\sin\theta\cos\phi, E\sin\theta\sin\phi, E\cos\theta).
\end{aligned}
$$

The above equations satisfy the identities $\varepsilon^\mu_{(R)} = -\varepsilon^{\mu*}_{(L)}$, $\varepsilon^\mu_{(0)} = \varepsilon^{\mu*}_{(0)}$, $p_\mu\varepsilon^\mu_{(h)} = 0$ and $\varepsilon^{(h)}_\mu\varepsilon^{\mu*}_{(h')} = -\delta_{hh'}$, for $h, h' = R, L$ or 0.

---

[1] For a massless spin-1 field, only the right-handed and the left-handed polarizations are physical.

In four component form we define the following. In the Weyl basis Dirac spinors have the form

$$\psi = \begin{pmatrix} \psi_+ \\ \psi_- \end{pmatrix} \tag{A.4}$$

where for fermions

$$\psi_\pm = \begin{cases} u_\pm^{(\lambda=1)} = w_\pm \chi_{1/2} \\ u_\pm^{(\lambda=-1)} = w_\mp \chi_{-1/2} \end{cases} \tag{A.5}$$

and anti-fermions

$$\psi_\pm = \begin{cases} v_\pm^{(\lambda=1)} = \pm w_\mp \chi_{-1/2} \\ v_\pm^{(\lambda=-1)} = \mp w_\pm \chi_{1/2} \end{cases} \tag{A.6}$$

with $w_\pm = \sqrt{E \pm |\vec{p}|}$.

The $\chi_{\lambda/2}$'s are eigenvectors of the helicity operator

$$h = \hat{p} \cdot \vec{\sigma}, \; \hat{p} = \vec{p}/|\vec{p}| \tag{A.7}$$

with eigenvalue λ where $\lambda = +1$ is for "spin-up" and $\lambda = -1$ is for "spin-down".

$$\chi_{1/2} = \begin{pmatrix} \cos\theta/2 \\ e^{i\phi}\sin\theta/2 \end{pmatrix}, \quad \chi_{-1/2} = \begin{pmatrix} -e^{-i\phi}\sin\theta/2 \\ \cos\theta/2 \end{pmatrix}. \tag{A.8}$$

Later it proves useful to represent $\chi_{\lambda/2}$'s using bra-ket notation where

$$|\hat{p}+\rangle \equiv \chi_{1/2}, \quad |\hat{p}-\rangle \equiv \chi_{-1/2}. \tag{A.9}$$

Gamma matrices in the Weyl basis have the form

$$\gamma^0 = \begin{pmatrix} 0 & 1 \\ 1 & 0 \end{pmatrix}, \quad \gamma^j = \begin{pmatrix} 0 & -\sigma_j \\ \sigma_j & 0 \end{pmatrix}, \quad \gamma^5 = \gamma_5 = \begin{pmatrix} 1 & 0 \\ 0 & -1 \end{pmatrix}, \tag{A.10}$$

where σ_j are the Pauli 2×2 spin matrices

$$\sigma_1 = \begin{pmatrix} 0 & 1 \\ 1 & 0 \end{pmatrix}, \quad \sigma_2 = \begin{pmatrix} 0 & -i \\ i & 0 \end{pmatrix}, \quad \sigma_3 = \begin{pmatrix} 1 & 0 \\ 0 & -1 \end{pmatrix}. \tag{A.11}$$

The chirality projection operators are defined by

$$P_\pm = \frac{1}{2}(1\pm\gamma^5). \tag{A.12}$$

Notice that P_+ (P_-) projects out the "right-handed" ("left-handed") component of the Weyl spinor effectively reducing the algebra from one involving four component spinors and matrices to one involving two component spinors and matrices.
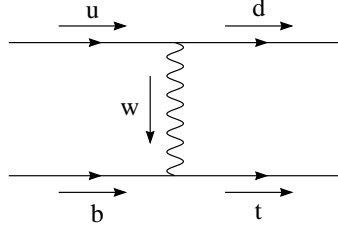
Figure A.1: Diagram for the $(2 \to 2)$ process $ub \to dt$.

$$P_- \psi = \begin{pmatrix} 0 & 0 \\ 0 & 1 \end{pmatrix} \begin{pmatrix} \psi_+ \\ \psi_- \end{pmatrix} = \begin{pmatrix} 0 \\ \psi_- \end{pmatrix}$$

$$\bar\psi P_+ = (\psi_+^\dagger \ \psi_-^\dagger) \begin{pmatrix} 0 & 1 \\ 1 & 0 \end{pmatrix} \begin{pmatrix} 1 & 0 \\ 0 & 0 \end{pmatrix} = (\psi_-^\dagger \ 0) \tag{A.13}$$

In the Weyl basis $\not{p}$ has the form

$$\not{p} \equiv p_\mu \gamma^\mu = \begin{pmatrix} 0 & p_0 + \vec\sigma \cdot \vec p \\ p_0 - \vec\sigma \cdot \vec p & 0 \end{pmatrix} \equiv \begin{pmatrix} 0 & \not{p}_+ \\ \not{p}_- & 0 \end{pmatrix} \equiv p_\mu \begin{pmatrix} 0 & \gamma_+^\mu \\ \gamma_-^\mu & 0 \end{pmatrix} \tag{A.14}$$

where

$$\gamma_\pm^\mu = (1, \mp\vec\sigma) . \tag{A.15}$$

Products of these $\gamma_\pm^\mu$'s have the following useful property when Lorentz indices are contracted:

$$(\gamma_+^\mu)_{ij}(\gamma_{\mu+})_{kl} = (\gamma_-^\mu)_{ij}(\gamma_{\mu-})_{kl} = 2[\delta_{ij}\delta_{kl} - \delta_{il}\delta_{kj}] \tag{A.16}$$

and

$$(\gamma_+^\mu)_{ij}(\gamma_{\mu-})_{kl} = (\gamma_-^\mu)_{ij}(\gamma_{\mu+})_{kl} = 2\delta_{il}\delta_{kj}, \tag{A.17}$$

where the Roman indices are not vector indices in the usual sense, but are labels identifying bras and kets. For instance, for arbitrary kets $|i\rangle, |j\rangle, |k\rangle$ and $|l\rangle$ we have

$$(\gamma_+^\mu)_{ij}(\gamma_{\mu-})_{kl} = \langle i|\gamma_+^\mu|j\rangle\langle k|\gamma_{\mu-}|l\rangle = 2 \langle i|\, l\rangle\langle k|\, j\rangle = 2\delta_{il}\delta_{kj} . \tag{A.18}$$

Equations (A.16) and (A.17) are simply the two-dimensional version of the well known Fiertz identities.

A.1   Helicity Amplitudes for $ub \to dt$

To illustrate the use of helicity amplitudes we calculate the matrix element for the $(2 \to 2)$ process $ub \to dt$ which contributes to the total rate for W–gluon fusion.

Figure A.1 shows the Feynman diagram for this process with the t decay included. In this example we use the generalized t-b-W coupling

$$\Gamma^\mu = \left(1 + \kappa_L{}^{CC}\right)\gamma^\mu P_- + \kappa_R{}^{CC}\gamma^\mu P_+ \tag{A.19}$$

where $\kappa_L{}^{CC}$ and $\kappa_R{}^{CC}$ parameterize deviations from the Standard Model in which $\kappa_L{}^{CC} = 0$ and $\kappa_R{}^{CC} = 0$. We calculate the matrix element in the 't Hooft-Feynman gauge ignoring for simplicity the factors due to vertices and propagators. We obtain

$$\mathcal{M} = [\bar{u}(t)\Gamma^\mu u(b)][\bar{u}(d)\gamma_\mu P_- u(u)] \tag{A.20}$$

where u, b, d and t are the momenta of the external legs and we retain only the mass of the top quark. We use the algebraic properties of the projection operators $P_\pm^2 = P_\pm, P_\pm P_\mp = 0$ and $P_\pm \gamma^\mu = \gamma^\mu P_\mp$ to project out the chirality states. In this example the amplitude contains both the left-handed and right-handed currents. For pure vector or axial vector currents one must first insert $1 = P_+ + P_-$ or $\gamma_5 = P_+ - P_-$ respectively. Therefore $\mathcal{M}$ takes the form

$$\mathcal{M} = (1 + \kappa_L{}^{CC})[u_-^\dagger(t)\gamma_+^\mu u_-(b)][u_-^\dagger(d)\gamma_{\mu+} u_-(u)]$$

$$+ \kappa_R{}^{CC}[u_+^\dagger(t)\gamma_-^\mu u_+(b)][u_-^\dagger(d)\gamma_{\mu+} u_-(u)] \tag{A.21}$$

According to Equations (A.5) and (A.9) we see that

$$u_-(u) = \sqrt{2E_u}\,|\,\hat{u}-\rangle$$

$$u_-(d) = \sqrt{2E_d}\,|\,\hat{d}-\rangle$$

$$u_-(b) = \sqrt{2E_b}\,|\,\hat{b}-\rangle$$

$$u_+(b) = \sqrt{2E_b}\,|\,\hat{b}+\rangle$$

$$u_-(t) = \begin{cases} \sqrt{E_t - |\vec{t}|}\,|\,\hat{t}+\rangle \\ \sqrt{E_t + |\vec{t}|}\,|\,\hat{t}-\rangle \end{cases}$$

$$u_+(t) = \begin{cases} \sqrt{E_t + |\vec{t}|}\,|\,\hat{t}+\rangle \\ \sqrt{E_t - |\vec{t}|}\,|\,\hat{t}-\rangle \end{cases} \tag{A.22}$$

Therefore,

$$\mathcal{M}(+) = (1 + \kappa_L{}^{CC})\sqrt{E_t - |\vec{t}|}\,\langle\,\hat{t}+|\gamma_+^\mu|\,\hat{b}-\rangle\langle\,\hat{d}-|\gamma_{\mu+}|\,\hat{u}-\rangle$$

$$+ \kappa_R{}^{CC}\sqrt{E_t + |\vec{t}|}\,\langle\,\hat{t}+|\gamma_-^\mu|\,\hat{b}+\rangle\langle\,\hat{d}-|\gamma_{\mu+}|\,\hat{u}-\rangle$$

$$\mathcal{M}(-) = (1 + \kappa_L{}^{CC})\sqrt{E_t + |\vec{t}|}\,\langle\,\hat{t}-|\gamma_+^\mu|\,\hat{b}-\rangle\langle\,\hat{d}-|\gamma_{\mu+}|\,\hat{u}-\rangle$$

$$+ \kappa_R{}^{CC}\sqrt{E_t - |\vec{t}|}\,\langle\,\hat{t}-|\gamma_-^\mu|\,\hat{b}+\rangle\langle\,\hat{d}-|\gamma_{\mu+}|\,\hat{u}-\rangle \tag{A.23}$$

where $\mathcal{M}(\pm)$ denotes the amplitude with t helicity $\lambda_t = \pm 1$ and we ignore for now the common factor of $\sqrt{2E_u}\sqrt{2E_b}\sqrt{2E_d}$.

One is now tempted to move on ahead and contract the Lorentz indices as in Equation (A.16). However, contracting γ_μ's with the same chirality introduces extra terms into the matrix element. It would be more useful with processes containing many branchings from decay, such as in Supersymmetry, if there were a way to utilize Equation (A.17) instead. To this end, we digress a moment.

Consider some current of the form

$$\psi_{f\pm}^\dagger [\gamma_{\mu_1\mp}\cdots\gamma_{\mu_n\mp}]\psi_{i\pm} \tag{A.24}$$

where n is odd. We note in passing, recalling the properties of the projection operators, consecutive matrices of the same sign would give zero current. Since Equation (A.24) is just a number, it is identical to taking its transpose as

$$\psi_{i\pm}^\top [\gamma_{\mu_n\mp}^\top \cdots \gamma_{\mu_1\mp}^\top]\psi_{f\pm}^* . \tag{A.25}$$

We now utilize the following algebraic properties of the Pauli matrices and in particular σ_2:

$$\sigma_2\sigma_2 = 1, \quad \sigma_2^\top = -\sigma_2, \quad \sigma_2\gamma_{\mu\mp}^\top\sigma_2 = \gamma_{\mu\pm} \tag{A.26}$$

and define

$$\widetilde{\psi_\pm} \equiv i\sigma_2\psi_\pm^* . \tag{A.27}$$

By inserting pairs of σ_2 between each pair of objects in Equation (A.25) we therefore obtain

$$\psi_{f\pm}^\dagger [\gamma_{\mu_1\mp}\cdots\gamma_{\mu_n\mp}]\psi_{i\pm} = \widetilde{\psi_{i\pm}}^\dagger [\gamma_{\mu_n\pm}\cdots\gamma_{\mu_1\pm}]\widetilde{\psi_{f\pm}} . \tag{A.28}$$

It is easy to show that $(i\sigma_2\psi_{i\pm})^\top = \widetilde{\psi_{i\pm}}^\dagger$. In addition, for an even number n of gamma matrices we have

$$\psi_{f\pm}^\dagger [\gamma_{\mu_1\mp}\cdots\gamma_{\mu_n\pm}]\psi_{i\mp} = \widetilde{\psi_{i\mp}}^\dagger [\gamma_{\mu_n\mp}\cdots\gamma_{\mu_1\pm}]\widetilde{\psi_{f\pm}} . \tag{A.29}$$

An important result has occurred, which allows us to take advantage of Equation (A.17) avoiding the number of terms that would otherwise occur. [2] For a fermion or anti-fermion with momentum $\vec{p}$ and helicity λ, $\psi_\pm$ is proportional to either $|\hat{p}+\rangle$ or $|\hat{p}-\rangle$. It is easy to show that

$$\begin{aligned}
\widetilde{|\hat{p}+\rangle} &= -|\hat{p}-\rangle, \\
\widetilde{|\hat{p}-\rangle} &= +|\hat{p}+\rangle, \\
\widetilde{\langle\hat{p}+|} &= -\langle\hat{p}-|, \\
\widetilde{\langle\hat{p}-|} &= +\langle\hat{p}+| .
\end{aligned} \tag{A.30}$$

---

[2] $i\sigma_2$ acts as a kind of charge conjugation operator on the chirality states of the Weyl spinors.

Finally, recalling Equation (A.23) the term

$$\langle \hat{d} - |\gamma_{\mu +}| \hat{u} - \rangle = \langle \hat{u} + |\gamma_{\mu -}| \hat{d} + \rangle \qquad (A.31)$$

giving, via Equation (A.17),

$$\mathcal{M}(+) = 2(1 + \kappa_L{}^{CC})\sqrt{E_t - |\vec{t}|}\,\langle \hat{t} + |\hat{d} + \rangle\langle \hat{u} + |\hat{b} - \rangle$$

$$+ 2\kappa_R{}^{CC}\sqrt{E_t + |\vec{t}|}\,\langle \hat{t} + |\hat{u} - \rangle\langle \hat{d} - |\hat{b} + \rangle$$

$$\mathcal{M}(-) = 2(1 + \kappa_L{}^{CC})\sqrt{E_t + |\vec{t}|}\,\langle \hat{t} - |\hat{d} + \rangle\langle \hat{u} + |\hat{b} - \rangle$$

$$+ 2\kappa_R{}^{CC}\sqrt{E_t - |\vec{t}|}\,\langle \hat{t} - |\hat{u} - \rangle\langle \hat{d} - |\hat{b} + \rangle. \qquad (A.32)$$

We now have the matrix element in the form we require for our Monte Carlo package ONETOP[3], remembering to include coupling constants, propagators, color factors and $\sqrt{2E_u}\sqrt{2E_b}\sqrt{2E_d}$.

A.2   Helicity Amplitudes for $ub \to dt$ in the CMS.

To illustrate our claim that in the SM (*i.e.* $\kappa_L{}^{CC} = 0$ and $\kappa_R{}^{CC} = 0$) only the left-handed top quark is produced from the $ub \to dt$ process in the d-t center of mass frame (CMS), we evaluate the matrix element in terms of CMS variables. Define the four-momenta:

$$\begin{aligned} u^\mu &= (\sqrt{\hat{s}}/2, 0, 0, -\sqrt{\hat{s}}/2) \\ b^\mu &= (\sqrt{\hat{s}}/2, 0, 0, \sqrt{\hat{s}}/2) \\ d^\mu &= (t, -t\sin\theta, 0, -t\cos\theta) \\ t^\mu &= (E_t, t\sin\theta, 0, t\cos\theta) \end{aligned} \qquad (A.33)$$

where $E_t = (\hat{s} + m_t^2)/2\sqrt{\hat{s}}$, $t = (\hat{s} - m_t^2)/2\sqrt{\hat{s}}$ and we have chosen $\phi = 0$ to be the scattering plane.

Using these, we obtain from Equations (A.5), (A.8) and (A.9)

$$|\hat{u} +\rangle = \begin{pmatrix} 0 \\ -1 \end{pmatrix}$$

$$|\hat{u} -\rangle = \begin{pmatrix} 1 \\ 0 \end{pmatrix}$$

---

[3] A FORTRAN code.

$$|\hat{b}+\rangle = \begin{pmatrix} 1 \\ 0 \end{pmatrix}$$

$$|\hat{b}-\rangle = \begin{pmatrix} 0 \\ 1 \end{pmatrix}$$

$$|\hat{d}+\rangle = \begin{pmatrix} \sin\theta/2 \\ -\cos\theta/2 \end{pmatrix}$$

$$|\hat{d}-\rangle = \begin{pmatrix} \cos\theta/2 \\ \sin\theta/2 \end{pmatrix}$$

$$|\hat{t}+\rangle = \begin{pmatrix} \cos\theta/2 \\ \sin\theta/2 \end{pmatrix}$$

$$|\hat{t}-\rangle = \begin{pmatrix} -\sin\theta/2 \\ \cos\theta/2 \end{pmatrix} \tag{A.34}$$

Therefore,

$$\langle \hat{u}+|\hat{b}-\rangle = -1$$

$$\langle \hat{d}-|\hat{b}+\rangle = \cos\theta/2$$

$$\langle \hat{t}+|\hat{d}+\rangle = 0$$

$$\langle \hat{t}+|\hat{u}-\rangle = \cos\theta/2$$

$$\langle \hat{t}-|\hat{d}+\rangle = -1$$

$$\langle \hat{t}-|\hat{u}-\rangle = -\sin\theta/2. \tag{A.35}$$

Including the common factor

$$\sqrt{2E_u}\sqrt{2E_b}\sqrt{2E_d} = \sqrt{\sqrt{\hat{s}}(\hat{s}-m_t^2)} \tag{A.36}$$

and

$$\sqrt{E_t + |\vec{t}|} = \sqrt{\sqrt{\hat{s}}}$$

$$\sqrt{E_t - |\vec{t}|} = \sqrt{\frac{m_t^2}{\sqrt{\hat{s}}}}$$

we see that

$$\mathcal{M}(+) = 2(\kappa_R{}^{CC})\sqrt{\hat{s}\,(\hat{s}-m_t^2)}\cos^2\theta/2, \tag{A.37}$$

$$\mathcal{M}(-) = 2(1+\kappa_L{}^{CC})\sqrt{\hat{s}(\hat{s}-m_t^2)} - 2(\kappa_R{}^{CC})\sqrt{m_t^2(\hat{s}-m_t^2)}\,\sin\theta/2\cos\theta/2\,.$$
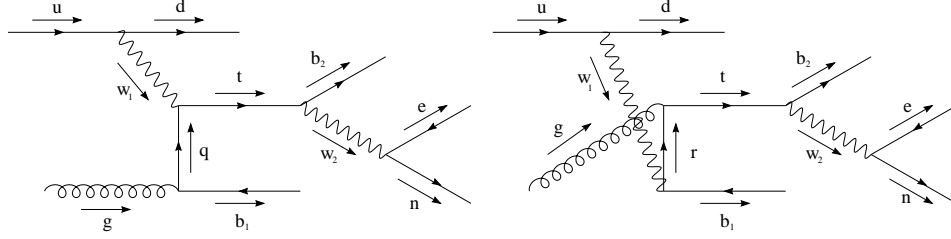
Figure A.2: Diagrams for $u\,g \to d\,t(\to b\,W^+(\to \ell^+\,\nu_\ell))\,\bar{b}$.

Notice in the SM, the top quark is 100% left-hand polarized in the CMS.

Having outlined the general procedure for calculating amplitudes using the helicity amplitude method, we list the matrix elements contributing to single top production and the major background $W b\bar{b}$ in the Standard Model. We include the decay of $t \to bW^+$ and $W^+ \to \ell^+\nu_\ell$ in the final form.

A.3 Helicity Amplitudes for $u\,g \to d\,t(\to b\,W^+(\to \ell^+\,\nu_\ell))\,\bar{b}$

In this and the following sections, we give the diagrams for the process listed, indicating the momentum flow and particle momentum labels: w's are for W^+ bosons, b's for b or $\bar{b}$ quarks, e for e^+, n for ν_e and u, d, t and g are for u, d, t quarks and gluon, respectively.

In Figure A.2, we show the diagrams for $u\,g \to d\,t(\to b\,W^+(\to \ell^+\,\nu_\ell))\,\bar{b}$. $\mathcal{M}_i(h_g, \lambda_{b_1})$ will represent the ith diagram ($i = 1, 2$ from left to right in Figure A.2) where h_g represents the two transverse gluon polarizations and λ_{b_1} represents the two helicity states of $\bar{b}$. The matrix element in the helicity amplitude formalism for this process is

$$\mathcal{M}_1(h_g, \mp) = 4\langle \hat{b}_2 -|\,\hat{n}\,+\rangle\langle \hat{e}\,+|\,\slashed{t}_-\,|\,\hat{d}\,+\rangle \times$$

$$\frac{\pm\sqrt{E_{b_1}\mp|\vec{b_1}\,|}\,\langle \hat{u}\,+|\,\slashed{d}_-\,\slashed{\epsilon}(h_g)_+\,|\,\hat{b_1}\,\pm\rangle \mp m_b\sqrt{E_{b_1}\pm|\vec{b_1}\,|}\,\langle \hat{u}\,+|\,\slashed{\epsilon}(h_g)_-\,|\,\hat{b_1}\,\pm\rangle}{(q^2 - m_b^2)}$$

$$\mathcal{M}_2(h_g, \mp) = \pm 4\sqrt{E_{b_1}\mp|\vec{b_1}\,|}\,\langle \hat{b}_2 -|\,\hat{n}\,+\rangle\langle \hat{u}\,+|\,\hat{b_1}\,\pm\rangle \times$$

$$\frac{\langle \hat{e}\,+|\,\slashed{t}_-\,\slashed{\epsilon}(h_g)_+\,\slashed{t}_-\,|\,\hat{d}\,+\rangle + m_t^2\langle \hat{e}\,+|\,\slashed{\epsilon}(h_g)_-\,|\,\hat{d}\,+\rangle}{(r^2 - m_t^2)} \tag{A.38}$$

where we have indicated the four different helicity states involved in this process. We keep the mass of the $\bar{b}$ parton to avoid the case where the b propagator goes on shell.
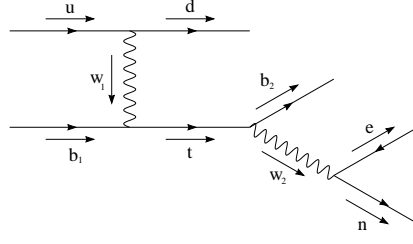
Figure A.3:   Diagram for $u\,b \to d\,t(\to b\,W^+(\to \ell^+\,\nu_\ell))$.

For simplicity we have omitted a common factor of

$$
g_S^2 \left(\frac{g_W}{\sqrt{2}}\right)^4 \frac{\sqrt{(2E_u)(2E_d)(2E_{b_2})(2E_e)(2E_n)}}{(t^2 - m_t^2)(w_1^2 - M_W^2)(w_2^2 - M_W^2)}
\tag{A.39}
$$

and color matrices.[4] We note that the polarization vectors for spin-1 gauge bosons may be expressed in terms of spin-$\frac{1}{2}$ bras and kets. We define

$$
|+\rangle = \begin{pmatrix} 1 \\ 0 \end{pmatrix} \quad |-\rangle = \begin{pmatrix} 0 \\ 1 \end{pmatrix},
\tag{A.40}
$$

then for the transverse polarizations

$$
\begin{aligned}
\not{\epsilon}_\pm^{(R)} &= \mp\sqrt{2}|\,\hat{g}+\rangle\langle\,\hat{g}-| \\
\not{\epsilon}_\pm^{(L)} &= \pm\sqrt{2}|\,\hat{g}-\rangle\langle\,\hat{g}+|
\end{aligned}
\tag{A.41}
$$

and for massive spin-1 gauge bosons

$$
\begin{aligned}
\not{\epsilon}_+^{(0)} &= \left(\frac{|\vec{g}|}{m} - \frac{E}{m}\right)(|+\rangle\langle+| + |-\rangle\langle-|) + 2\frac{E}{m}|\,\hat{g}+\rangle\langle\,\hat{g}+| \\
\not{\epsilon}_-^{(0)} &= \left(\frac{|\vec{g}|}{m} - \frac{E}{m}\right)(|+\rangle\langle+| + |-\rangle\langle-|) + 2\frac{E}{m}|\,\hat{g}-\rangle\langle\,\hat{g}-|.
\end{aligned}
\tag{A.42}
$$

A.4 Helicity Amplitudes for $u\,b \to d\,t(\to b\,W^+(\to \ell^+\,\nu_\ell))$

In Figure A.3, we show the diagram for $u\,b \to d\,t(\to b\,W^+(\to \ell^+\,\nu_\ell))$. The matrix element in the helicity amplitude formalism for this process is

$$
\mathcal{M} = 4\langle\,\hat{u}+|\,\hat{b}_1-\rangle\langle\,\hat{e}+|\,\not{\epsilon}_-\,|\,\hat{d}+\rangle\langle\,\hat{b}_2-|\,\hat{n}+\rangle
\tag{A.43}
$$

---

[4] The color factor for the amplitude squared is $3 \times 4 \times 1/3 \times 1/8$ for this process.
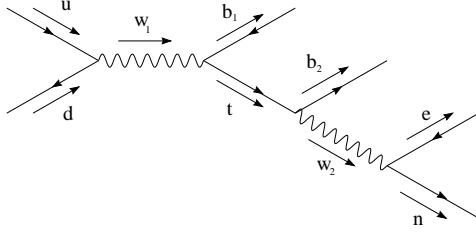
Figure A.4:   Diagram for $u\,\bar{d} \to \bar{b}\,t(\to b\,W^+(\to \ell^+\,\nu_\ell))$.

where we ignore the b parton mass. We have omitted a common factor of

$$\left(\frac{g_W}{\sqrt{2}}\right)^4 \frac{\sqrt{(2E_u)(2E_d)(2E_{b_1})(2E_{b_2})(2E_e)(2E_n)}}{(t^2 - m_t^2)(w_1^2 - M_W^2)(w_2^2 - M_W^2)} \tag{A.44}$$

and color matrices.[5]

A.5   Helicity Amplitudes for $u\,\bar{d} \to W^* \to \bar{b}\,t(\to b\,W^+(\to \ell^+\,\nu_\ell))$

In Figure A.4, we show the diagram for $u\,\bar{d} \to W^* \to \bar{b}\,t(\to b\,W^+(\to \ell^+\,\nu_\ell))$. Aside from a possible phase, the matrix element in the helicity amplitude formalism for this process (W^* production) is identical to that of Figure A.3. This is because one process is the cross diagram of the other and therefore only the momentum assignments are different. For clarity, it is

$$\mathcal{M} = 4\langle\,\hat{u}+|\,\hat{b}_1\,-\rangle\langle\,\hat{e}+|\,\not{t}_-\,|\,\hat{d}\,+\rangle\langle\,\hat{b}_2\,-|\,\hat{n}\,+\rangle. \tag{A.45}$$

Again we ignore the b parton mass and omit the common factor of

$$\left(\frac{g_W}{\sqrt{2}}\right)^4 \frac{\sqrt{(2E_u)(2E_d)(2E_{b_1})(2E_{b_2})(2E_e)(2E_n)}}{(t^2 - m_t^2)(w_1^2 - M_W^2)(w_2^2 - M_W^2)} \tag{A.46}$$

and color matrices.[6]

A.6   Helicity Amplitudes for $u\,\bar{d} \to \bar{b}\,b\,W^+(\to \ell^+\,\nu_\ell)$

In Figure A.5 we show the diagrams for $u\,\bar{d} \to \bar{b}\,b\,W^+(\to \ell^+\,\nu_\ell)$, the major $W + 2$ jets background to W–gluon fusion including b-tagging. The matrix element in the

---

[5] The color factor for the amplitude squared is $3 \times 3 \times 1/3 \times 1/3$ for this process.

[6] The color factor for the amplitude squared is $3 \times 3 \times 1/3 \times 1/3$ for this process.
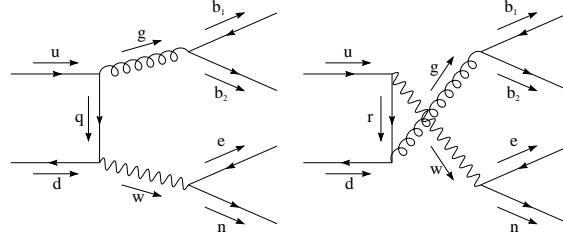
Figure A.5:   Diagrams for $u\,\bar{d} \to \bar{b}\,b\,W^+(\to \ell^+\,\nu_\ell)$.

helicity amplitude formalism is

$$
\mathcal{M}(+,-) = 4\langle\,\hat{d}-|\,\hat{n}+\rangle\langle\,\hat{b}_1+|\,\hat{u}-\rangle\langle\,\hat{e}+|\,\not{q}_-\,|\,\hat{b}_2+\rangle/q^2
$$
$$
+\,4\langle\,\hat{d}-|\,\hat{b}_2+\rangle\langle\,\hat{e}+|\,\hat{u}-\rangle\langle\,\hat{b}_1+|\,\not{r}_-\,|\,\hat{n}+\rangle/r^2
$$
$$
\mathcal{M}(-,+) = 4\langle\,\hat{d}-|\,\hat{n}+\rangle\langle\,\hat{b}_2+|\,\hat{u}-\rangle\langle\,\hat{e}+|\,\not{q}_-\,|\,\hat{b}_1+\rangle/q^2
$$
$$
+\,4\langle\,\hat{d}-|\,\hat{b}_1+\rangle\langle\,\hat{e}+|\,\hat{u}-\rangle\langle\,\hat{b}_2+|\,\not{r}_-\,|\,\hat{n}+\rangle/r^2 \tag{A.47}
$$

where we have indicated the helicity states of $\bar{b}$ and b as $\mathcal{M}(\lambda_{b_1}, \lambda_{b_2})$. We have once again left out the factor of

$$
g_S^2\left(\frac{g_W}{\sqrt{2}}\right)^2 \frac{\sqrt{(2E_u)(2E_d)(2E_{b_1})(2E_{b_2})(2E_e)(2E_n)}}{(g^2)(w^2 - M_W^2)} \tag{A.48}
$$

and color matrices. [7]

---

[7] The color factor for the amplitude squared is $2 \times 1/3 \times 1/3$ for this process.

Appendix B

Event Rate of the $(2 \to 3)$ Process $ug \to dt\bar{b}$

Monte Carlo integration is an indispensable tool in phenomenology. However, when performing a calculation one often encounters singularities which make it impossible to obtain meaningful results from a Monte Carlo program. In the case of delta functions one is forced to integrate by hand. Other singularities may occur when propagators go on mass–shell. These types of divergences may be regularized by applying suitable cuts on the external particles in the process. However, when one is interested in obtaining a total rate, part of the calculation must be performed by hand if there is any singularity present.

To obtain the total rate for the $(2 \to 3)$ process $ug \to dt\bar{b}$ via Monte Carlo integration, the idea is to integrate out the $W^+g \to tb$ sub-cross section in Figure (B.1) by hand. The alternative is to use Monte Carlo for the full 3-body phase space, but the singularity due to the small mass of the b quark in the right diagram would require too much computer time even for the powerful technique applied in VEGAS, a fortran code for calculating multiple dimensional integrations [64]. An added benefit of performing the sub-cross section integration in the way shown in this appendix is an understanding of the validity of the effective–W approximation[33].
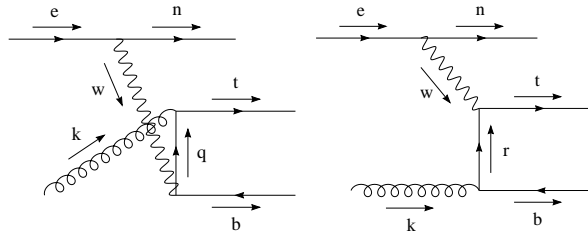
Figure B.1: Diagrams for $u\,g \to d\,t\,\bar{b}$.

The differential cross section for this process is

$$\sigma = \frac{1}{2s}\int \frac{d^3n}{(2\pi)^3(2E_n)}\sigma_{sub} \tag{B.1}$$

where

$$\sigma_{sub} \equiv \int \frac{d^3t}{(2\pi)^3(2E_t)} \frac{d^3b}{(2\pi)^3(2E_b)} \overline{|\mathcal{M}|^2} (2\pi)^4\delta^4(e+k-n-t-b). \tag{B.2}$$

Since σ_{sub} is a Lorentz invariant, we choose to evaluate it and the matrix element in the $t\bar{b}$ center of mass (CMS) frame. We express the 4-vector components of t, b, e, n and k explicitly as

$$
\begin{aligned}
t &= (E_t, p\sin\theta\cos\phi, p\sin\theta\sin\phi, p\cos\theta)\\
b &= (E_b, -p\sin\theta\cos\phi, -p\sin\theta\sin\phi, -p\cos\theta)\\
e &= E_e(1, \sin\theta_e, 0, \cos\theta_e)\\
n &= E_n(1, \sin\theta_n, 0, \cos\theta_n)\\
k &= E_k(1, 0, 0, 1).
\end{aligned} \tag{B.3}
$$

In the $t\bar{b}$ rest frame $\hat{s} \equiv (t+b)^2$, so

$$E_t = \frac{\hat{s} + m_t^2 - m_b^2}{2\sqrt{\hat{s}}}$$

$$E_b = \frac{\hat{s} - m_t^2 + m_b^2}{2\sqrt{\hat{s}}}$$

$$p = \frac{1}{2\sqrt{\hat{s}}}\sqrt{[\hat{s} - (m_t+m_b)^2][\hat{s} - (m_t-m_b)^2]}. \tag{B.4}$$

It is easy to see in the $t\bar{b}$ CMS, that $\vec{e}, \vec{k}, \vec{n}$ all lie in the same plane. Momentum conservation $(e+k=n+t+b)$ and $\vec{t}+\vec{b}=\vec{0}$ imply $\vec{e}+\vec{k}=\vec{n}$. It only takes two vectors to describe a plane and any vector which is a linear combination of those two vectors lies in that plane. Therefore, we choose the vectors $\vec{e}, \vec{k}, \vec{n}$ to define the x–z plane with the momentum of the gluon ($\vec{k}$) along the z–axis.

For a 3-body final state, there are only 5 ($= 3\times3-4$) independent variables. (The minus 4 is for energy-momentum conservation.) We shall choose the 5 independent variables to be $\theta, \phi, E_n, \theta_n$ and ϕ_n where ϕ_n can be trivially integrated as $\int d\phi_n = 2\pi$. This is a consequence of the arbitrariness of the choice of scattering planes. Hence, we should be able to express all vectors in terms of the 4 variables θ, ϕ, E_n and θ_n.

What we have done so far is express all 4-vectors in the $t\bar{b}$ CMS. It is now a fairly

trivial exersize to evaluate σ_{sub}.[1] We found

$$\sigma_{sub} = \frac{1}{4(2\pi)^2} \frac{p}{\sqrt{\hat{s}}} \int d\cos\theta \, d\phi \, \overline{|\mathcal{M}|^2}. \tag{B.5}$$

Having done so, we now have a Lorentz invariant expression for

$$\sigma_{sub} = \sigma_{sub}(\hat{s}, E_n, \theta_n).$$

To compare our result with the effective–W approximation, we express E_n and θ_n in terms of ek CMS quantities with the aid of some projection operators defined below.

To extract out the information of e, k and n in the $t\bar{b}$ CMS frame we use the fact that $\vec{e} + \vec{k} - \vec{n} = 0$ and $(e + k - n)^2 = \hat{s}$. We then define the projection operators $\mathbf{P}_E$ and $\mathbf{P}_\parallel$ as follows:

$$\mathbf{P}_E V \equiv \frac{(e + k - n) \cdot V}{\sqrt{\hat{s}}} \tag{B.6}$$

$$\mathbf{P}_\parallel V \equiv \frac{-k \cdot V + E_k E_V}{E_k} \tag{B.7}$$

where $V = e, n$ or k. $\mathbf{P}_E$ and $\mathbf{P}_\parallel$ project out the energy of V and component of V parallel to k (i.e., the z–axis) respectively. We express the 4-vector components of e, n and k explicitly as

$$k = \frac{\sqrt{s}}{2}(1, 0, 0, 1)$$

$$e = \frac{\sqrt{s}}{2}(1, 0, 0, -1)$$

$$n = E'_n(1, -\sin\theta'_n, 0, -\cos\theta'_n) \tag{B.8}$$

where $s = (e + k)^2$. From now on we will distinguish ek CMS components from $t\bar{b}$ CMS components by a prime. We assume

$$E'_n = E'_e(1 - x) = \frac{\sqrt{s}}{2}(1 - x)$$

and use the following results

$$\hat{s} = (e + k - n)^2 = xs$$

$$W^2 \equiv (e - n)^2 = -\frac{s}{2}(1 - x)(1 - \cos\theta'_n). \tag{B.9}$$

---

[1] This integration is done analytically to avoid bad convergence in the numerical integration method. All the singular terms are of the nature of $\ln(m_b^2)$. Because the analytic form for this result is long, it will not be explicitly given here.

Using the projection operators it is easy to show

$$E_k = \frac{1}{2\sqrt{xs}}(xs - W^2)$$

$$E_e = \frac{1}{2\sqrt{xs}}(s + W^2)$$

$$E_n = \frac{1}{2\sqrt{xs}}s(1 - x)$$

$$k_\| = E_k$$

$$e_\| \equiv E_e\cos\theta_e = \frac{-1}{2E_k}(W^2 + s(1 - x)) + E_n$$

$$n_\| \equiv E_n\cos\theta_n = \frac{-s}{2E_k} + E_e \tag{B.10}$$

and therefore

$$\sigma_{sub} = \sigma_{sub}(s, x, W^2).$$

Also, the Lorentz invariant phase space integral in terms of ek CMS components becomes

$$\int \frac{d^3n'}{(2\pi)^3(2E'_n)} = \frac{1}{(4\pi)^2}\int_0^1 dx \int_{-s(1-x)}^0 dW^2. \tag{B.11}$$

Finally, the following cross section

$$\sigma = \frac{1}{2s(4\pi)^2}\int_0^1 dx \int_{-s(1-x)}^0 dW^2\sigma_{sub}(s, x, W^2) \tag{B.12}$$

may be folded in with parton distributions and safely evaluated using a Monte Carlo program.

We note that $\sqrt{W^2}$ is the virtuality of the W–boson line emitted from the u–quark line (with momentum e). $(1-x)$ is the fraction of the incoming u–quark energy carried away by the outgoing d–quark line in the ek CMS. If desired, one can approximate the above equation as the result of the effective–W approximation. However, we shall not pursue it further here.

Appendix C

Helicity Amplitudes of $t \to W^+ b$ and $\bar{t} \to W^- \bar{b}$

In Equations (6.1) and (6.2) we have listed the most general form factors for the decay processes $t \to W^+ + b$ and $\bar{t} \to W^- + \bar{b}$. Here we use those equations to calculate the helicity amplitudes for an on–shell W–boson. (We take the limit of $m_b \to 0$ in the following for $m_t \gg m_b$.)

For the decay process $t \to W^+ b$, the top quark is taken to decay in its rest frame where the top quark momentum is $p_t = (m_t, 0, 0, 0)$. Spherical coordinates are used to describe the outgoing particles; θ is taken from the positive Z–axis and ϕ is taken from the positive X–axis in the $X - Y$ plane. The bottom quark and the W–boson are taken on their mass shells with the four–momenta for the bottom quark (p_b) and the W–boson (p_W) taken as

$$
\begin{aligned}
p_b &= (E_b, -E_b \sin\theta \cos\phi, -E_b \sin\theta \sin\phi, -E_b \cos\theta), \\
p_W &= (E_W, E_b \sin\theta \cos\phi, E_b \sin\theta \sin\phi, E_b \cos\theta),
\end{aligned}
\tag{C.1}
$$

where we have neglected the bottom quark mass, and

$$
E_b = \frac{m_t^2 - M_W^2}{2m_t}.
\tag{C.2}
$$

The angles θ and ϕ refer to the direction of the W–boson.

Denote the helicity amplitudes as (h_t, λ_W, h_b) with $\lambda_W = -, +, 0$ being a left-handed, right-handed, and longitudinal W–boson. After suppressing the common factor

$$
\frac{-g}{\sqrt{2}} \sqrt{2 E_b m_t},
\tag{C.3}
$$

there are 8 nonvanishing helicity amplitudes in the rest frame of the top quark for $m_b = 0$:

$$(- \, 0 \, -) \;=\; \left(\frac{m_t}{M_W} f_1^L + f_2^R \right) \sin \frac{\theta}{2},$$

$$(- \, - \, -) \;=\; \sqrt{2} \left(f_1^L + \frac{m_t}{M_W} f_2^R \right) \cos \frac{\theta}{2} e^{i\phi},$$

$$(+ \, 0 \, -) \;=\; \left(\frac{m_t}{M_W} f_1^L + f_2^R \right) \cos \frac{\theta}{2} e^{i\phi},$$

$$(+ \, - \, -) \;=\; -\sqrt{2} \left(f_1^L + \frac{m_t}{M_W} f_2^R \right) \sin \frac{\theta}{2} e^{2i\phi},$$

$$(- \, 0 \, +) \;=\; - \left(\frac{m_t}{M_W} f_1^R + f_2^L \right) \cos \frac{\theta}{2} e^{-i\phi},$$

$$(- \, + \, +) \;=\; -\sqrt{2} \left(f_1^R + \frac{m_t}{M_W} f_2^L \right) \sin \frac{\theta}{2} e^{-2i\phi},$$

$$(+ \, 0 \, +) \;=\; \left(\frac{m_t}{M_W} f_1^R + f_2^L \right) \sin \frac{\theta}{2},$$

$$(+ \, + \, +) \;=\; -\sqrt{2} \left(f_1^R + \frac{m_t}{M_W} f_2^L \right) \cos \frac{\theta}{2} e^{-i\phi}. \tag{C.4}$$

To obtain the averaged amplitude squared, a spin factor $\frac{1}{2}$ should be included. We note that there is no right-handed W–boson produced with a massless left-handed b from a top quark decay. Similarly, from helicity conservation, it is not possible to have a left-handed W–boson produced with a massless right-handed b from t decay.

For an unpolarized top quark decay, after summing over the helicities of the bottom quark, the amplitudes squared for various W polarizations are, apart from a common factor $(g^2 E_b m_t)$,

$$\overline{|M(\lambda_W = -)|^2} \;=\; \left| f_1^L + \frac{m_t}{M_W} f_2^R \right|^2,$$

$$\overline{|M(\lambda_W = +)|^2} \;=\; \left| f_1^R + \frac{m_t}{M_W} f_2^L \right|^2,$$

$$\overline{|M(\lambda_W = 0)|^2} \;=\; \frac{1}{2} \left| \frac{m_t}{M_W} f_1^L + f_2^R \right|^2 + \frac{1}{2} \left| \frac{m_t}{M_W} f_1^R + f_2^L \right|^2. \tag{C.5}$$

The fraction (f_{Long}) of longitudinally polarized W-boson produced in the rest frame of the top quark is defined as the ratio of the number of longitudinally polarized W–bosons produced with respect to the total number of W–bosons produced in top quark decays:

$$f_{\text{Long}} \quad = \quad \frac{\Gamma(\lambda_W = 0)}{\Gamma(\lambda_W = 0) + \Gamma(\lambda_W = -) + \Gamma(\lambda_W = +)}$$

$$= \quad \frac{\overline{|M(\lambda_W = 0)|^2}}{\overline{|M(\lambda_W = 0)|^2} + \overline{|M(\lambda_W = -)|^2} + \overline{|M(\lambda_W = +)|^2}} \, , \qquad \text{(C.6)}$$

where we use $\Gamma(\lambda_W)$ to refer to the decay rate for a top quark to decay into a W–boson with polarization λ_W.

Using a parallel definition for the process $\bar{t} \rightarrow W^- \bar{b}$, we obtain the helicity amplitudes $(h_{\bar{t}}, \lambda_W, h_{\bar{b}})$, similar to the ones listed in Equation (C.4) for the $t \rightarrow W^+ b$ process, provided we replace f_1^L by f_1^{R*}, f_1^R by f_1^{L*}, f_2^L by f_2^{R*}, and f_2^R by f_2^{L*}. (Here the superscript $*$ means complex conjugate.)

The helicity amplitudes of the process $W^+ \rightarrow e^+ \nu_e$ are well known. After suppressing the common factor (gM_W), they are

$$(\lambda_W = -) \quad = \quad -e^{-i\phi_e^*} \left(\frac{1 - \cos\theta_e^*}{2} \right),$$

$$(\lambda_W = 0) \quad = \quad -\frac{\sin\theta_e^*}{\sqrt{2}},$$

$$(\lambda_W = +) \quad = \quad -e^{i\phi_e^*} \left(\frac{1 + \cos\theta_e^*}{2} \right), \qquad \text{(C.7)}$$

where θ_e^* and ϕ_e^* refer to e^+ in the rest frame of W^+.

The helicity amplitudes (λ_W) for the decay process $W^- \rightarrow e^- \bar{\nu}_e$ can be obtained from Equation (C.7) by replacing θ_e^* by $\pi - \theta_e^*$ and ϕ_e^* by $\pi + \phi_e^*$. In this case, θ_e^* and ϕ_e^* refer to e^- in the rest frame of W^-.

Appendix D

The Total Rate for W–gluon Fusion

As discussed in Section 2, the total rate for the W–gluon fusion process is obtained by

$$Total = (2 \rightarrow 2) + (2 \rightarrow 3) - (\text{splitting piece})$$

and the rates of

$$(2 \rightarrow 2) = \int d\xi_1 \, d\xi_2 \, f_{q'/A}(\xi_1, \mu) \, f_{b/B}(\xi_2, \mu) \, \hat{\sigma}(q'b \rightarrow qt)$$

$$+ \int d\xi_1 \, d\xi_2 \, f_{b/A}(\xi_1, \mu) \, f_{q'/B}(\xi_2, \mu) \, \hat{\sigma}(bq' \rightarrow qt) \tag{D.1}$$

$$(2 \rightarrow 3) = \int d\xi_1 \, d\xi_2 \, f_{q'/A}(\xi_1, \mu) \, f_{g/B}(\xi_2, \mu) \, \hat{\sigma}(q'g \rightarrow qt\bar{b})$$

$$+ \int d\xi_1 \, d\xi_2 \, f_{g/A}(\xi_1, \mu) \, f_{q'/B}(\xi_2, \mu) \, \hat{\sigma}(gq' \rightarrow qt\bar{b}) \tag{D.2}$$

$$(\text{splitting piece}) = \int d\xi_1 \, d\xi_2 \, f_{q'/A}(\xi_1, \mu) \, \widetilde{f_{b/B}}(\xi_2, \mu) \, \hat{\sigma}(q'b \rightarrow qt)$$

$$+ \int d\xi_1 \, d\xi_2 \, \widetilde{f_{b/A}}(\xi_1, \mu) \, f_{q'/B}(\xi_2, \mu) \, \hat{\sigma}(bq' \rightarrow qt) \tag{D.3}$$

where, for instance, $f_{b/A}(\xi_1, \mu)$ denotes the parton distribution function (PDF) of the b quark inside hadron A, carrying the fraction ξ_1 of the hadron momentum, and μ is the energy scale at which the PDF is evaluated. The constituent cross section $\hat{\sigma}$ is given by the differential cross section for

$$p_1(m_1) + p_2(m_2) \rightarrow p'_1(m'_1) + p'_2(m'_2) + \cdots + p'_n(m'_n), \tag{D.4}$$

as shown in Figure D.1. The differential cross section is

$$d\hat{\sigma} = \frac{\overline{|\mathcal{M}|^2} \, d\Phi_n(p_1 + p_2; p'_1, \cdots, p'_n)}{4\sqrt{(p_1 \cdot p_2)^2 - m_1^2 m_2^2}} \tag{D.5}$$

with

$$d\Phi_n(p_1 + p_2; p'_1, \cdots, p'_n) = (2\pi)^4 \delta^4(p_1 + p_2 - \sum_{i=1}^{n} p'_i) \prod_{i=1}^{n} \frac{d^3 p'_i}{(2\pi)^3 dE'_i} \qquad (D.6)$$

and $\overline{|\mathcal{M}|^2}$ is the square of the amplitude after summing over the final state polarization and colors and averaging over the initial state polarization and colors. Notice that the differential cross section for $d\hat{\sigma}(bq' \to qt)$ can be obtained from $d\hat{\sigma}(q'b \to qt)$ by interchanging the 4–momenta p_1 and p_2 in the scattering amplitudes. In terms of the polar angle θ^* and azimuthal angle ϕ^* defined in the center-of-mass frame of the partons, this means replace θ^* by $\pi - \theta^*$ and ϕ^* by $\pi + \phi^*$. In Equation (D.3), the effective parton density

$$\widetilde{f_{b/A}}(\xi, \mu) = \frac{\alpha_S(\mu)}{2\pi} \ln\left(\frac{\mu^2}{m_b^2}\right) \int \frac{dz}{z} \left[\frac{z^2 + (1-z)^2}{2}\right] f_{g/A}\left(\frac{\xi}{z}, \mu\right) \qquad (D.7)$$

in the $\overline{\text{MS}}$ scheme. The coupling constant

$$\alpha_S(\mu) = \frac{12\pi}{(33 - 2n_f) \ln(\frac{\mu^2}{\Lambda^2})}. \qquad (D.8)$$

Here, n_f is the number of quarks with mass less than the energy scale μ. The QCD parameter $\Lambda \equiv \Lambda_{\overline{\text{MS}}}^{(n_f)}$ is an experimentally determined parameter. Perturbative QCD is presumed to be applicable for $\mu \gg \Lambda$. For CTEQ2L PDF, $\Lambda_{\overline{\text{MS}}}^{(4)} = 190$ MeV.
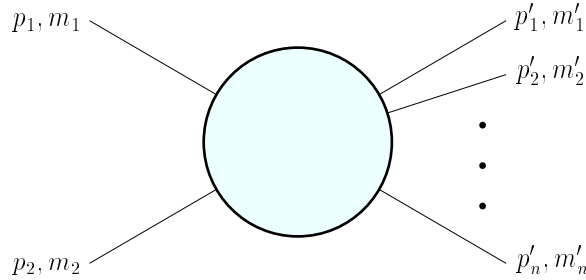

Figure D.1: n–body scattering

Appendix E

The Eikonal Approximation for $\sigma(AB(u\bar{d}) \to \bar{b}bW^+ + jet)$

Applying the Eikonal approximation, we can write the cross section of $\sigma(AB(u\bar{d}) \to \bar{b}bW^+ + jet)$ in terms of the amplitude square of the $u\bar{d} \to \bar{b}bW^+$ process as follows.

$$\sigma(AB(u\bar{d}) \to \bar{b}bW^+ + jet) = \int dQ^2 \int dy \int dq_T^2 \int d\Phi_3 \frac{1}{2S} \left(\frac{\alpha_S(Q)}{2\pi q_T^2} \right) \times$$

$$\left\{ f_{u/A}(x_A, Q) \left[\sum_j P^{(1)}_{\bar{d} \leftarrow j} \circ f_{j/B} + P^{(1)}_{\bar{d} \leftarrow g} \circ f_{g/B} \right] (x_B, Q) + \right. \tag{E.1}$$

$$\left. f_{u/A}(x_A, Q) \, f_{\bar{d}/A}(x_B, Q) \left[C_F \ln \left(\frac{Q^2}{q_T^2} \right) - \frac{3}{2} C_F \right] \right\} \overline{|\mathcal{M}(u\bar{d} \to \bar{b}bW^+)|^2} +$$

$$(A \leftrightarrow B),$$

where $d\Phi_3$ is the usual 3-dimensional phase space volume as defined in Appendix B.

Q, y and q_T are the invariant mass, rapidity and transverse momentum of the $(W + \bar{b} + b)$ system. $\overline{|\mathcal{M}(u\bar{d} \to \bar{b}bW^+)|^2}$ is the amplitude square of $u\bar{d} \to \bar{b}bW^+$ after summing over the spin and color factors in the final state and averaging over the spin and color factors in the initial state. For a given Q, y and q_T

$$x_A = \frac{Q}{\sqrt{S}} e^y, \quad x_B = \frac{Q}{\sqrt{S}} e^{-y}, \tag{E.2}$$

where $\sqrt{S}$ is the center-of-mass energy of the hadrons A and B.

The splitting functions are

$$P^{(1)}_{k \leftarrow j}(z) = C_F \left(\frac{1 + z^2}{1 - z} \right)_+ \delta_{kj}, \tag{E.3}$$

$$P^{(2)}_{k \leftarrow g}(z) = \frac{1}{2}\left(z^2 + (1-z)^2\right)$$

$$\text{(E.4)}$$

and

$$(P^{(1)} \circ f)(x, Q) = \int_x^1 \frac{d\xi}{\xi} P^{(1)}\left(\frac{x}{\xi}\right) f(x, Q),$$

$$\text{(E.5)}$$

$$\text{(E.6)}$$

where the indices j and k denote the flavor of quark or antiquark, δ_{kj} is equal to 1 for $k = j$ and zero otherwise. In QCD, $C_F = \frac{4}{3}$ for three colors. The "+" prescription is defined by

$$\int_x^1 dz \left(\frac{1+z^2}{1-z}\right)_+ f(z) = \int_0^1 dz \frac{(1+z^2)f(z)\theta(z-x) - (1+z^2)f(1)}{1-z},$$

$$\text{(E.7)}$$

where

$$\theta(z-x) = \begin{cases} 1 & \text{for } z > x \\ 0 & \text{otherwise} \end{cases}.$$

$$\text{(E.8)}$$

The above result holds in the soft-gluon approximation. We have also assumed that the initial state QCD radiation dominates the soft-gluon radiation from $u\bar{d} \rightarrow \bar{b}bW^+$. This should be a good approximation because the b quark is massive and is less likely to radiate gluons as compared to the initial state quark or gluon.

Appendix F

The Computer Program ONETOP

Our analysis is based on our Monte Carlo program ONETOP, created by modifying PAPAGENO (version 3.07), written by Ian Hinchliffe. ONETOP contains code for parton level analyses of single top-quark production at hadron colliders as well as the major background. The top quark decays on-shell to bW^+ with branching ratio Br $= 1$. All final state W's decay on-shell to $e\nu$ with branching ratio Br $= \frac{1}{9}$.

In addition, we implemented QCD $t\bar{t}$ production with the top quark decaying on-shell according to the Effective Lagrangian of Equation(6.1), which includes the most general t-b-W couplings.

Only the CTEQ2 leading order parton distribution is implemented[27]. ONETOP accepts matrix elements calculated using the helicity amplitude method described in Appendix A. Squaring of the matrix elements and sums over spin and color are performed numerically. We include a simple histogramming package which allows the plotting of one- and two-dimensional differential cross-sections to aid in analyzing event topologies.

We list below the processes included in ONETOP. The structure of these processes are fully discussed in Section 7.

- $q'b \rightarrow q\, t(\rightarrow bW^+(\rightarrow \ell^+\nu))$,

- $q'g \rightarrow q\, t(\rightarrow bW^+(\rightarrow \ell^+\nu))\,\bar{b}$,

- $q'\bar{q} \rightarrow W^* \rightarrow \bar{b}\, t(\rightarrow bW^+(\rightarrow \ell^+\nu))$,

- $q'\bar{q} \rightarrow \bar{b}bW^+(\rightarrow \ell^+\nu)$,

- $q\bar{q},\, gg \rightarrow t(\rightarrow bW^+(\rightarrow \ell^+\nu))\,\bar{t}(\rightarrow \bar{b}W^-(\rightarrow \ell^-\bar{\nu}))$.

Bibliography

[1] D.J. Griffiths, *Introduction to Elementary Particles*, John Wiley & Sons, Inc., 1987.

[2] F. Halzen and A.D. Martin, *Quarks and Leptons: An Introductory Course in Modern Particle Physics*, John Wiley & Sons, Inc., 1984.

[3] F. Mandl and G. Shaw, *Quantum Field Theory*, John Wiley & Sons, Inc., 1984.

[4] P. Renton, *Electroweak Interactions: An Introduction to the Physics of Quarks and Leptons*, Cambridge University Press, 1990.

[5] Review of Particle Properties, *Phys. Rev.* **D50**, Aug. 1994, pp. 1315-1317.

[6] J.F. Donoghue, E. Golowich and B.R. Holstein, *Dynamics of the Standard Model*, Cambridge University Press, 1992

[7] L. Wolfenstein, *Phys. Rev. Lett.* **51**, 1945 (1983).

[8] G.L. Kane, in *Proceedings of the Workshop on High Energy Phenomenology*, Mexico City, Mexico, July 1–10, 1991.

[9] F. Abe *et al.*, *Phys. Rev. Lett.* **73**, 220 (1994).

[10] M. Veltman, *Acta. Phys. Polon.* **B12**, 437 (1981);
M. Einhorn, D.R.T. Jones, M. Veltman, *Nucl. Phys.* **B191**, 146 (1981).

[11] The LEP Collaborations ALEPH, DELPHI, L3, OPAL and the LEP Electroweak Working Group, CERN/PPE/93–157 (1993);
W. Hollik, in *Proceedings of the XVI International Symposium on Lepton–Photon Interactions*, Cornell University, Ithaca, N.Y., Aug. 10–15, 1993;
M. Swartz, in *Proceedings of the XVI International Symposium on Lepton–Photon Interactions*, Cornell University, Ithaca, N.Y., Aug. 10–15, 1993;
Barbara Mele, in *XIV Encontro Nacional de Fisica de Campos e Particulas*, Caxambu, Brazil, 29 Sept.–3 Oct., 1993;
J. Lefrancois, in *Proceedings of the EPS Conference on Higs Energy Physics*, Marseille, France, 1993.

[12] G. Altarelli, in *Proceedings of International University School of Nuclear and Particle Physics: Substructures of Matter as Revealed with Electroweak Probes*, Schladming, Austria, 24 Feb - 5 Mar 1993.

[13] M. Koratsinos and S. de Jong, in *Proceedings of the Rencontres de la Vallee d'Aoste*, La Thuile, 1994 ;
P. Clarke, P. Siegrist and B. Pietrzyk, in *Proceedings of the Rencontres de Moriond*, Meribel, 1994.

[14] M. Woods, in *Proceedings of the Rencontres de Moriond*, Meribel, 1994.

[15] CDF Collaboration (F. Abe, et al.), FERMILAB-PUB-95-022-E, March 1995.

[16] DØ Collaboration (S. Abachi, et al.), FERMILAB-PUB-95-028-E, March 1995; to appear in *Phys. Rev. Lett.*

[17] R.D. Peccei, S. Peris and X. Zhang, *Nucl. Phys.* **B349**, 305 (1990).

[18] R.S. Chivukula, E. Gates, E.H. Simmons and J. Terning, *Phys. Lett.* **B311**, 157 (1993);
R.S. Chivukula, E.H. Simmons and J. Terning, *Phys. Lett.* **B331**, 383 (1994).

[19] D. Carlson, Ehab Malkawi and C.–P. Yuan, *Phys. Lett.* **B337** (1994) 145;
Ehab Malkawi and C.–P. Yuan. *Phys. Rev.* **D50**, 4462 (1994);
Ehab Malkawi and C.–P. Yuan. MSUHEP-50107, January 1995.

[20] I.I.Y. Bigi, Yu L. Dokshitzer, V.A. Khoze, J.H. Kuhn and P. Zerwas, *Phys. Lett.* **181B** (1986) 157;
L.H. Orr and J.L. Rosner, *Phys. Lett.* **246B** (1990) 221; **248B** (1990) 474(E).

[21] F. Berends et al., in the report of the Top Physics Working Group from the *Proceedings of the Large Hadron Collider Workshop*, 4-9 October 1990, Aachen, ed. G. Jarlskog and D. Rein, CERN publication CERN 90-10, pg. 310, Figure 7/8;
A. Stange and S. Willenbrock, *Phys. Rev.* **D48** (1993) 2054;
C. Kao, G.A. Ladinsky, C.–P. Yuan, MSUHEP-93/04, 1993; MSUHEP-94/04, 1994;
W. Beenakker, *et al.*, *Nucl. Phys.* **B411** (1994) 343;
Chung Kao, FSU-HEP-940508, June 1994.

[22] See, for example,
C.–P. Yuan, *et al.*, *Report of the subgroup on the Top Quark*, in *Proceedings of Workshop on Physics at Current Accelerators and Supercolliders*, eds. by J. Hewett, A. White and D. Zeppenfeld, 1993, pp 495-505; and the references therein.
For NLO analyses, see, for example,
L.H. Orr, T. Stelzer, W.J. Stirling, DTP-94-112, Nov 1994;
S. Frixione, M.L. Mangano, P. Nason, G. Ridolfi, CERN-TH-95-52, March 1995; and the references therein.

[23] S. Dawson, *Nucl. Phys.* **B249**, 42 (1985);
S. Dawson and S. Willenbrock, *Nucl. Phys.* **B284**, 449 (1987);
S. Willenbrock and D.A. Dicus, *Phys. Rev.* **D34**, 155 (1986);
F. Anselmo, B. van Eijk and G. Bordes, *Phys. Rev.* **D45**, 2312 (1992);
T. Moers, R. Priem, D. Rein and H. Reithler, in *Proceedings of Large Hadron Collider Workshop*, preprint CERN 90-10, 1990;
R.K. Ellis and S. Parke, *Phys. Rev.* **D46**, 3785 (1992).

[24] C.–P. Yuan, *Phys. Rev.* **D41**, 42 (1990);
D. Carlson and C.–P. Yuan, *Phys. Lett.* **B306** (1993) 386.

[25] S. Cortese and R. Petronzio, *Phys. Lett.* **B253** (1991) 494.

[26] G.A. Ladinsky and C.–P. Yuan, *Phys. Rev.* **D43**, 789 (1991);

[27] J. Botts, J. Huston, H. Lai, J. Morfin, J. Owens, J. Qiu, W.-K. Tung, H. Weerts, Michigan State University preprint MSUTH-93/17.

[28] P. Nason, S. Dawson and R.K. Ellis, *Nucl. Phys.* **B303**, 607 (1988); **B327**, 49 (1989);
W. Beenakker, H. Kuijf, W.L. van Neerven and J. Smith, *Phys. Rev.* **D40**, 54 (1989);
R. Meng, G.A. Schuler, J. Smith and W.L. van Neerven, *Nucl. Phys.* **B339**, 325 (1990).

[29] E. Laenen, J. Smith and W.L. van Neerven, Nucl. Phys. **B369** (1992) 543

[30] J. C. Collins and Wu-Ki Tung, *Nucl. Phys.* **B278** (1986) 934;
F. Olness and Wu-Ki Tung, *Nucl. Phys.* **B308** (1988) 813;
M. Aivazis, F. Olness and Wu-Ki Tung, *Phys. Rev. Lett.* **65** (1990) 2339; *Phys. Rev.* **D50**, 3085 (1994);
M. Aivazis, J.C. Collins, F. Olness and Wu-Ki Tung, *Phys. Rev.* **D50**, 3102 (1994).

[31] C.T. Hill and S. Parke, *Phys. Rev.* **D49** 4454 (1994);
E. Eichten and K. Lane, *Phys. Lett.* **B327** 129 (1994).

[32] R. N. Cahn and S. Dawson, *Phys. Lett.* **B136**, 196 (1984), *Phys. Lett.* **B138**, 464(E) (1984);
M. S. Chanowitz and M. K. Gaillard, *Phys. Lett.* **B142**, 85 (1984);
G. L. Kane, W. W. Repko and W. R. Rolnick, *Phys. Lett.* **B148**, 367 (1984);
S. Dawson, *Nucl. Phys.* **B249**, 42 (1985); *Phys. Lett.* **B217**, 347 (1989);
J. Lindfors, *Z. Phys.* **C28**, 427 (1985);
W. B. Rolnick, *Nucl. Phys.* **B274**, 171 (1986);
P. W. Johnson, F. I. Olness and Wu–Ki Tung, *Phys. Rev.* **D36**, 291 (1987);
Z. Kunszt and D. E. Soper, *Nucl. Phys.* **B296**, 253 (1988);
A. Abbasabadi, W. W. Repko, D. A. Dicus and R. Vega, *Phys. Rev.* **D38**, 2770 (1988).

[33] J. M. Cornwall, D. N. Levin, and G. Tiktopoulos, *Phys. Rev.* **D10**, 1145 (1974);
C. Vayonakis, Lett. Nuovo Cimento **17**, 383 (1976);
B. W. Lee, C. Quigg, and H. Thacker, *Phys. Rev.* **D16**, 1519 (1977);
M. S. Chanowitz and M. K. Gaillard, *Nucl. Phys.* **B261**, 379 (1985);
G. J. Gounaris, R. Kogerler, and H. Neufeld, *Phys. Rev.* **D34**, 3257 (1986);

[34] Y.–P. Yao and C.–P. Yuan, *Phys. Rev.* **D38**, 2237 (1988);
J. Bagger and C. R. Schmidt, *Phys. Rev.* **D41**, 264 (1990);
H. Veltman, *Phys. Rev.* **D41**, 2294 (1990);
H.-J. He, Y.-P. Kuang, and X. Li, *Phys. Rev. Lett.* **69** (1992) 2619; *Phys. Rev.*

D49 (1994) 4842; *Phys. Lett.* **B329** (1994) 278;
A. Dobado and J.R. Pelaez, *Phys. Lett.* **B329** (1994) 469 (Addendum, *ibid*, **B335** (1994) 554); *Nucl. Phys.* **B425** (1994) 110;
H.-J. He, Y.-P. Kuang, and C.–P. Yuan, VPI-IHEP-94-04, MSUHEP-40909, 1994.

[35] See, for example,
C.–P. Yuan, in *Perspectives on Higgs Physics*, edited by G. Kane (World Scientific, 1992), pp 415–428.

[36] M. Veltman, *Acta. Phys. Pol.* **B8** (1977) 475;
M. Einhorn, J. Wudka, *Phys. Rev.* **D39** (1989) 2758;
M. Veltman, UM-TH-94-28, June 1994, Lectures given at *34th Cracow School of Theoretical Physics*, Zakopane, Poland, 31 May - 10 June 1994.

[37] The specific methods used by the CDF and the DØ groups can be found in Refs. [15] and [16], respectively.

[38] ATLAS Letter of Intent, CERN/LHCC/92-4, October 1992. ATLAS Internal Note, A.Mekki and L.Fayard, PHYS-NO-028, 1993. ATLAS Internal Note, Nicholas Andell, PHYS-NO-037, 1994.

[39] CMS Letter of Intent, CERN/LHCC/92-3, October 1992.

[40] Raymond Brock; private communication.

[41] S. Mrenna and C.–P. Yuan, *Phys. Rev.* **D46** (1992) 1007.

[42] SDC technical Design Report, preprint SDC-92-201, 1992.

[43] For a review, see,
S. Cortese and R. Petronzio, *Phys. Lett.* **B276** (1992) 203.

[44] G. L. Kane, G. A. Ladinsky and C.–P. Yuan, *Phys. Rev.* **D45** (1992) 124.

[45] R.D. Peccei and X. Zhang, *Nucl. Phys.* **B337**, 269 (1990).

[46] J. Liu and Y.–P. Yao, University of Michigan preprint UM-TH-90-09;
C.S. Li, R.J. Oakes and T.C. Yuan, *Phys. Rev.* **D43** (1991) 3759;
M. Jezabek and J.H. Kuhn, *Nucl. Phys.* **B314** (1989) 1; *ibid* **B320** (1989) 20.

[47] A. Denner and T. Sack, *Nucl. Phys.* **B358** 46 (1991); *Z. Phys.* **C46**, 653 (1990);
G. Eilam, R. R. Mendel, R. Migneron, and A. Soni, *Phys. Rev. Lett.* **66** (1991) 3105;
B. A. Irwin, B. Margolis, and H. D. Trottier, *Phys. Lett.* **B256**, 533 (1991);
J. Liu and Y.–P. Yao, *Int.J.Mod.Phys.* **A6** (1991) 4925;
T.C. Yuan and C.–P. Yuan, *Phys. Rev.* **D44** (1991) 3603.

[48] F. Abe *et al.*, *Phys. Rev.* **D50**, 2966 (1994).

[49] H. Georgi, *Weak Interactions and Modern Particle Theory* (The Benjamin/Cummings Publishing Company, 1984).

[50] A. Manohar and H. Georgi, *Nucl. Phys.* **B234** (1984) 189.

[51] A similar analysis was also performed by D. Amidei and D. Winn; private communication.

[52] This is the kind of analysis that has currently been performed at LEP for separating a quark jet from a gluon jet.

[53] K. Fujikawa and A. Yamada, *Phys. Rev.* **D49**, 5890 (1994).

[54] D. Chang, W.-Y. Keung, I. Phillips, *Nucl. Phys.* **B408** (1993) 286.

[55] J. M. Soares and L. Wolfenstein, *Phys. Rev.* **D46** (1992) 256.

[56] C.–P. Yuan, preprint MSUHEP-41009, November 1994.

[57] B. Grzadkowski and J.F. Gunion, *Phys. Lett.* **B287** (1992) 237.

[58] R. Kauffman, *Phys. Rev.* **D41** (1990) 3343.

[59] B. Grzadkowski and W.-Y. Keung, *Phys. Lett.* **B319** (1993) 526;
M. Nowakowski and A. Pilaftsis, *Mod. Phys. Lett.* **A4** (1989) 821; *Z. Phys.* **C42** (1989) 449;
A. Pilaftsis, *Z. Phys.* **C47** (1990) 95;
M. Nowakowski and A. Pilaftsis, *Mod. Phys. Lett.* **A6** (1991) 1933; *Phys. Lett.* **B245** (1990) 185.

[60] G. Sterman, *Quantum Field Theory* (Cambridge University Press, 1993).

[61] H. Baer, F.E. Paige, S.D. Protopopescu, X. Tata, FSU-HEP-930329, April 1993.

[62] T. Sjostrand, CERN-TH-7112-93, Feb. 1994.

[63] G. Marchesini, B.R. Webber, G. Abbiendi, I.G. Knowles, M.H. Seymour, L. Stanco, *Comput. Phys. Commun.* **67** (1992) 465.

[64] G.P. Lepage, *J. Comput. Phys.* **27** (1978) 192; CLNS-80/447, Mar 1980.